

Aus der Klinik und Poliklinik für Neurochirurgie  
Klinik der Ludwig-Maximilians-Universität München

Direktor: Prof. Dr. med. Jörg-Christian Tonn

**“Lineage-tracing reveals the genesis of pericytes  
from Nestin expressing cells during glioma angiogenesis”**

Dissertation

zum Erwerb des Doktorgrades der Medizin  
an der Medizinischen Fakultät der  
Ludwig-Maximilians-Universität zu München

vorgelegt von  
Katharina Eisenhut  
aus Heidelberg

2021

Mit Genehmigung der Medizinischen Fakultät  
der Universität München

Berichterstatter:	Prof. Dr. rer. nat. Rainer Glaß
Mitberichterstatter:	Prof. Dr. Simone Kreth PD Dr. Louisa von Baumgarten
Mitbetreuung durch den promovierten Mitarbeiter:	Dr. sc. nat. Roland Kälin
Dekan:	Prof. Dr. med. dent. Reinhard Hickel
Tag der mündlichen Prüfung:	25.03.2021

## Table of contents

I.	List of figures.....	4
II.	List of tables.....	5
III.	List of abbreviations .....	6
1.	Introduction.....	8
1.1	Gliomas.....	8
1.1.1	Glioblastoma multiforme .....	9
1.1.1.1	Clinical presentation and diagnosis .....	10
1.1.1.2	Therapy and prognosis .....	11
1.1.2	Tumor proliferation.....	13
1.1.3	Tumor angiogenesis and Apelin/APJ signaling.....	13
1.1.4	Anti-angiogenic therapies .....	15
1.2	Pericytes.....	16
1.2.1	Definition and characteristics .....	16
1.2.2	Functions.....	17
1.2.3	Markers .....	19
1.2.4	Subtypes.....	20
1.2.5	Ontogeny.....	21
1.2.6	Pericytes in gliomas .....	22
1.2.7	Anti-angiogenic therapies targeting pericytes .....	23
2.	Objectives .....	25
3.	Materials and methods .....	26
3.1	Materials .....	26
3.1.1	Lab devices .....	26
3.1.2	Lab consumables.....	26
3.1.3	Reagents and chemicals .....	27
3.1.4	Cell lines .....	28
3.1.5	Antibodies and streptavidin-conjugated flourophores .....	28
3.1.6	Staining kits .....	31
3.1.7	Computer Software .....	31
3.2	Methods.....	32

3.2.1	Animal model: NesCreER <sup>T2</sup> x Ai9tdTomato.....	32
3.2.2	Treatment protocol.....	33
3.2.2.1	Tumor inoculation.....	34
3.2.2.2	Tamoxifen treatment.....	35
3.2.2.3	CldU/IdU treatment .....	35
3.2.3	Perfusion and tissue preparation .....	35
3.2.4	HE staining.....	36
3.2.5	Immunohistochemistry .....	37
3.2.5.1	Without biotinylated Streptavidin conjugation.....	37
3.2.5.2	With biotinylated Streptavidin conjugation (LSAB method).....	38
3.2.5.3	Mouse-on-mouse kit .....	39
3.2.5.4	CldU/IdU staining.....	39
3.2.5.5	Single-chain fragment variables .....	40
3.2.6	Microscopy .....	41
3.2.6.1	Light microscopy .....	41
3.2.6.2	Fluorescence microscopy.....	41
3.2.6.3	Confocal microscopy .....	41
3.2.7	3D reconstruction.....	42
3.2.8	Evaluation criteria.....	43
3.2.9	CldU/IdU labeling indices .....	44
3.2.10	Statistical analysis.....	44
4.	Results.....	45
4.1	Delineation of the cells of the pericyte-lineage .....	45
4.2	Proliferative expansion of the cells of the pericyte-lineage.....	47
4.2.1	CldU/IdU labeling.....	47
4.2.2	CldU/IdU labeling of endothelial cells and microglia/macrophages.....	48
4.2.3	CldU/IdU labeling of the cells of the pericyte-lineage .....	51
4.3	Characterization of the cells of the pericyte-lineage.....	55
4.3.1	Perivascular location.....	55
4.3.2	Pericyte marker constellation.....	58
4.3.3	Lack of Iba1 expression .....	64
4.3.4	Pericyte subtypes .....	65
4.3.5	Apelin/APJ expression.....	66

5.	Discussion.....	70
5.1	The pericyte-lineage.....	70
5.2	The pericyte-lineage in glioma angiogenesis.....	73
5.3	Cells of the pericyte-lineage as future therapeutic targets? .....	76
6.	Summary.....	78
7.	Zusammenfassung.....	79
8.	References.....	80
9.	Eidesstattliche Versicherung.....	90
10.	Acknowledgements.....	91
11.	Curriculum vitae .....	92
12.	Publication .....	93

## I. List of figures

- Fig. 1 Simplified algorithm of the 2016 WHO classification of diffuse gliomas
- Fig. 2 Axial MRI scans with contrast of a typical GBM case
- Fig. 3 Pericytes as components of the BBB
- Fig. 4 Embryonal ontogeny of vascular mural cells
- Fig. 5 Common model of the ontogeny of tumor-associated pericytes
- Fig. 6 The NesCreER<sup>T2</sup> x Ai9tdTomato mouse model
- Fig. 7 Treatment protocol
- Fig. 8 Schematic illustration of the confocal crosshair mode
- Fig. 9 RFP positive cells in the NesCreER<sup>T2</sup> x Ai9tdTomato mouse model
- Fig. 10 Morphological development of RFP positive cells
- Fig. 11 General CldU/IdU labeling
- Fig. 12 CldU/IdU-labeled cell populations
- Fig. 13 CldU/IdU labeling of RFP positive cells
- Fig. 14 CldU/IdU labeling of perivascular RFP positive cells
- Fig. 15 3D reconstructions of RFP- and IB4-co-stained brain sections
- Fig. 16 3D reconstructions of RFP- and vWF-co-stained brain sections
- Fig. 17 Desmin labeling of RFP positive cells
- Fig. 18 PDGFR $\beta$  labeling of RFP positive cells
- Fig. 19 NG2 labeling of RFP positive cells
- Fig. 20 Pericyte marker co-labeling of perivascular RFP positive cells
- Fig. 21 RFP positive cells do not co-label with Iba1
- Fig. 22 RFP positive cells do not develop into different pericyte subtypes
- Fig. 23 Apelin labeling of RFP positive cells
- Fig. 24 APJ labeling of RFP positive cells
- Fig. 25 The ontogeny of tumor-associated pericytes from Nestin expressing cells

## **II. List of tables**

Tab. 1 Overview of established pericyte markers

Tab. 2 Lab devices

Tab. 3 Lab consumables

Tab. 4 Reagents and chemicals

Tab. 5 Cell lines

Tab. 6 Primary antibodies

Tab. 7 Secondary antibodies

Tab. 8 Streptavidin-conjugated fluorophores

Tab. 9 Staining kits

Tab. 10 Computer software

Tab. 11 CldU/IdU labeling indices

### III. List of abbreviations

5-ALA	5-aminolevulinic acid
APJ	Apelin receptor
ApIn	Apelin
BBB	Blood brain barrier
BM	Basal membrane
bp	Base pair
BrdU	5-Bromodeoxyuridine
cf.	Compare
CldU	5-Chloro-2'-deoxyuridine
CT	Computer tomography
d	Day
DAB	3,3'-Diaminobenzidine
DAPI	4, 6-diamidino-2-phenylindole
DMEM	Dulbecco's Modified Eagle's Medium
DPO	Days post-operative
EDTA	Ethylenediaminetetraacetic acid
EdU	5-Ethynyl-2'-deoxyuridine
EM	Electron microscopy
Fig.	Figure
FLAIR	Fluid-attenuated inversion recovery
GBM	Glioblastoma multiforme
HE	Hematoxylin-Eosin
i.a.	Among others (inter alia)
IB4	Isolectin B4
IDH-1/-2	Isocitrate-dehydrogenase-1/-2
IdU	5-Iodo-2'-deoxyuridine
IgG	Immunoglobulin G
ITGAM	Integrin alpha M
LSAB	Labeled streptavidin biotin
MGMT	O <sup>6</sup> -methylguanine DNA methyltransferase
MMP	Matrix metalloproteinases
MOM	Mouse-on-mouse kit
MRI	Magnetic resonance imaging

MSC	Mesenchymal stem cell
NG2	Neuron-gial 2
NOS	Not otherwise specified
NVU	Neurovascular unit
PBS	Phosphate buffered saline
PBST	Phosphate buffered saline with Tween-20
PDGFR $\beta$	Platelet-derived growth factor receptor $\beta$
PDGF $\beta$	Platelet-derived growth factor $\beta$
PET	Positron-emission tomography
PFA	Paraformaldehyde
RFP	Red fluorescent protein
ScFv	Single-chain fragment variables
SMC	Smooth muscle cell
Tab.	Table
TAM	Tamoxifen
TERT	Telomerase reverse transcriptase
TMZ	Temozolomide
VEGF	Vascular endothelial growth factor
VEGFR	Vascular endothelial growth factor receptor
V <sub>H</sub>	Heavy chain
V <sub>L</sub>	Light chain
vWF	Von Willebrand factor
WHO	World Health Organization
$\alpha$ SMA	$\alpha$ smooth muscle actin

## 1. Introduction

### 1.1 Gliomas

Gliomas are primary tumors of the central nervous system (CNS) [1, 2]. They develop due to malignant transformation of the cells of the brain and spinal cord. Based on their degree of malignancy, as determined by their histological features (i.a. mitoses, nuclear atypia, microvascular proliferation, necrosis), cellular ontogeny (e.g. astrocytomas deriving from astrocytes, oligodendrogliomas deriving from oligodendrocytes etc.) and genetic alterations (amongst others, Isocitrate Dehydrogenase (IDH) mutation status, cf. Fig. 1), they are commonly graded on a World Health Organization (WHO) derived scale of I-IV [3, 4].

Gliomas are primarily of a neuroepithelial provenance [5], representing 31% of all tumors and 70% of malignant tumors in the CNS [6]. They originate from so-called glial cells of the CNS, which decidedly not only support circumjacent neurons but also display various specific functions. While WHO grade I gliomas are generally benign, circumscribed, associated with a high median survival and effective curative approaches, grade II-IV gliomas are malignant and increasingly invasive, the higher the WHO grade. Therapeutic options are, hence, limited leading to high recurrence and poor survival rates. Also, they are likely to progress to higher grade gliomas, resulting in a rapid clinical deterioration [4].

The WHO classification of CNS tumors has been substantially revised in 2016 [4]. While its 2007 predecessor was largely based on histological and immunohistochemical features, the classification now for the first time takes into account genetic parameters, thereby redefining major tumor entities by “integrating” phenotypic and genotypic parameters for greater diagnostic accuracy [3, 4, 7]. With this nosological shift, newly recognized tumor entities were introduced, whilst others were deleted due to lack of diagnostic and/or biological relevance; furthermore, the classification of diffuse gliomas, medulloblastomas and other embryonal tumors underwent major revisions [4]. While previously all tumors deriving from astrocytes had been grouped together, the new classification incorporates all diffusely infiltrating gliomas, whether of astrocytic or oligodendrocytic ontogeny, into one group of “diffuse gliomas”. This group now includes WHO grade II and III astrocytomas, WHO grade II and III oligodendrogliomas, WHO grade IV glioblastomas, and related diffuse gliomas of childhood [4]. Therewith, diffuse astrocytomas and oligodendrogliomas, which are similar regarding clinical course, therapy, and prognosis as well as genetic alterations despite different cellular ontogenies, are now also nosologically closer together than e.g. diffuse astrocytomas and pilocytic astrocytoma, which differ both clinically and genetically, although they each

derive from astrocytes [4]. Therewith, the new WHO classification of CNS tumors is not only a conceptual, but also a practical improvement over its 2007 precursor [4, 8].

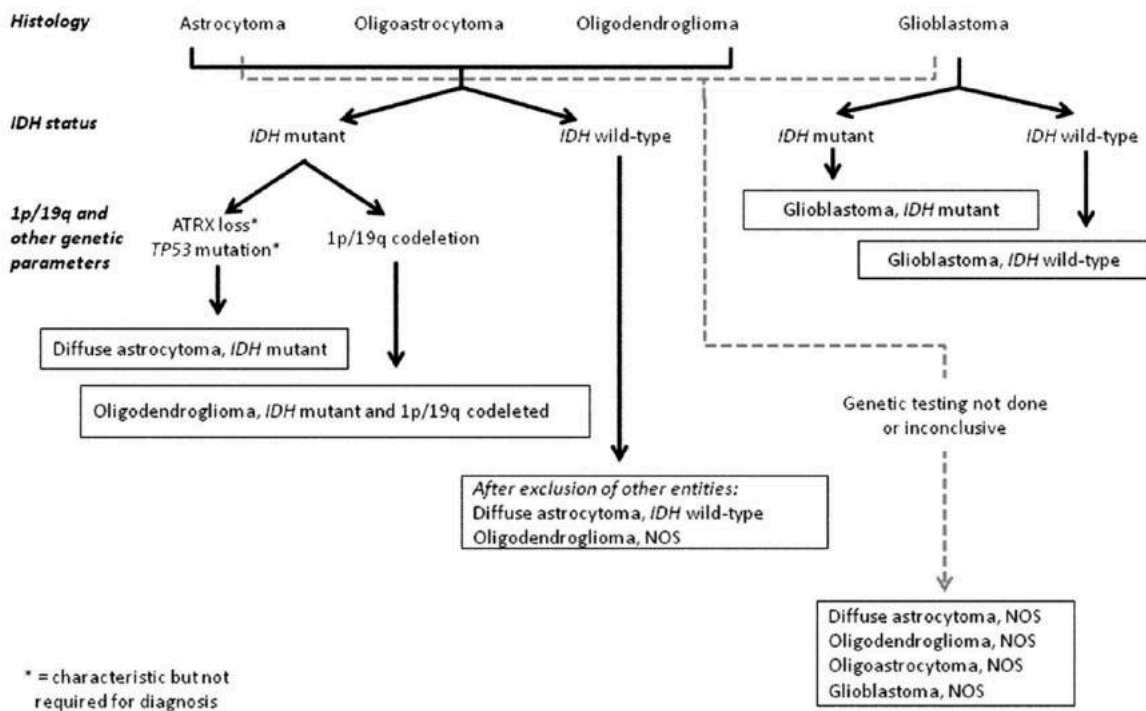


**Fig. 1 Simplified algorithm of the 2016 WHO classification of diffuse gliomas.** Notwithstanding the move towards molecular markers, the classification continues to be organized according to cell of origin, determined by histology, followed by genetic parameters like IDH status, 1p/19q codeletion, TP53 mutation, and ATRX loss. If genetic testing cannot be performed or is inconclusive, the respective tumor entity is classified as not otherwise specified (NOS). Notably, the diagnostic “flow” not necessarily proceeds from histology first to molecular genetic factors next in every case as delineated in this diagram, for molecular signatures can sometimes outweigh histological characteristics in achieving an “integrated” diagnosis. Adapted from [4].

### 1.1.1 Glioblastoma multiforme

Glioblastoma multiforme is a WHO grade IV brain tumor, listed in the group of diffuse gliomas in the 2016 WHO classification (cf. Fig. 1) [4]. It is not only the most malignant but also the most common glioma in adults, accounting for 51,4% of all gliomas [2] and primarily occurring at the age of 55-60 years. It is more often diagnosed in male than in female patients (ratio 1.3:1) and more commonly reported in the western world than in developing countries [9]. Despite its global incidence of less than 10 per 100.000 subjects per year, its extremely poor prognosis makes it one of the leading oncological death causes in the western world and thus a major public health issue [10].

### 1.1.1.1 Clinical presentation and diagnosis

Glioblastomas are usually located in the subcortical white matter in the frontotemporal area of the telencephal cortex [11]. They occur multifocally in only 10% of all cases [12]. Depending on tumor localization, frequent symptoms include aphasia, paresthesia, hemiparesia and vision disorders. Furthermore, convulsions, personality changes as well as symptoms of increased cerebral pressure, such as nausea, emesis and cephalgia, may occur [2]. Said symptoms emerge due to excessive and rapid invasiveness of GBM and consequent compression of adjacent brain parenchyma [10]. As tumor cells infiltrate alongside myelinated tracts, distant cerebral areas are also severely affected. Extracerebral metastases and primary spinal glioblastomas are only seldomly found [13].

Clinically, the tumor often occurs without any known trigger or previous malignant lesion. If so, it is called primary or “de novo” glioblastoma, which is very aggressive and more common in the elderly than in young patients. Only 10% of all GBM occur as a secondary tumor, i.e. as a progression of a WHO grade II or III astrocytoma. Progression from grade II to IV usually takes 5, from grade III to IV 2 years, respectively [14]. Nevertheless, in many cases of diagnosed primary gliomas it remains unclear whether the tumor truly depicts a primary or a secondary GBM, which degenerated from a slowly growing, clinically inapparent lower-grade astrocytoma [3, 4, 15, 16]. Primary glioblastomas most frequently display an IDH-wildtype and are associated with a poor prognosis of 10-15 months, whilst secondary glioblastomas are rather IDH-mutant and linked to a median survival of 2-2,5 years after diagnosis [17, 18]. Accordingly, the 2016 WHO classification of CNS tumors also divides glioblastomas into IDH-wildtype, IDH-mutant, and glioblastomas not otherwise specified, which is reserved for neoplasms whose full IDH status remains unknown (cf. Fig. 1) [4].

In addition to the medical history and clinical-neurological examination, radiographic imaging usually provides the first evidence of a GBM burden [19]. Rapid cell turnover, resulting in insufficient vascular supply, necrosis and, in turn, sprouting of new vessels, is typical in GBM. The radiographic correlate of these features is a ring-enhanced lesion with a necrotic core, a large peritumoral edema and a mass effect in CT and MRI scans with contrast [20]. While GBM presents as a hypo-isointense mass with a central heterogenous signal in the T1 section of MRI scans (see Fig. 2), it is hyperintense in T2 and FLAIR [20]. In PET scans GBM accumulates FDG, leading to a relatively stronger signal in the tumor than in the tumor-free tissue [21]. In angiograms, GBM shows exorbitant pathological vascularization often with early venous drainage [19]. Generally, GBM can present with both a midline shift and a compression of ventricles [2, 22].

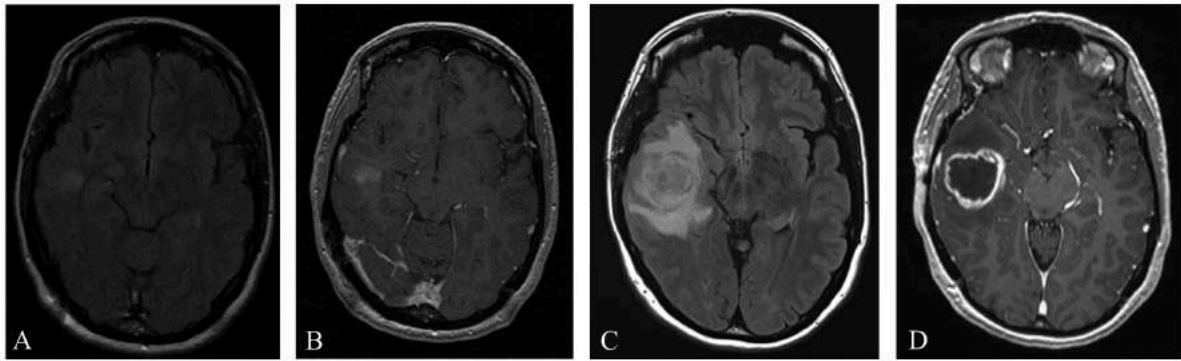


**Fig. 2 Axial MRI scans with contrast of a typical GBM case.** T1 (A, C) and T2 (B, D) weighed. **A, B** Small lesion in the right temporal lobe with faint enhancement and no edema; **C, D** repeated MRI imaging 20 days later shows rapid evolution to a ring-enhanced mass with a necrotic center and vast perilesional edema. Adapted from [19].

The definitive diagnosis of a suspected GBM can only be made by a stereotactic biopsy or craniotomy with tumor resection and a following neuropathological examination, including histology, immunohistochemistry and genetic evaluation [2]. Alongside with diffuse and rapid invasiveness, marked tissue heterogeneity, extensive necrotic areas, hemorrhages and high microvascular proliferation rates are histological characteristics of GBM [23, 24].

### 1.1.1.2 Therapy and prognosis

Initial surgical resection followed by adjuvant radiotherapy with concomitant temozolomide (TMZ) is the gold standard of GBM therapy [25]. However, current therapeutic regimes for GBM have remained palliative up until now, but notably, certain subgroups of patients derive greater benefit from treatment than others [26].

The therapeutic importance of surgical tumor resection is undisputable. Especially fluorescence-guided resection by pre-operative oral administration of 5-aminolevulinic-acid (5-ALA) prolongs progression free survival significantly [27, 28]. 5-ALA induces the accumulation of fluorescent porphyrins selectively in glioma cells and can be imaged intraoperatively under dark light condition, which facilitates tumor recognition and thus leads to more precise resections. Nevertheless, diffuse tumor cell infiltration makes microscopically complete resections (R0 resections) largely impossible causing very high recurrence rates of GBM. In case of recurrent disease, especially radiotherapy is pivotal both in an additive and in a palliative setting. Here, accelerated radiotherapy may be useful [29, 30] in addition to surgical resection of the recurrence.

Local radiotherapy is administered in a dose of 54-60 Gy, if possible 60 Gy in 1,8-2 Gy fractions [31] as part of the standard therapeutic regime. For chemotherapy, TMZ is the first-line agent in glioblastoma therapy. It is an alkylating agent and displays a high oral bioavailability as well as a good penetration of the blood-brain-barrier [32]. A prolonged monotherapy with TMZ for 6 months after standard adjuvant radiochemotherapy may be considered on an individual basis. Also, more recently, Bevacizumab, a humanized recombinant monoclonal antibody against vascular endothelial growth factor (VEGF), has been investigated for GBM therapy but failed in various clinical trials [33-35]. Nevertheless, it has been approved for treatment of recurrent GBM [36]. Generally, the field of GBM therapy has received extensive attention and various new therapeutic approaches have been investigated or are evaluated at the moment [37, 38], including gene [39, 40] and immunotherapies like tumor vaccines [41, 42], CAR T-cell therapy [43], and immune checkpoint inhibitors [44, 45].

Meanwhile various molecular markers and genetic alterations of GBM are known and contribute to an improvement in neuropathological subtype identification, which in turn allows more individualized therapies. Such markers include, for instance, mutations of the IDH-1 and -2 gene and of the telomerase reverse transcriptase (TERT) gene [46], but the highest therapeutic relevance at the moment has the so-called MGMT (O<sup>6</sup>-methylguanine DNA methyltransferase) hypermethylation status [47]. MGMT is a DNA-repair-protein, which specifically eliminates pro-mutagenic alkyl groups of the O<sup>6</sup>-position of guanine. It contributes to cellular resistance against alkylating substances such as TMZ. Promotor hypermethylation leads to a loss of function of MGMT with increased sensitivity to TMZ as a consequence. Patients with positive MGMT hypermethylation status are thus more susceptible to TMZ therapy than those with a negative status, a finding which has been implemented into clinical decision making in elderly (age > 65-70 years) GBM patients [23, 47].

Despite increasingly individualized therapies, a wide range of therapeutic approaches, and substantial efforts in GBM research, prognosis of glioblastoma patients remains very poor with a median survival of only 10-15 months after diagnosis under optimal treatment for IDH-wildtype and 2-2,5 years for IDH-mutant neoplasms [9, 48, 49]. Infiltrative and rapid tumor growth, clonal heterogeneity of tumor cells, and pathologic angiogenesis resulting in a hypoxic and immunosuppressive tumor microenvironment are, among others, features hampering treatment efficacy across many cancers including GBM [23, 26]. Further research on molecular mechanisms of GBM is hence inevitable to improve therapeutic outcomes.

### **1.1.2 Tumor proliferation**

As mentioned above, high-grade gliomas, especially GBM, depict fast growing and thus highly proliferative brain tumors. The individual proliferation rate is assessed for tumor characterization [24]. The most common marker for such an analysis is Ki-67, a DNA-binding nuclear protein, which is expressed throughout the cell cycle, but not in quiescent G0 cells and cells in the early parts of G1 [50]. It is commonly used as an indicator for tumor cell proliferative activity and is associated with the WHO grade of gliomas. Clinically, histological Ki-67 stains (usually conducted with a MIB-1 antibody) of patient material are predictors for individual prognosis regarding low- as well as high-grade-gliomas of children and adults [51].

Besides Ki-67, other markers are used in a pre-clinical context. In animal models, proliferation at a selected time point can be assessed through systemic administration of thymidine analogues, which get incorporated by nascent DNA molecules during replication, followed by antigen retrieval and a respective immunohistochemical staining. For these purposes, 5-Bromodeoxyuridine (BrdU) [52], 5-Chloro- (CldU), 5-Iodo- (IdU) [53] and 5-Ethynyl-2'-deoxyuridine (EdU) [54] are used as thymidine analogues (cf. chapter 3.2.2.3 CldU/IdU treatment and chapter 3.2.5.4 CldU/IdU staining). BrdU may also be utilized on human samples through intraoperative application, as it does not affect cell cycle if it is administered in the minimal doses needed for imaging [55, 56]. In human as well as mouse tissue it has been shown that labeling indices display a high variability in gliomas ranging from 0.3 to 19.1%, depending on, among other factors, their WHO grade [55].

Unusual vascular proliferation is one of the distinctive predicates of glioma, especially of glioblastoma multiforme [24]. While the BrdU labeling index of tumor-associated endothelial cells in physiological, tumor-free areas is  $< 0,05\%$ , it increases exorbitantly to  $36 \pm 2,4\%$  in glioma tissue as shown by Payton et al. 2014 [57]. This severely enhanced endothelial cell proliferation raises the question of the molecular mechanisms of tumor angiogenesis in gliomas.

### **1.1.3 Tumor angiogenesis and Apelin/APJ signaling**

Blood vessels throughout the body form a sufficient transport system for oxygen, nutrients, immune cells, growth factors and waste elimination [58]. In contrast to vasculogenesis, i.e. the emergence of vessels from endothelial precursor cells during embryonic development, angiogenesis means the genesis of new vasculature from pre-existing vessels in order to vascularize tissue [59]. It is mainly a phenomenon of fetal and embryonic development, but also occurs during postnatal tissue growth. Several mechanisms of angiogenesis have so far

been investigated, including sprouting of capillaries from pre-existing vessels, splitting of pre-existing vessels by transcapillary pillars or posts of extracellular matrix (intussusception) and fusion of capillaries to vessels with an increased diameter, all of which may occur at the same time in one tissue [60].

In highly proliferative tissues with an exorbitant metabolic turnover, such as in malignant tumors like GBM, thorough vascularization is pivotal for ample nourishment [61]. Malignant neoplasms can only grow to a diameter of 1-2 mm without tumor angiogenesis, being solely sustained by diffusion of oxygen and nutrients through the adjacent tissue [62, 63]. In this state, the so-called “tumor dormancy”, tumor progression is usually clinically inapparent. For further cancer progression, angiogenesis needs to be induced [64]. Angiogenesis is thus a hallmark of cancer as well as its inhibition promises opportunities for potent therapies [65, 66].

However, tumor angiogenesis does not only implicate an increment of newly formed vasculature. It also causes changes of tumor micro-milieu due to aberrancy of tumor vessels [67, 68]. Their endothelium is often inhomogeneous with endothelial cells growing on top of each other into the lumen and sometimes depicts a mosaic of endothelial and tumor cells. Tumor vessels are unorganized, dilated, varying in their diameter, and even lacking a lumen in some cases [67]. Ramifications and blind ends can be perpetually found leading to an irregular blood flow. Transendothelial leakage, intraendothelial gaps, vesicles, and fenestrations are ultrastructural features of tumor endothelium [68]. Since a basal membrane is often lacking, hematogenous metastasis is facilitated [69]. Moreover, plasma can easily extravasate leading to an increased hydrostatic pressure in the neoplastic tissue. Smaller vessels in the tumor are consequently compressed causing central tumor necrosis [70]. The latter can also be a consequence of exorbitant tumor cell proliferation without a sufficient induction of angiogenesis. Consequent intratumoral hypoxia then effects acidosis including an increased oxygen and carbon dioxide pressure, which leads to aggravated transport of required substances [71]. Tumor progression, immune escape, metastasis and, most importantly, response to anticarcinogenic therapies are decisively affected by the described processes [72].

With exception to the female reproductive organs [73] and tissue repair [74], postnatal endothelial cells physiologically remain quiescent as phalanx cells. In this homeostatic state, pro- and anti-angiogenic factors are balanced in equilibrium [75]. If pro-angiogenic factors prevail due to secretion by tumor cells, said equilibrium is abolished and vascularization is induced. This “angiogenic switch” in malignancies is influenced by a variety of angiogenic factors [76]. In an oncological context, the most prominent inducing factor is Vascular Endothelial Growth Factor A (VEGF-A), a glycoprotein of the large VEGF family, which binds

its tyrosine kinase type III receptor (VEGFR) i.a. on endothelial cells [77, 78]. Besides endothelial cells, also pericytes and vascular smooth muscle cells (VSMCs) are involved in tumor angio- as well as arteriogenesis [79].

One recently identified mechanism of tumor-vessel-generation is the Apelin/APJ signaling pathway [80, 81]. Apelin is the natural ligand of APJ, a 7-transmembrane G-protein-coupled receptor [82]. The Apelin gene encodes a secreted preprotein (77 amino acids with a signal peptide, a predomain, and a C-terminal peptide) in mammals. After proteolytic maturation it generates a number of Apelin polypeptides [82], of which Apelin-36 (comprised of amino acids 42-77) and Apelin-13 (comprised of amino acids 65-77) are the predominant and most active isoforms [82, 83]. It was suggested that Apelin signaling functions downstream of VEGF-A [84]. APJ is structurally related to the angiotensin II receptor type I (AT1R) [85]. However, angiotensin 1 (AT1) does not bind APJ [82].

Apelin and APJ are expressed in the adult brain and in the periphery, particularly in the gastrointestinal tract, adipose tissue, lung, kidney, liver, and skeletal muscle [86]. They are known to play an essential physiological role in the regulation of blood pressure and cardiac contractility [87]. Regarding embryonic cardiovascular development, previously reported findings are heterogeneous but suggest an important role of Apelin and APJ [88, 89]. In retinal blood vessels they may function as regulators of angiogenesis during postnatal development [90]. Also, recent studies have shown that Apelin is expressed and associated with angiogenic blood vessel growth, where it acts via autocrine and paracrine mechanisms [84]. Apelin/APJ signaling is necessary and sufficient to promote angiogenic blood vessel growth *in vivo*. Most importantly, Apelin/APJ were shown to have an important impact on tumor angiogenesis in GBM [84]. Nevertheless, as of yet it was postulated that they interact with endothelial cells, but not with other cells involved in angiogenesis, such as pericytes.

#### **1.1.4 Anti-angiogenic therapies**

For oncological therapies, angiogenic signal transduction pathways offer multiple potential targets for inhibition of tumor angiogenesis. In contrast to conventional chemotherapeutics, anti-angiogenic therapies do not focus on direct depletion of malignant cells, but on the potential of “normalizing” pathologic tumor vasculature in order to both inhibit tumor nourishment as well as removal of metabolites and to improve antitumoral drug delivery [72]. They aim for a reestablishment of the physiological equilibrium of pro- and anti-angiogenic factors [91].

Anti-angiogenic substances usually target the basal membrane, endothelial cell migration and proliferation, or cell matrix interactions [75]. Especially molecules targeting the signal transduction of receptors are in the spotlight of clinical research, including both antibodies directly binding the receptor and substances interacting with the intracellular pathway. The most investigated anti-angiogenic agent in GBM is Bevacizumab, a humanized monoclonal antibody inhibiting VEGF [78, 92]. However, if implemented into different therapeutic regimes, it has indeed increased progression free survival in recurrent GBM if administered in combination therapy with Lomustine, but has failed to prolong overall survival of GBM patients [35, 93]. Also, drug resistance by evasion of VEGF inhibition has been reported to occur in various preclinical settings [94, 95]. There is, thus, an urgent need for alternative, anti-angiogenic drug targets, for which not only endothelial cells but also pericytes may be considered.

## **1.2 Pericytes**

Pericytes are the perivascular, mural cells of the microvasculature [96]. The term microvasculature includes arterioles, capillaries, and venules [97]. Historically, pericytes were called Rouget-Cells due to their discovery by Charles Rouget in 1873 [98] and later renamed ‘pericytes’, because of their perivascular location [99]. Now, more than a century after their discovery, pericyte biology is still only poorly understood [100].

In the literature, pericytes are often compared with vascular smooth muscle cells (VSMCs), the perivascular, mural cells found in larger vessels. Sometimes they are even regarded as their microvascular counterparts [96], although their histologic features and functional spectrum remain quite different.

### **1.2.1 Definition and characteristics**

In contrast to VSMCs, pericytes are commonly defined as cells within the vascular basal membrane (BM) that is seamlessly merged with the BM of endothelial cells [101]. This applies to the vast majority of the pericyte-endothelial cell interface. In distinct places, however, the BM is disrupted and provides direct contact points between pericytes and endothelial cells. Also, BM coverage may be incomplete or even absent in some parts of the microvasculature [102]. Especially during embryonic development or in pathological conditions, for instance in tumor vasculature, the BM is typically aberrant [103]. Identification of pericytes by their location within the BM under these conditions is, hence, difficult and rather relies on labelling of pericyte markers as described in chapter 1.2.3 [100].

Pericytes are attached to capillaries and embrace the vasculature with multiple extensions [96]. Their processes span several endothelial cells and occasionally even bridge neighboring capillary branches. They are virtually encircling the vessel as secondary branches extend from primary branches in a usually perpendicular orientation. At capillary branch points, they are often found to extend primary processes alongside each branch, forming a cellular Y-shape. They typically maintain round nuclei and cover the microvasculature in a single layer [100].

Pericyte density and the proportion of the endothelial abluminal surface that is covered by them varies between different organs. The CNS displays the highest pericyte density with a 1-3:1 endothelial-cell-to-pericyte ratio [101, 104, 105]. The lowest pericyte density can be found in skeletal muscle tissue, which has been reported to have a 100:1 endothelial-cell-to-pericyte ratio [102, 104]. Although evidence for variations of density is decidedly strong, the latter ratio relies on few studies [96]. A more conservative estimate of variation would be that endothelial-to-pericyte ratio varies between 1:10 and 1:1 and that abluminal surface coverage ranges between 70% and 10% [101]. Pericyte coverage hereby correlates positively with endothelial barrier capacities (large coverage in the CNS, low coverage in skeletal muscle tissue), endothelial cell turnover (large coverage coincides with less turnover), and orthostatic blood pressure (large coverage in lower body parts) [100-102].

Regarding the microvasculature of all organs, pericyte coverage is most dense in capillaries and postcapillary venules [100]. Regarding lymphatic capillaries, pericytes are absent in physiological conditions. In pathologies, lymphatic capillaries may attract ectopic pericytes [106].

### **1.2.2 Functions**

As correlations between pericyte coverage and functional differences of organ-specific microvasculature suggest, pericytes are vital regulators of the vasculature.

The most prominent function of pericytes is their contribution to the development and maintenance of the endothelial barrier, particularly in the CNS [96]. Here, the so-called blood-brain-barrier (BBB) tightly regulates CNS homeostasis, which is pivotal for proper neuronal function and protection from toxins, pathogens, inflammatory agents, injury, and disease [107]. It controls the movement of molecules, ions, and cells between the blood and the CNS [108, 109]. The BBB is an idiom used to describe these unique properties of the CNS vasculature [96]. It is composed, from inside out, of endothelial cells closely attached to each other by tight junctions, a non-fenestrated BM, pericytes, and astrocyte endfeet [107]. Together with

microglia and neurons, the cells of the BBB form the so-called functional neurovascular unit (NVU) [110]. Several *in vivo* experiments have shown that pericyte loss is associated with insufficient BBB development during embryogenesis [111], a BBB breakdown in adult organisms [112], and aberrant BBB permeability [111, 112]. They are, hence, vital components of both the BBB and the NVU [113]. They not only stabilize vessels, but also actively interact with endothelial cells and play an important role in the formation as well as degradation of the BM [114].

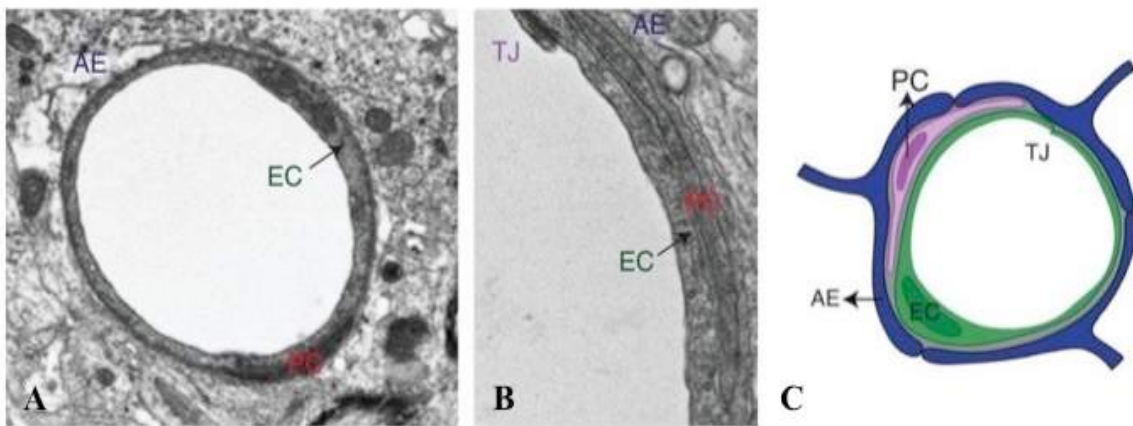


**Fig. 3 Pericytes as components of the BBB.** **A** Electron micrograph (EM) of a cross section of a typical CNS vessel illustrating the relationship between endothelial cells (EC), pericytes (PC) and astrocyte endfeet (AE). Both EC and PC are embedded within the vascular BM. **B** Magnified EM showing tight junctions (TJ) between ECs (arrow). **C** Schematic representation of the BBB. Adapted from [107].

Just like VSMCs in larger vessels, pericytes were shown to regulate vasodilatation and vasoconstriction in capillaries [96, 115]. Desmin and  $\alpha$ -smooth-muscle-actin ( $\alpha$ SMA) are subcellular structural proteins, which are typically expressed in many pericytes and thus serve as standard pericyte markers as described in chapter 1.2.3 [100, 116, 117]. By contributing to actin filament bundles located near the endothelial cell side of pericytes they have a contractile function [118]. A variety of vasoactive circulatory ligands mediate this process by interacting with pericytes. For instance, Serotonin, Histamine, Angiotensin 2, Endothelin-1, and adrenergic agonists lead to pericyte-induced vasoconstriction, while nitric oxide, carbon dioxide, and cholinergic agonists cause pericyte-induced vasodilatation via up- or down-regulation of intracellular calcium levels, respectively [119]. Studies suggest that especially pericytes located in the transition zone of arterioles to capillaries have a contractile function [120]. It is to be mentioned, however, that not all pericytes do so. Some authors even refer to pericytes as, by

definition, non-contractile, while others clearly name contractility as one of their defining features [96].

Pericytes can not only serve as [pre-] capillary sphincters, but also and most importantly mediate angiogenesis [96]. During the initial phase of angiogenesis, activated pericytes produce matrix metalloproteinases (MMPs), including MMP2, MMP3, and MMP9, to degrade the BM [121]. By this process, endothelial cells can detach and migrate to the extracellular matrix lead by a gradient of chemotaxins. Detachment of endothelial cells from pericytes and from the BM is led by so-called endothelial tip cells. Neighboring endothelial cells follow the endothelial tip-cells to form endothelial stalk-cells, which, in turn, elongate the newly formed vessel sprout by vascular proliferation [96]. These newly formed vessels are highly instable. To inhibit disintegration of the vessel, endothelial cells secrete chemokines, e.g. platelet derived growth factor  $\beta$  (PDGF $\beta$ ), which recruits pericytes for vascular stabilization [122, 123]. Platelet derived growth factor receptor  $\beta$  (PDGFR $\beta$ ), the receptor of PDGF $\beta$ , is widely expressed by pericytes [100]. These PDGFR $\beta$  positive pericytes were shown to migrate from adjacent vasculature, to be recruited from the bone marrow, or to derive from cells that differentiate from surrounding mesenchymal precursors [123, 124]. The impact of the PDGFR $\beta$  pathway in the recruitment of pericytes during angiogenesis was demonstrated by Hellström et al., as they have shown that in PDGF $\beta$  and PDGFR $\beta$  knockout mice pericyte coverage is lacking, leading to endothelial hyperplasia as a consequence [125].

### 1.2.3 Markers

Increased interest in pericyte research and the impossibility of location-based pericyte identification in many pathological conditions has sparked research on specific pericyte makers. Standard pericyte markers include neuron-gial 2 (NG2) [126-128], PDGFR $\beta$  [129-131], CD 146 [130, 131], Endoglin (CD 105) [122] and Aminopeptidase A and N (CD 13) [132, 133] as membrane-bound markers [96]. The cytosolic markers  $\alpha$ SMA [122, 134], non-muscle myosin [122], Nestin [122, 130-132, 135], Desmin [100, 117, 122, 131], and Vimentin [134] also allow proper pericyte identification even in pathological conditions such as in tumors (cf. Tab. 1) [96]. Tab. 1 provides an overview of pericyte markers.

In addition to the markers listed in Tab. 1, pericytes were shown to express i.a. CD90, CD44, CD73 and CD105, surface markers usually found in mesenchymal stem cells (MSCs) [136, 137]. MSCs are regenerative cells, as they are able to differentiate to adipocytes, chondrocytes and osteocytes [136]. Interestingly, pericytes also show similar differentiation

capacities as MSCs, as they display adipogenic, osteogenic, and chondrogenic potential in vitro, and were shown to form calcified tissue in vivo [130].

Expressed in:	Pericytes	VSMCs	Arterioles	Capillaries	Venules	Remarks
<i>Cytosolic markers</i>						
Alpha-smooth muscle actin ( $\alpha$ SMA)	+	+	+	-	+	Most frequently used and best characterized. Also a marker for VSMCs.
Non-muscle myosin	+	-	-	+	+	Present in relatively high concentration in capillary pericytes, absent in VSMCs.
Tropomyosin	Unknown	+	-	+	+	Part of the actin cytoskeleton.
Desmin	+	+	+	+	+	Useful marker in tissues other than skeletal muscle and heart tissue. Expressed on intermediate filament proteins in pericytes that are in direct contact with underlying endothelium. Also expressed by VSMCs.
Vimentin	+	+	+	+	+	Component of intermediate filaments.
Nestin	+	+	+	+	+	An intermediate filament protein that is expressed mostly in nerve cells during early stages of development. In adulthood replaced by tissue specific intermediate filaments in mural cells.
Regulator of G protein signalling 5 (RGS5)	+	+	+	+	+	Tested in PDGFR $\beta$ - or PDGF- $\beta$ deficient mice. Marker for developing pericytes independent of PDGF- $\beta$ signalling.
<i>Membrane bound markers</i>						
Platelet-derived growth factor receptor $\beta$ (PDGFR $\beta$ )	+	+	+	+	+	Expressed by developing pericytes and precursor pericytes. Also a tyrosine kinase receptor important for pericyte function.
CD146	+	+	+	+	+	Transmembrane glycoprotein. EC antigen also expressed at the surface of pericytes and in larger blood vessel types.
Aminopeptidases A and N (CD13)	+	+	+	+	+	Type II membrane zinc dependent metalloproteases.
Endoglin (CD105)	Unknown	+	+	+	+	TGF- $\beta$ 1 co-receptor required for angiogenesis. Also a marker for ECs.
Neuron-glia 2 (NG2)	+	+	+	+	-	Broadly expressed in pericyte population, expressed during vascular morphogenesis. Also expressed by larger blood vessel types, and by oligodendrocytes.

**Tab. 1 Overview of established pericyte markers.** Adapted from [96].

However, pericyte markers are not expressed by every pericyte in every organ or tissue and neither one of them is completely specific [96, 100]. This may be a result of pericyte plasticity, as pericytes express different markers in different organs and tissues at different development stages as well as at different microvascular locations. For instance,  $\alpha$ SMA is only found in contractile pericytes and Nestin is often regarded as only being present in some pericyte subforms [135]. Due to this heterogeneity, pericytes are not identifiable by one single marker. A state-of-the-art identification of pericytes rather relies on co-labelling of several pericyte markers and counter-labelling of endothelial cells [100].

### 1.2.4 Subtypes

As delineated above, some pericytes have an angiogenic potential. So far, it is often claimed that such a potential is especially displayed by pericytes that do not express  $\alpha$ SMA and are

therewith not involved in vasoconstriction [96, 100]. In more recent studies, Nestin and NG2 instead of  $\alpha$ SMA were used as markers for pericyte subtype identification [135, 138].

Bibrair et al. identified two different pericyte subtypes by their marker profile, namely type-1 and type-2-pericytes [135, 138-140]. While type-1-pericytes express NG2 but not Nestin, type-2-pericytes are both NG2 and Nestin positive. Both pericyte subtypes play diverse roles in different microenvironments: Type-1-pericytes are fibrogenic and adipogenic in old and diseased skeletal muscle; type-2-pericytes are able to generate new muscle tissue after injury [139]. According to Bibrair and colleagues, type-2-pericytes also exhibit characteristics of neural progenitor cells such as morphology, specific neural marker profile, replicative capacity, ability to form neurospheres, and functional response to neurotransmitters [140]. Even more astonishingly, it was shown that only type-2, but not type-1-pericytes foster angiogenesis in vitro as well as in vivo in a matrigel plug assay [135]. In a model for hindlimb ischemia, only type-2-pericytes recover blood flow [135]. Most interestingly, during tumor angiogenesis only type-2-pericytes are recruited [135]. Specific inhibition of type-2-pericytes might, thus, lead to a targeted antiangiogenic tumor therapy, as physiological pericyte functions remain unimpaired.

### 1.2.5 Ontogeny

From a range of lineage-tracing studies it is known that pericytes have multiple developmental origins [100].

In the CNS, the majority of vascular mural cells are probably neural crest derived [141-143]. This also applies to vascular mural cells in the thymus [144, 145]. The cells of the neural crest, in turn, are of an ectodermal provenance [100]. In coelomic organs, such as the gastrointestinal tract, the liver, the lung, and the heart, vascular mural cells derive from the mesothelium, the single-layered squamous epithelium that lines coelomic cavities and its organs [100, 146]. The mesothelium, in turn, rises from the mesoderm [100]. Despite said common ectodermal or mesodermal origin, the signaling mechanisms that govern pericyte recruitment to their final perivascular location may differ from organ to organ [96]. For instance, PDGF $\beta$ /PDGFR $\beta$  signaling has been demonstrated to mediate pericyte recruitment in the CNS [147]. In the thymus, however, pericytes are recruited independently of this signaling pathway, albeit in both organs pericytes derive from the neural crest [144]. Also, literature suggests a close ontogenetic relationship between vascular mural cells and fibroblasts [100].

In a non-embryonic setting, the ontogeny of pericytes remains largely elusive [100] and finding a pericyte precursor or lineage is still subject of further investigation.

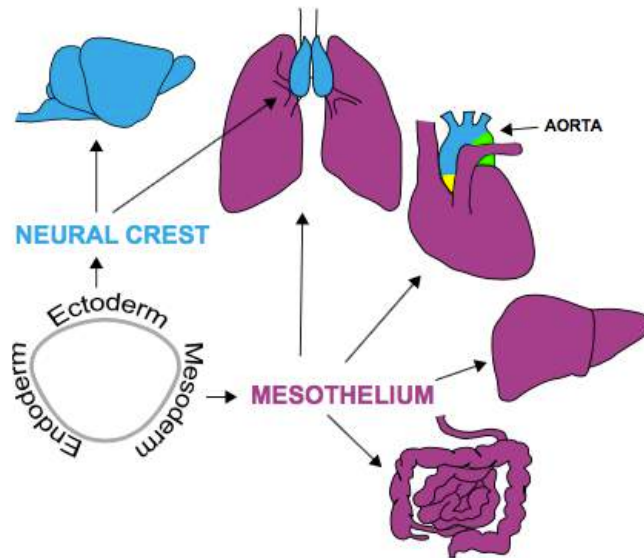


**Fig. 4 Embryonal ontogeny of vascular mural cells.** While vascular mural cells of the CNS and the thymus are derived from the neural crest (indicated in blue, ectoderm), the mesothelium (indicated in purple, mesoderm) gives rise to vascular mural cells of the lung, the heart, the liver, and the gastrointestinal tract. Regarding the aorta, vascular mural cells have multiple developmental origins: They derive from the secondary heart field (indicated in yellow), the neural crest, and the somite (indicated in green). Adapted from [100].

### 1.2.6 Pericytes in gliomas

Pericytes are involved in a variety of pathological conditions, especially in vascular and fibrotic diseases such as diabetic retinopathy and liver fibrosis, but also in wound healing [96] and neurological illnesses, such as stroke [148] and Alzheimer's disease [149]. In oncological conditions, pericytes mediate tumor vascularization [100]. In addition to immune cells, fibroblasts, extracellular matrix molecules and endothelial cells, they are vital parts of the tumor microenvironment [65]. In the following, pericytes located in tumors are referred to as tumor-associated pericytes.

Just as in physiological angiogenesis, pericytes are recruited into tumor blood vessels by PDGF $\beta$ /PDGFR $\beta$  signaling [150]. More recent reports suggest an additional role of HB-EGF in pericyte recruitment to tumor vasculature in a model of pancreatic carcinoma [151] and of EGFR $^{+}$  pericytes in the development of resistance against antiangiogenic therapy in a model of lung cancer [152]. Generally, signaling pathways for pericyte recruitment to tumor tissue was suggested to be tumor-type-specific [100, 153].

Whereas pericytes are attracted to the tumor via similar signaling pathways as in physiological conditions, pericyte coverage of tumor vasculature is clearly aberrant and generally decreased. In tumors, pericytes are only loosely attached to the endothelium and form cytoplasmatic processes that penetrate deep in the tumor parenchyma [70]. These alterations

may be explained by hypoxia-driven upregulation of VEGF-A expression in tumor cells. VEGF-A fosters endothelial sprouting and neovascularization but is inefficient in forming a sufficient vascular network and inhibits pericyte function as well as vessel maturation [154].

The ontogeny of tumor-associated pericytes remains largely unknown [100]. According to Abramsson et al., they may be recruited from local immature mesenchymal cells [155]. Other studies suggest that tumor-associated pericytes migrate from the bone marrow into respective neoplasms [156, 157], as in higher-grade CNS tumors the BBB is disrupted making such a migration theoretically possible [24]. Generally, it is assumed that tumor-associated pericytes are recruited from pericytes in physiological, probably tumor-adjacent tissue and that both of them express typical pericyte markers, including NG2, Desmin, and PDGFR $\beta$  (cf. Fig. 5) [100]. However, a specific pericyte progenitor or lineage has not been identified so far neither in a physiological nor in an oncological setting.

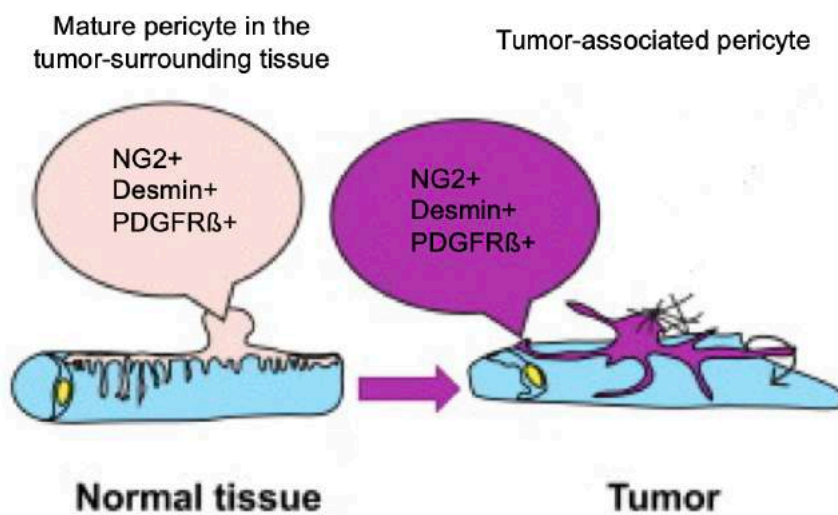


**Fig. 5 Common model of the ontogeny of tumor-associated pericytes.** Literature suggests that tumor-associated pericytes derive from mature pericytes in the tumor-surrounding tissue. Both of them display the same typical pericyte markers, namely NG2, Desmin, and PDGFR $\beta$ . However, scientific evidence for this commonly assumed model has never been provided. Adapted from [100].

### 1.2.7 Anti-angiogenic therapies targeting pericytes

The tumor microenvironment provides ample potential targets for therapy strategies [158]. Regarding antiangiogenic therapies, pericytes are promising targets since they are involved in i.a. tumor vessel stabilization and angiogenesis, as described earlier.

Recent analysis of the cause of resistance to antiangiogenic therapies suggested that pericytes protect the endothelium in situations of VEGF-A inhibition [100]. VEGF-A ablation

in fact caused selective elimination of tumor vasculature that lacked pericyte coverage, as shown by Benjamin and colleagues [159]. To target both pericyte-covered and pericyte-lacking vessels more effectively, combined antiangiogenic therapies directed against endothelial cells as well as against pericytes were proposed to have an increased antitumoral effect compared to single-targeted antiangiogenic regimes [160, 161]. Especially in conditions, which showed to be resistant to conventional endothelium-targeted antiangiogenic therapies, regimes focusing on pericytes may be promising [100]. Further investigations on pericyte biology, particularly on tumor-associated pericytes in fatal oncological diseases like high-grade gliomas, are hence pivotal to provide a thorough foundation for future antiangiogenic therapies.

## 2. Objectives

Glioblastoma multiforme is the most common and most aggressive primary brain tumor in adults with a very poor prognosis despite therapy. GBM is characterized by an exorbitant neo-vascularization, for which pericytes play a pivotal role. However, the lineage of such tumor-associated pericytes remains largely elusive up until now. In this study, a NesCreER<sup>T2</sup> x Ai9tdTomato double transgenic mouse model was established which allowed re-investigating the lineage of pericytes in tumor-initiated neo-angiogenesis in the CNS. The objectives of the doctoral thesis at hand are as follows:

- (1) To trace the cells of the pericyte-lineage throughout glioma angiogenesis in vivo;
- (2) To delineate the cells of the pericyte-lineage regarding their morphological development;
- (3) To investigate the proliferation of the cells of the pericyte-lineage using a CldU/IdU labeling protocol;
- (4) To characterize the cells of the pericyte-lineage concerning their perivascular localization, their pericyte marker profile, their development into pericyte subtypes, and their expression of Apelin/APJ.

### 3. Materials and methods

#### 3.1 Materials

##### 3.1.1 Lab devices

Lab device	Supplier
Axio Observer A1 inverse fluorescence microscope	Carl Zeiss Microscopy GmbH, Jena, Germany
Axioskop 2 light microscope	Carl Zeiss Microscopy GmbH, Jena, Germany
Axiovert 135 TV fluorescence microscope	Carl Zeiss Microscopy GmbH, Jena, Germany
Axiovert 25 fluorescence microscope	Carl Zeiss Microscopy GmbH, Jena, Germany
BMS D1-223A light microscope	Breukoven b. v., Capelle aan den IJssel, Netherlands
Broadband confocal microscope TCS SP5	Leica Microsystems Vertrieb GmbH, Wetzlar, Germany
Digital Vortex mixer	VWR, Radnor, Pennsylvania, USA
DOSE IT peristaltic pump	Integra Biosciences AG, Zizers, Switzerland
Hera safe hood	Thermo Fisher Scientific, Waltham, MA, USA
Heraeus Multifuge 1S Centrifuge	Thermo Fisher Scientific, Waltham, MA, USA
Magnetic Hotplate Stirrer VMS-C7-2	VWR International GmbH, Darmstadt, Germany
Microliter syringe	Hamilton Company, Reno, NV, USA
MS2 minishaker	IKA, Staufen, Germany
Pipet Boy Comfort	Integra Biosciences AG, Zizers, Switzerland
Pipettes (0-10, 20-200, 100-1000 µl)	Eppendorf AG, Hamburg, Deutschland
Sea Star Shaker	Biozyme Scientific GmbH, Oldendorf, Germany
Slide 2003 Microtome	Pfm Medical, Cologne, Germany
Stereotactic Frame	Stoelting Co., Wood Dale, IL, USA
Water bath	Memmert GmbH + Co. KG, Schwabach, Germany
WTW Multical bench pH Meter (pH 526)	Sigma-Aldrich, Saint Louis, MO, USA

**Tab. 2 Lab devices.**

##### 3.1.2 Lab consumables

Lab consumable	Supplier
Costar Stripettes (5, 10 and 25 ml)	Corning Incorporated, Corning, NY, USA
Dako Pen	Dako Germany, Hamburg, Germany
Drying block	Whatman GmbH, Dassel, Germany

Eppendorf tubes (0.5, 1 and 2 ml)	Eppendorf AG, Hamburg, Germany
Falcon tubes (15 and 50 ml)	VWR International GmbH, Darmstadt, Germany
Microscope cover slips (24 x 50 mm)	Gerhard Menzel GmbH, Braunschweig, Germany
Parafilm	Biozym Scientific GmbH, Hessisch Oldendorf, Germany
Pipette tips (0-10, 20-200, 100-1000 µl)	Eppendorf AG, Hamburg, Germany
Plates (12 wells, 24 wells)	TPP Techno Plastic Products AG, Trasadingen, Switzerland
Superfrost Ultra Plus microscope slides	Thermo Fisher Scientific, Waltham, MA, USA
Surgical instruments	Medizinisches Lager Klinikum der Universität München, Munich, Germany
Syringes BD Discardit II (5 and 10 ml)	Becton Dickinson, Franklin Lakes, NJ, USA

**Tab. 3 Lab consumables.**

### 3.1.3 Reagents and chemicals

Reagent/chemical	Supplier
Antibody diluent serum-free with background reducing components	Dako Germany, Hamburg, Germany
Aqua ad iniectabilia	B. Braun Melsungen AG, Melsungen, Germany
Bepanthen® Eye- and Nosecream	Bayer HealthCare, Leverkusen, Germany
CldU	Sigma-Aldrich, Saint Louis, MO, USA
Cryomatrix	Thermo Fisher Scientific, Waltham, MA, USA
Donkey serum	Sigma-Aldrich, Saint Louis, MO, USA
DAPI	Sigma-Aldrich, Saint Louis, MO, USA
Entellan® mounting medium	Merck, Darmstadt, Germany
Eosin G-solution 0.5%	Carl Roth GmbH + Co. KG, Karlsruhe, Germany
Ethylenglycol	Sigma-Aldrich, Saint Louis, MO, USA
EtOH 100%	Apotheke Klinikum der Universität München, Munich, Germany
EtOH 70%	Apotheke Klinikum der Universität München, Munich, Germany
EtOH 96%	Apotheke Klinikum der Universität München, Munich, Germany
Glycerol	Sigma-Aldrich, Saint Louis, MO, USA
Goat serum	Sigma-Aldrich, Saint Louis, MO, USA
HCl	Sigma-Aldrich, Saint Louis, MO, USA
Hoechst 3342 (1:1000)	Life Technologies, Darmstadt, Germany

IB4 biotinylated (1:100)	Vector Laboratories, Burlingame, CA, USA
IB4 FITC (1:200)	Sigma-Aldrich, Saint Louis, MO, USA
IdU	Sigma-Aldrich, Saint Louis, MO, USA
Ketaminhydrochlorid (Ketavet, 100 mg/ml) injection solution	Pfizer, New York City, NY, USA
Meyer's Hemalaun	Carl Roth GmbH + Co. KG, Karlsruhe, Germany
Mounting medium for fluorescence microscopy	Ibidi, Martinsried, Germany
Na <sub>2</sub> HPO <sub>4</sub>	Sigma-Aldrich, Saint Louis, MO, USA
NaH <sub>2</sub> PO <sub>4</sub>	Sigma-Aldrich, Saint Louis, MO, USA
PBS	Apotheke Klinikum der Universität München, Munich
PFA	Sigma-Aldrich, Saint Louis, MO, USA
Protein block	Dako Germany, Hamburg, Germany
Rompun (2%) & Xylazin injection solution	Bayer Vital GmbH, Leverkusen, Germany
Roti® Histol	Carl Roth GmbH + Co. KG, Karlsruhe, Germany
Sodium Tetraborate decahydrate	Sigma-Aldrich, Saint Louis, MO, USA
Sucrose	Sigma-Aldrich, Saint Louis, MO, USA
Tamoxifen	Sigma-Aldrich, Saint Louis, MO, USA
Triton X-100	Roche Diagnostics GmbH, Rotkreuz, Switzerland
Tween-20	Sigma-Aldrich, Saint Louis, MO, USA

**Tab. 4 Reagents and chemicals.**

### 3.1.4 Cell lines

Cell line	Supplier
GL261 murine glioma cell line	National Cancer Institute, NCI-Frederick, MD, USA

**Tab. 5 Cell lines.**

### 3.1.5 Antibodies and streptavidin-conjugated flourophores

Primary antibodies						
Antigen	Host	Isotype	Conjugation/ Biotinylation	Dilution	Catalog number	Supplier
Apelin	Rabbit	IgG	-	1:100	ab59469	Abcam, Cambridge, UK
Apelin (C12)	-	-	-	1:20	-	ScFv antibody from D. Neri

APJ	Rabbit	IgG	-	1:100	ab66218	Abcam, Cambridge, UK
CD31	Rat	IgG	-	1:50	550274	Becton Dickinson, Heidelberg, Germany
CldU & BrdU	Rat	IgG	-	1:250	MCA2060T	Abd Serotec, Kidlington, UK
Desmin	Rabbit	IgG	-	1:200	ab15200	Abcam, Cambridge, UK
Iba1	Rabbit	IgG	-	1:500	019-19741	Wako Pure Chemicals, Neuss, Germany
Iba1	Goat	IgG	-	1:500	ab5076	Abcam, Cambridge, UK
IdU & BrdU	Mouse	IgG	-	1:750	347580 (7580)	Becton Dickinson, Franklin Lakes, NJ, USA
Myc tag (ChIP grade)	Goat	IgG	-	1:100	ab9132	Abcam, Cambridge, UK
Nestin	Mouse	IgG	-	1:100	MAB353	Merck Millipore, Darmstadt, Germany
NG2	Rabbit	IgG	-	1:200	ab5320	Abcam, Cambridge, UK
PDGFR $\beta$	Goat	IgG	-	1:50	AF1042	R+D Systems, Minneapolis, MN, USA
RFP	Rabbit	IgG	-	1:200	ab62341	Abcam, Cambridge, UK
vWF	Rabbit	IgG	-	1:400	A0082	Dako Germany,

						Hamburg, Germany
--	--	--	--	--	--	---------------------

**Tab. 6 Primary antibodies.**

Secondary antibodies						
Antigen	Host	Isotype	Conjugation /Biotinylation	Dilution	Catalog number	Supplier
Goat IgG	Donkey	IgG (H+L)	Alexa Fluor 488	1:125	705-545- 147	Dianova, Hamburg, Germany
Mouse IgG	Donkey	IgG (H+L)	Cy <sup>TM</sup> 2	1:250	715-225- 150	Jackson Immuno- Research, West Grove, PA, USA
Mouse IgG	Donkey	IgG (H+L)	Cy <sup>TM</sup> 5	1:500	715-175- 150	Jackson Immuno- Research, West Grove, PA, USA
Rabbit IgG	Goat	IgG (H+L)	Alexa Fluor 488	1:500	A11034	Life Technologies, Carlsbad, CA, USA
Rabbit IgG	Donkey	IgG (H+L)	Alexa Fluor 594	1:500	711-585- 152	Jackson Immuno- Research, West Grove, PA, USA
Rabbit IgG	Donkey	IgG (H+L)	biotinylated	1:250	711-545- 152	Jackson Immuno- Research, West Grove, PA, USA
Rabbit IgG	Donkey	IgG (H+L)	Cy <sup>TM</sup> 3	1:500	711-161- 52	Jackson Immuno- Research, West Grove, PA, USA
Rat IgG	Donkey	IgG (H+L)	Cy <sup>TM</sup> 2	1:250	712-225- 150	Jackson Immuno- Research, West Grove, PA, USA

Rat IgG	Donkey	IgG (H+L)	Cy <sup>TM</sup> 5	1:500	712-175-150	Jackson Immuno-Research, West Grove, PA, USA
---------	--------	-----------	--------------------	-------	-------------	--

**Tab. 7 Secondary antibodies.**

Streptavidin-conjugated fluorophores			
Fluorophore	Dilution	Catalog Number	Supplier
Alexa Fluor 488	1:500	016-540-084	Jackson Immuno-Research, West Grove, PA, USA
Alexa Fluor 594	1:500	016-580-084	Jackson Immuno-Research, West Grove, PA, USA
Alexa Fluor 647	1:500	016-600-084	Jackson Immuno-Research, West Grove, PA, USA

**Tab. 8 Streptavidin-conjugated fluorophores.**

### 3.1.6 Staining kits

Staining kit	Supplier
MaxFluor <sup>TM</sup> Mouse on Mouse Fluorescence Detection Kit (MaxFluor 488)	Dianova GmbH, Hamburg, Germany

**Tab. 9 Staining kits.**

### 3.1.7 Computer Software

Computer software	Supplier
Adobe Illustrator	Adobe Systems Inc., San Jose, CA, USA
Adobe Photoshop CS5	Adobe Systems Inc., San Jose, CA, USA
Axio Vision Rel. 4.8	Carl Zeiss Microscopy GmbH, Jena, Germany
GraphPad PRISM 6	Graph Pad Software Inc., La Jolla, CA, USA
Image J	NIH, Bethesda, MD, USA

Leica LAS X Core offline version 1.9	Leica Microsystems Vertrieb GmbH, Wetzlar, Germany
Leica Microsystems LAS AF TCS SP5	Leica Microsystems Vertrieb GmbH, Wetzlar, Germany
Microsoft Office 2011	Microsoft, Redmond, WA, USA
Thomson Reuters EndNote X7.1	Thomson Reuters, Philadelphia, PA, USA
Volocity	PerkinElmer, Waltham, MA, USA

**Tab. 10 Computer software.**

## 3.2 Methods

### 3.2.1 Animal model: NesCreER<sup>T2</sup> x Ai9tdTomato

The NesCreER<sup>T2</sup> x Ai9tdTomato mouse model is based on the Cre/loxP system, a time- and tissue-dependent recombination method with which selected DNA sequences can be deleted or recombined, respectively [162]. LoxP (locus of X over P1) sites are 34 bp DNA sequences with an 8 bp non-palindromic core region flanked by two 13bp inverted repeats. Every loxP site is specifically identified by the enzyme Cre (cyclization recombination) recombinase [163]. In order to delete or recombine a DNA sequence of interest, two loxP sites have to be placed before and after the latter; this constellation is called “floxed” sequence. Depending on the location and orientation of said loxP sites, Cre recombinase now catalyzes either deletion or translocation or inversion of the DNA sequence in between. If two loxP sites are directly repeated on the same chromosome, Cre recombinase excises the floxed sequence as a covalently closed circle with one loxP site remaining in the DNA molecule. This reaction is a chemical equilibrium, in which the excision prevails [164].

NesCreER<sup>T2</sup> mice carry the CreER transgene under the control of the Nestin promoter and enhancer located in the second intron of the Nestin gene. The Nestin gene is active in neural stem cells and other progenitor cells during CNS development. CreER, a fusion protein of Cre and the human estrogen receptor  $\alpha$ , is Tamoxifen inducible. Only if Tamoxifen is administered, CreER is activated and translocated into the nucleus where it can fulfill its function. Otherwise the protein stays in the cytoplasm where it remains functionless. Tamoxifen injection therefore determines the time point of genetic recombination in this mouse model (cf. Fig. 6) [162, 165].

In Ai9tdTomato mice, a loxP flanked stop cassette precedes the tdTomato coding region. Thus, if NesCreER<sup>T2</sup> and Ai9tdTomato mice are crossbred generating NesCreER<sup>T2</sup> x Ai9tdTomato double transgenic mice, Cre recombinase excises the floxed stop cassette after Tamoxifen administration [162]. RFP (red fluorescent protein) is now expressed by all cells that express CreER, i.e. all cells that express Nestin at the time of Tamoxifen administration.

As a result, NesCreER<sup>T2</sup> x Ai9tdTomato mice can be used as a fate-mapping tool for Nestin expressing cells with RFP as reporter molecule [166].

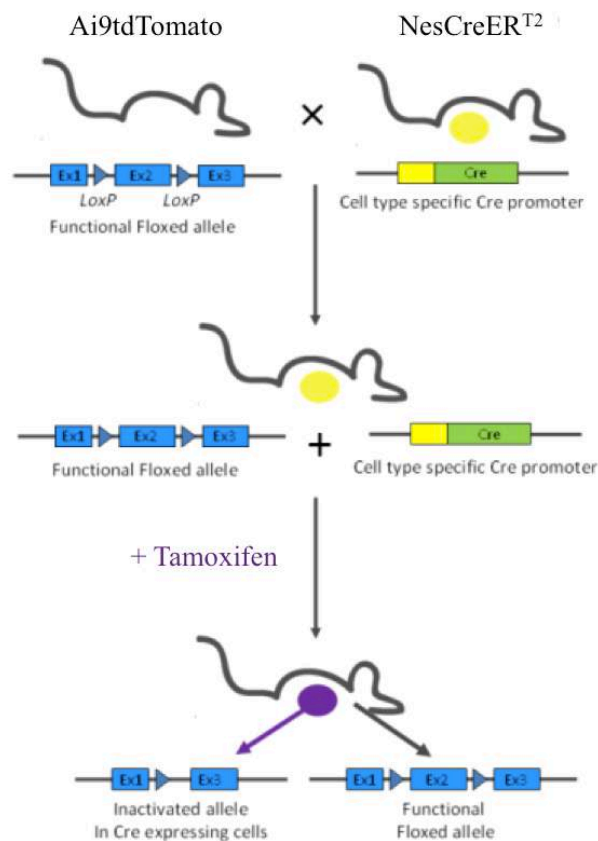


**Fig. 6 The NesCreER<sup>T2</sup> x Ai9tdTomato mouse model.** The CreER gene is placed under the control of a cell type specific Cre promoter (Nestin promoter). After Tamoxifen administration, the functional floxed allele (floxed stop cassette preceding the tdTomato coding region) is recombined by Cre recombinase. Adapted from <http://www.ics-mci.fr/mousecre> [accessed 16.08.2018, 11:30 a.m.].

### 3.2.2 Treatment protocol

All in vivo experiments were conducted in the Walter Brendel Centre for Experimental Medicine, Department of Neurosurgical Research, LMU Munich. Mice were handled in compliance with the regulations of the German law on animal welfare and were approved by the Regierung von Oberbayern in Munich, Germany. Animal cages were standardized. Water and food was available ad libitum. A circadian day and night light rhythm of 12 hours was obtained.

For this study, male and female 2-3 months old NesCreER<sup>T2</sup> x Ai9tdTomato transgenic mice were used. They were generated by cross-breeding the NesCreER<sup>T2</sup> strain (generated by Verdon Taylor, University of Basel) with the Ai9tdTomato reporter line (purchased from The Jackson Laboratory). In the experimental groups (group A and B), all mice carried both the

NesCreER<sup>T2</sup> and the Ai9tdTomato transgene. On day 1 of the treatment protocol, the tumor cells (GL261, 100.00 cells/mouse, 1  $\mu$ l) were inoculated followed by Tamoxifen administration on day 3, 4 and 5 (cf. Fig. 7). The thymidine analogue CldU (Chlorodeoxyuridine) was injected 2 days, IdU (Iododeoxyuridine) 5 hours before sacrifice (cf. Fig. 7). Mice of group A were sacrificed 14 days and mice of group B 21 days after tumor inoculation, respectively.

As controls, 3 further groups were included. They were genetically modified and treated in the same manner as the experimental groups excluding the following conditions: Mice of control 1 did not carry the NesCreER<sup>T2</sup> transgene; mice of control 2 did not receive a Tamoxifen treatment; mice of control 3 served as a positive control; mice of control 4 were not inoculated with tumor cells but stabbed with the injection needle (stab-wound control). Control mice did not receive CldU/IdU treatment.

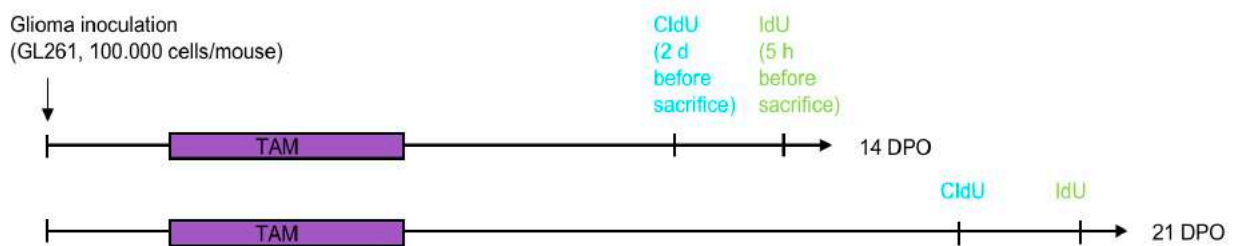


**Fig. 7 Treatment protocol.** After tumor-inoculation on day 1 (GL261, 100.000 cells/mouse), Tamoxifen (TAM) was administered i.p. on day 3, 4, and 5. CldU was injected 2 days, IdU 5 hours before perfusion of mice, respectively. Mice were sacrificed 14 or 21 days post-operative (DPO).

### 3.2.2.1 Tumor inoculation

On day 1 of the treatment protocol, 100.000 GL261 murine glioma cells (1  $\mu$ l) per mouse were inoculated. GL261 murine glioma cells reliably generate angiogenic tumors that have a consistent histopathological pattern and growth-rate in cohorts of mice [167].

The surgical procedure was conducted as follows: Mice were anesthetized with 0,36 ml 2% Rompun, 1,02 ml 10% Ketavet and 4,86 ml 0,9% NaCl depending on their individual body weight; corneas were kept moisturized with Bepanthen® Eye- and Nosecream. Then, the head was placed onto the stereotactic frame where it was carefully fixed in flat-skull position. After disinfection with 10% potassium iodide solution, the skin of the skull was cut with a scalpel blade. Through a midline incision, a burr hole was made 1,5 mm anterior and 2 mm right of the bregma by drilling with a 23-gauge needle tip. Now, a syringe was placed 5 mm deep in the tissue with which glioma cells in DMEM medium without supplements were injected. In the

end, the wound was sutured. Mice of control 4 were not inoculated with tumor cells but stabbed with a needle (stab-wound control).

### **3.2.2.2 Tamoxifen treatment**

On day 3, 4 and 5 of the treatment protocol, 75 mg Tamoxifen/kg body weight of the animal (dissolved in corn oil) was administered, respectively. The injections were performed intraperitoneally (i.p.) once every 24 hours. Mice of control 2 only received a corn oil injection.

### **3.2.2.3 CldU/IdU treatment**

CldU and IdU are thymidine analogues, which get incorporated by nascent DNA at replication forks instead of physiological bases [53]. They can later be detected as replication markers using respective antibodies for immunohistochemistry [168, 169].

Using equimolar amounts of said 2 thymidine analogues together, it is furthermore possible to distinguish between different proliferation types [170, 171]: Since CldU was administered 2 days before perfusion, cells that are traversing S-phase at this point of time incorporate the thymidine analogue into their DNA. IdU, in turn, was administered 5 hours before sacrifice and indicates the currently proliferating cells (taking-up IdU within 5 hours before termination of the experiment). Cells that are both CldU and IdU positive, traversed S-phase both 2 days and 5 hours before sacrifice; they can thus be interpreted as continuously proliferating cells. However, if cells proliferate very rapidly, they dilute-out the earlier administered and incorporated thymidine-analogue (CldU), while still being IdU positive. This interpretation of the CldU/IdU labeling paradigm was made in concordance with prior thymidine analogue uptake studies [170, 171]. Its application and relevance to the study at hand is going to be further explained in chapter 4.2 Proliferative expansion of the cells of the pericyte-lineage.

In accordance with established protocols [171], CldU was administered 2 days before perfusion at a concentration of 42,75 mg/kg body weight of the animal (dissolved in 0.9% saline). IdU was administered 5 hours before perfusion at a concentration of 56,75 mg/kg body weight of the animal (dissolved in 0.1 M phosphate buffered saline [PBS] with 2 drops of 5 M NaOH per 10-15 ml PBS). Both solutions were preheated to 37°C and injected i.p.

### **3.2.3 Perfusion and tissue preparation**

Mice were perfused with 0,9% saline to wash out the blood followed by 4% paraformaldehyde (PFA) dissolved in PBS. Perfusion was performed transcardially using a perfusion system (8,7

ml/min) so that the substances reach the brain parenchyma through the vascular system. Further external fixation steps followed.

The procedure was conducted as follows: After anesthesia as described earlier (chapter 3.2.2.1 Tumor inoculation), a thoracotomy was performed, severing the diaphragm in order to expose the heart. The right atrium was opened as a drainage for the extruded blood and first PBS followed by the PFA solution (max. 25 ml) was infused through the left ventricle using a peristaltic pump. After successful perfusion, the brain parenchyma was dissected and kept in a 4% PFA solution for 2 days at 4°C in order to post-fix the tissue (brains of 105, 106 and control 4 were kept in a 2% PFA solution for only 2 hours).

As the brain tissue was then prepared for cutting, it was placed on the object table of the microtome surrounded by dry ice for continuous cooling. 40 µm horizontal sections were made and preserved as free-floating sections in a 24-well-plate filled with cryoprotectant (Ethylenglycol, Glycerol and 0,1 M PO<sub>4</sub> buffer in a 1:1:2 solution at pH 7,4), which protects the tissue from freezing. During the cutting process, each section was placed in one well (from A1 to D6); having reached the end of the well plate, the next section was subsequently placed in A1. With this method, approximately 5 sections of different brain regions could be found in each well. The whole well plate was kept at -20°C protected from light by aluminum foil.

### **3.2.4 HE staining**

Hematoxylin Eosin staining (HE staining) implicates the application of the basic dye Hematoxylin, which colors acidic structures blue, and an alcohol-based acidic Eosin, which colors alkaline structures bright pink. This staining was conducted as follows in order to estimate the individual tumor volume of each mouse:

1. Mounting of the sections
2. Dehydration in 100% Ethanol for 30 sec
3. Staining in Meyer's Hemalaun solution for 5 min
4. Rinsing in running tap water for 5 min
5. Counter staining with 0.5% Eosin G-solution for 10 sec
6. Dipping very shortly in a. dest. (Caution: Eosin is water soluble)
7. Dehydration through ascending alcohol series starting with 70% EtOH for 20 sec
8. Continued by 96% EtOH for 1 min
9. Continued by 100% EtOH for 1 min
10. Continued by Roti®-Histol for 1 min

11. Repetition of the last step with fresh Roti®-Histol
12. Covering with mounting medium

### **3.2.5 Immunohistochemistry**

Immunohistochemistry was performed by the indirect method, either with or without biotinylated Streptavidin conjugation, using fluorescence techniques. The indirect method relies on the principle that a primary antibody detects its specific antigen; then, it is bound by a secondary, fluorophore coupled antibody, which is directed against the primary antibody's host species. The fluorophore, in turn, can be visualized by fluorescence microscopy. Since several molecules of secondary antibodies can react with one primary antibody molecule, signal amplification entails a high sensitivity of indirect immunofluorescence stains. Furthermore, if the host species of two or more different primary antibodies do not coincide, their respective secondary antibodies do not interfere with each other; such primary antibodies can therefore be co-applied in one immunostaining procedure [172].

Binding specificity of primary antibodies was ensured by checking the conducted stains for pre-established target structures of the respective primary antibody, i.e. target structures which have been reported previously to be bound by the respective primary antibody. Moreover, control sections were stained by the secondary antibody alone in order to detect improper binding of the secondary antibody.

All stains, excluding the ones conducted with the mouse-on-mouse kit, were performed as free-floating-sections, i.e. sections were stained while floating in a well plate and mounted afterwards, leading to improved antibody penetration into the tissue.

#### **3.2.5.1 Without biotinylated Streptavidin conjugation**

Immunofluorescence stains without biotinylated Streptavidin conjugation were performed as follows:

1. Washing in PBST (PBS, 0.1% Tween-20) 3 x 5 min at room temperature
2. Protein blocking (PBS, 0.3% Triton X-100, 5% serum of the secondary antibody's host species) for 1h at room temperature
3. Primary antibody (see Tab. 6 for dilutions) diluted in PBS, 0.3% Triton X-100, 5% serum of the secondary antibody's host species over night at 4 °C
4. Washing in PBST (PBS, 0.1% Tween-20) 3 x 5 min at room temperature

5. Secondary antibody (see Tab. 7 for dilutions) diluted in PBS, 0.3% Triton X-100, 5% serum of the secondary antibody's host species for 2 h at room temperature
6. Washing in PBST (PBS, 0.1% Tween-20) 3 x 5 min at room temperature
7. Alexa Hoechst 1:1000 for 1 min at room temperature as a nuclear stain
8. Mounting and covering with fluorescence mounting medium

The indirect method was used for RFP, CldU, IdU, CD31, Nestin and NG2 stains.

### **3.2.5.2 With biotinylated Streptavidin conjugation (LSAB method)**

The Labeled Streptavidin Biotin (LSAB) method is another technique for indirect immunofluorescence stains. Streptavidin, derived from streptomyces avidinii, is a large protein with four binding sites for the vitamin biotin. In fact, this is one of the strongest non-covalent bonds known in biology. In the LSAB method, the antigen is bound by a specific biotinylated antibody, which then reacts with fluorescent-dye labeled Streptavidin. Since the binding affinity is very high and one primary antibody reacts with four secondary antibodies, this method has a higher sensitivity than indirect immunofluorescent stainings without biotinylated Streptavidin conjugation [172]. LSAB immunofluorescence stainings were performed as follows:

1. Washing in PBST (PBS, 0.1% Tween-20) 3 x 5 min
2. Protein blocking (PBS, 0.3% Triton X-100, 5% serum of the secondary antibody's host species) for 1 h
3. Primary biotinylated antibody (see Tab. 6 for dilutions) diluted in PBS, 0.3% Triton X-100, 5% serum of the secondary antibody's host species over night at 4 °C
4. Washing in PBST (PBS, 0.1% Tween-20) 3 x 5 min
5. Fluorophore coupled Streptavidin (see Tab. 8 for dilutions) diluted in PBS, 0.3% Triton X-100, 5% serum of the secondary antibody's host species for 2 h at room temperature
6. Washing in PBST (PBS, 0.1% Tween-20) 3 x 5 min
7. Alexa Hoechst 1:1000 for 1 min at room temperature in order to visualize the nuclei
8. Mounting and covering with fluorescence mounting medium

Instead of a biotinylated primary antibody, a non-biotinylated primary followed by a biotinylated secondary antibody can also be used. Here, the streptavidin conjugate is then added as a third step. This leads to even higher signal amplification and sensitivity. The LSAB method was used for IB4, vWF, Desmin, PDGFR $\beta$ , Apelin and APJ stains.

### 3.2.5.3 Mouse-on-mouse kit

In some situations, if there are no other antibodies available, mouse antibodies are used to detect specific antigens on mouse tissue. This, however, can cause difficulties since the secondary antibody thus has to be directed against mouse IgGs, which are also present in the endogenous tissue during inflammatory processes, including tumor-associated inflammation. As the blood-brain-barrier is opened caused by tumor progression in glioma mouse models, the immunoglobulines can directly migrate to the tumor and are detected by the secondary antibody. In order to reduce this background staining, a Dianova MaxFluor™ Mouse on Mouse Fluorescence Detection Kit (cf. chapter 3.1.6 Staining kits) was utilized. The procedure was conducted as follows:

1. Mounting and circling the sections with a Dako pen (a lipid marker which ensures that the different solutions remain on the section)
2. Fixation on the microscope slide with 4% PFA for 10 min
3. Washing in PBST (PBS, 0.1% Tween-20) 3 x 2 min at room temperature
4. Blocking with Protein blocking solution (reagent 1) for 10 min at room temperature
5. Blocking with MaxMOM blocking reagent (reagent 2) for 1 h at room temperature
6. Primary antibody (see Tab. 6 for dilutions) diluted in PBS, 0.3% Triton X-100, 5% serum of the secondary antibody's host species over night at 4 °C
7. Washing in PBST (PBS, 0.1% Tween-20) 3 x 2 min at room temperature
8. Fluorescence signal enhancer (reagent 3) for 30 min at room temperature
9. Washing in PBST (PBS, 0.1% Tween-20) 3 x 2 min at room temperature
10. Max Fluor labeled linker (reagent 4) 1:200 and secondary antibody (see Tab. 7 for dilutions) diluted in Fluorescent Diluent (reagent 5) for 2 h at room temperature
11. Washing in PBST (PBS, 0.1% Tween-20) 3 x 2 min at room temperature
12. Rinsing shortly in distilled water
13. Alexa Hoechst 1:1000 for 1 min at room temperature as a nuclear stain
14. Covering with fluorescence mounting medium

The mouse-on-mouse kit was used for Nestin as well as for CldU, IdU and RFP triple stains.

### 3.2.5.4 CldU/IdU staining

The injected thymidine analogues CldU and IdU can be detected using a rat anti Bromodeoxyuridine (BrdU) antibody, which is also directed against CldU, and a mouse anti

BrdU antibody, which also binds IdU, respectively. Because both are nuclear stains, an antigen retrieval has to be performed so that the antibody can find its binding site, i.e. CldU/IdU implemented into DNA [171]. Therefore, HCl is added to denature DNA, followed by sodium tetraborate to neutralize the tissue. All CldU/IdU stains were performed as follows:

1. Washing in PBST (PBS, 0.1% Tween-20) 2 x 5 min at room temperature
2. Washing in H<sub>2</sub>O 2 x 5 min at room temperature
3. Denaturing in 2 M HCl for 45 min at room temperature
4. Neutralization with 0.1 M sodium tetraborate for 15 min at room temperature
5. Washing in PBST (PBS, 0.1% Tween-20) 6 x 10 min at room temperature
6. Protein blocking (PBS, 0.3% Triton X-100, 5% donkey serum) for 1h at room temperature
7. Rat anti CldU 1:250 anti IdU 1:500 diluted in PBS, 0.3% Triton X-100, 5% donkey serum over night at 4 °C
8. Washing in PBST (PBS, 0.1% Tween-20) 3 x 5 min at room temperature
9. Cy<sup>TM</sup>5 donkey anti rat/Cy<sup>TM</sup>5 donkey anti mouse 1:500 diluted in PBS, 0.3% Triton X-100, 5% donkey serum for 2 h at room temperature
10. Washing in PBST (PBS, 0.1% Tween-20) 3 x 5 min at room temperature
11. Alexa Hoechst 1:1000 for 1 min at room temperature as a nuclear stain
12. Mounting and covering with fluorescence mounting medium

Using this general protocol, either CldU or IdU stains were combined with both IB4 and RFP stains, respectively. CldU, IdU and RFP triple stains were performed using the mouse-on-mouse kit (MOM-kit, cf. Chapter 3.2.5.3 Mouse-on-mouse kit). Here, steps 1-3 of the CldU/IdU protocol were conducted as free floating sections, followed by steps 1-14 of the MOM kit.

### **3.2.5.5 Single-chain fragment variables**

Single-chain fragment variables (ScFv) are fusion proteins of the variable regions of the heavy (V<sub>H</sub>) and the light (V<sub>L</sub>) chain of an antibody, which are joined together by a flexible short linker peptide. ScFvs can be used both therapeutically (linked to e.g. a drug) [173] and for imaging purposes (linked to e.g. a fluorophore) [174]. For the thesis at hand, an anti-Apelin scFv (C12), which was coupled to a myc-tag was utilized. The latter was detected by a goat anti myc secondary antibody, which was then bound by a fluorophore-linked tertiary antibody, respectively. The stain was performed as follows:

1. Washing in PBST (PBS, 0.1% Tween-20) 3 x 5 min at room temperature
2. Protein blocking (PBS, 0.3% Triton X-100, 5% donkey serum) for 1h at room temperature
3. Anti Apelin scFv (C12) diluted in PBS, 0.3% Triton X-100, 5% donkey serum overnight at 4 °C
4. Washing in PBST (PBS, 0.1% Tween-20) 3 x 5 min at room temperature
5. Goat anti myc 1:100 diluted in PBS, 0.3% Triton X-100, 5% donkey serum for 2 h at room temperature
6. Washing in PBST (PBS, 0.1% Tween-20) 3 x 5 min at room temperature
7. Alexa 488 donkey anti goat 1:500 diluted in PBS, 0.3% Triton X-100, 5% donkey serum for 2 h at room temperature
8. Washing in PBST (PBS, 0.1% Tween-20) 3 x 5 min at room temperature
9. Alexa Hoechst 1:1000 for 1 min at room temperature as a nuclear stain
10. Mounting and covering with fluorescence mounting medium

A Single-chain fragment variable was used for Apelin stainings.

### **3.2.6 Microscopy**

For the study at hand, light-, fluorescence- as well as confocal-microscopy was conducted.

#### **3.2.6.1 Light microscopy**

Light microscopy was only applied for the evaluation of HE stains using a Zeiss Axioskop 2 light microscope and a Breukoven BMS D1-223A light microscope.

#### **3.2.6.2 Fluorescence microscopy**

For quantification analyses fluorescence microscopy was conducted. If only a red, green and DAPI filter was needed, a Zeiss Axiovert 135 TV fluorescence microscope and a Zeiss Axiovert 25 fluorescence microscope was used. If also a far red filter was needed, a Zeiss Axio Observer A1 inverse fluorescence microscope (Department of Cardiosurgical Research, LMU Munich) was used.

#### **3.2.6.3 Confocal microscopy**

Unlike conventional widefield microscopes, confocal microscopes are able to control depth of field, elimination, and reduction of background information. Also, optical sections from thick

specimens can be collected. This leads to high-resolution imaging, as image series can be viewed both as a maximal projection of all plains and as a single plain at a chosen z-position. Additionally, a crosshair mode can visualize the xy-plane of one image while simultaneously showing the xz- and yz-plane so that accurate co-localization analyses can be conducted (cf. Fig. 8).

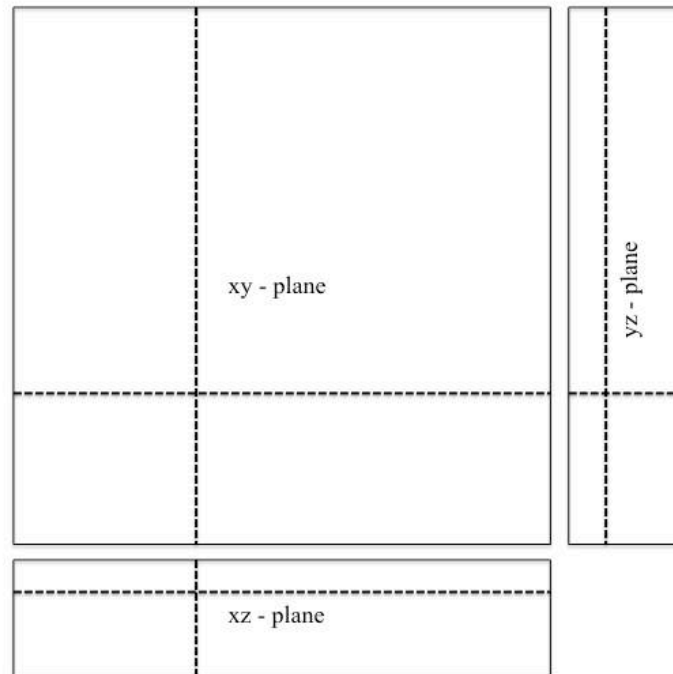


**Fig. 8 Schematic illustration of the crosshair mode.** Images taken by confocal microscopy and visualized in the crosshair mode analogously show the xy-, xz-, and yz-plane, facilitating the analysis of immunohistochemistry stainings, especially regarding co-localization of two or more markers.

In this study, confocal microscopy was performed using a Leica broadband confocal laser microscope TCS SP5 (Walter-Brendel Centre for Experimental Medicine, LMU Munich). The following settings were applied for all images.

Magnification: 20x (40x only for RFP, CldU and IdU triple stains)

Zoom factor: 2

Format: 1024 x 1024 pixels

Z-stack step width: 0,5  $\mu\text{m}$

### 3.2.7 3D reconstruction

After confocal imaging the Leica Image File Format (lif) documents were taken for 3D reconstruction using Volocity computer software (cf. chapter 3.1.7 Computer software). The

program was used for illustrating morphology and spatial relations between individual cells, but not for co-localization analyses. For every 3D reconstruction shown in this dissertation the isosurface mode was applied.

### 3.2.8 Evaluation criteria

Regarding immunohistochemical stains, the extent of co-localization of the traced cells (i.e. the RFP positive cells) with a variety of markers was evaluated according to the following criteria: As the reporter molecule, RFP, is expressed within the cytoplasm, cells were interpreted to co-localize with markers that are expressed in the same cell compartment (Desmin, Iba1) if pixels identified in the red channel co-localize with pixels in the green or blue channel. If the marker of interest, however, is expressed in other compartments, e.g. in the nucleus (CldU, IdU) or on the cell surface (NG2, PDGFR $\beta$ ), cells were interpreted to co-localize if a RFP positive cell inherited a stained nucleus or was surrounded by a stained plasmalemma, respectively. Concerning the analysis of CldU/IdU stains, only if CldU/IdU positive structures also co-localized with an Alexa Hoechst positive nucleus they were included in the respective quantification. Cells were interpreted as perivascular if they were located at a distance of maximally 1  $\mu\text{m}$  to an IB4- or vWF-labeled vascular structure.

For all quantifications a 20x magnification was utilized. Unclearly marked cells were additionally observed at a 100x magnification. Quantifications were conducted from 4 randomly selected optical fields of both tumor and peritumoral (optical field at the edge of the tumor) and tumor free (optical field of a corresponding region in the contralateral, tumor-free hemisphere) regions per section. As 3 sections from corresponding brain regions were taken per animal, a total of 36 optical fields per animal were evaluated for every immunohistochemical stain. All quantifications were performed from a picture of the respective optical field. The counting was performed by hand with the support of ImageJ software.

Confocal image analyses were performed using the maximal projection and crosshair mode of Leica LAS AF imaging software (for settings cf. chapter 3.2.6.3 Confocal microscopy). Only if pixels colocalized in the xy-, xz- and yz- plane, cells were regarded as double-/triple-positive.

### 3.2.9 CldU/IdU labeling indices

CldU/IdU labeling indices are a measure for cell proliferation indicating the percentage of proliferating cells. They were calculated as follows:

$$\text{CldU labeling index} = \frac{\text{CldU labeled cells}}{\text{Alexa Hoechst labeled cells}} \times 100$$

$$\text{IdU labeling index} = \frac{\text{IdU labeled cells}}{\text{Alexa Hoechst labeled cells}} \times 100$$

$$\text{CldU vascular labeling index} = \frac{\text{CldU} + \text{IB4 labeled endothelial cells}}{\text{IB4 labeled endothelial cells}} \times 100$$

$$\text{IdU vascular labeling index} = \frac{\text{IdU} + \text{IB4 labeled endothelial cells}}{\text{IB4 labeled endothelial cells}} \times 100$$

$$\text{CldU microglia \& macrophages labeling index} = \frac{\text{CldU} + \text{IB4 labeled microglia \& macrophages}}{\text{IB4 labeled microglia \& macrophages}} \times 100$$

$$\text{IdU microglia \& macrophages labeling index} = \frac{\text{IdU} + \text{IB4 labeled microglia \& macrophages}}{\text{IB4 labeled microglia \& macrophages}} \times 100$$

The CldU vascular labeling index, IdU vascular labeling index, CldU microglia & macrophages labeling index and IdU microglia & macrophages labeling index was calculated by using quantifications obtained from IB4 and CldU or IB4 and IdU co-stains, respectively. Since IB4 is a widely deployed marker for both endothelial cells and microglia as well as macrophages [175], cell types were differentiated by individual morphology (large spherical-ellipsoid somata with branched processes as well as round nuclei of microglia and macrophages versus narrow, elongated cell bodies with flat nuclei of endothelial cells). Microglia and macrophages are both myeloid cells and cannot be differentiated neither by shape nor by antigen expression; in accordance with prior publications [176], they were thus integrated into one quantification.

### 3.2.10 Statistical analysis

Statistical analysis was performed using GraphPad PRISM 5 software. To compare quantification results of group A and B, an unpaired t-test was conducted; for comparing the quantification results of the tumor area, the peritumoral area and the contralateral side, the one-way ANOVA was applied. Statistical significance is assumed if  $p \leq 0,05$ .

## 4. Results

### 4.1 Delineation of the cells of the pericyte-lineage

In the study at hand, NesCreER<sup>T2</sup> x Ai9tdTomato double transgenic mice were orthotopically inoculated with GL261 murine glioma cells in order to trace Nestin expressing cells (Nestin positive at the time of Tamoxifen administration) with RFP as reporter throughout glioma progression in vivo (cf. chapter 3.2.1 Animal model: NesCreER<sup>T2</sup> x Ai9tdTomato and chapter 3.2.2 Treatment protocol). RFP positive cells therefore represent the traced cells in the following.

For a primary analysis of the NesCreER<sup>T2</sup> x Ai9tdTomato recombination system, the amount of RFP positive cells was quantified on brain sections (14 and 21 DPO) stained by immunofluorescence (cf. Fig. 9). The endogenous RFP signal was enhanced by application of an anti-RFP antibody (cf. chapter 3.1.5 antibodies and streptavidin-conjugated fluorophores), which is a common method for signal amplification.

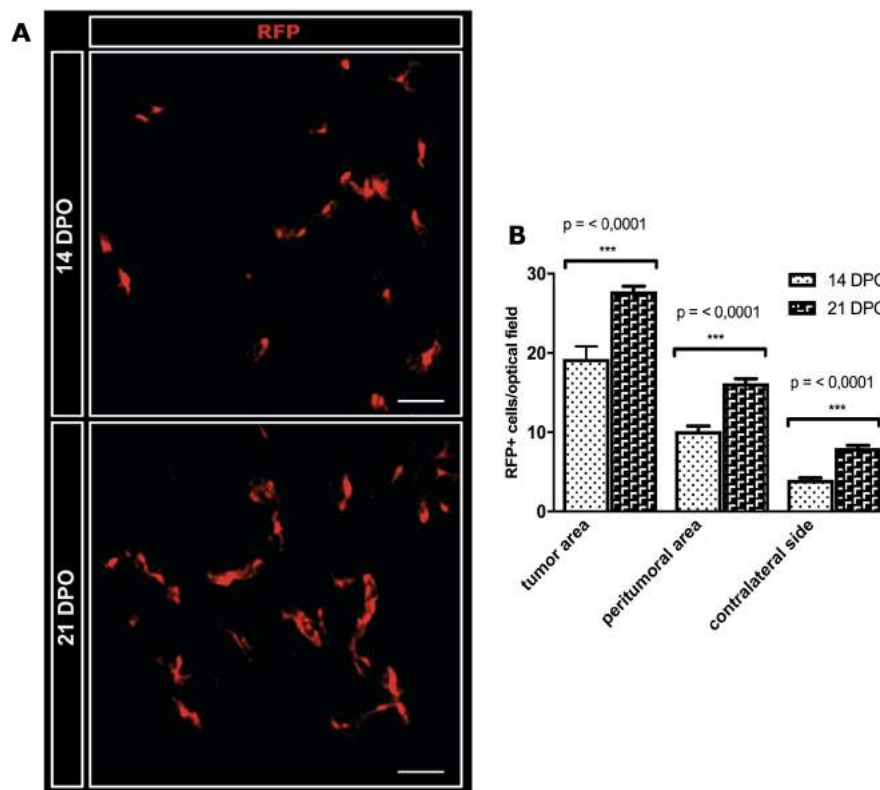


**Fig. 9 RFP positive cells in the NesCreER<sup>T2</sup> x Ai9tdTomato model.** RFP positive cells were inspected and quantified on RFP-stained brain sections 14 and 21 DPO (n = 4 mice per time point). **A** Immunofluorescence-stained brain sections illustrate a numerical increase of RFP positive cells in the tumor area and a change in RFP positive cell morphology over time. **B** Quantification results demonstrate that the amount of RFP positive cells increases significantly from 14 to 21 DPO ( $p < 0,0001$  for all areas), especially in the tumor but also in the peritumoral and contralateral area. Scale bars are 100  $\mu$ m in A. Statistical significance between individual time-points is indicated in B.

Quantifications were conducted according to the criteria explained in chapter 3.2.8 Evaluation criteria. Especially in the tumor area, but also in the peritumoral area and contralateral, i.e. tumor-free, side a significant increase of RFP positive cells was observed from 14 to 21 days of tumor growth (cf. Fig. 9 C,  $p < 0,0001$  for all areas). Regardless of the length of tumor growth, the total number of RFP positive cells was the highest in the tumor area, followed by the peritumoral area and contralateral side (cf. Fig. 9). Hence, the traced cells are primarily located in the tumor. Furthermore, the longer the time period of tumor growth is, the more traced cells can be found in all areas, especially in glioma tissue.

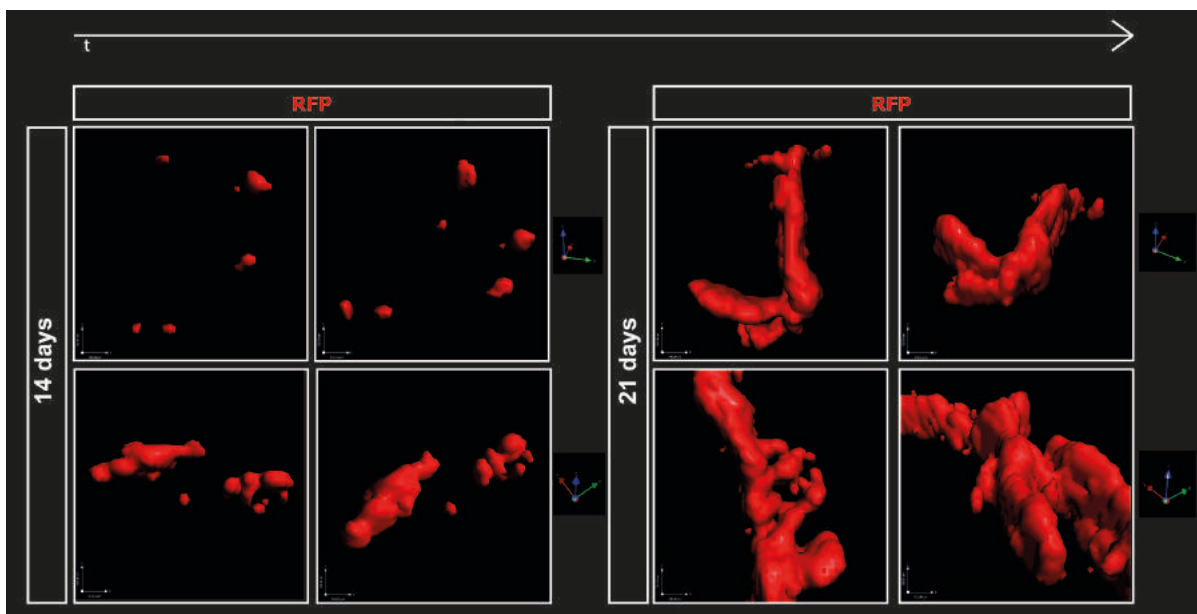


**Fig. 10 Morphological development of RFP positive cells.** 3D reconstructions of confocal micrographs of RFP stained brain sections reveal a change in morphology from small, disseminated cells 14 DPO to large conglomerates of several RFP positive cells displaying an elongated structure 21 DPO. This change in morphology exclusively takes place in glioma tissue. The images on the left column of the two boxes were taken as xy-planes; the images on the right column of the two boxes were taken from a different angle as indicated by the arrows next to them, respectively.

Not only the quantified amount but also the morphology of RFP positive cells changed over time (cf. Fig. 9 A, Fig. 10). After 14 DPO, the traced cells are small and heterogenous in shape, after 21 DPO, their morphology becomes more consistent and they increase in size. These findings were confirmed by 3D reconstructions of confocal images of RFP stained tumor sections (cf. Fig. 10). Fig. 10 clearly illustrates a development from early, small, disseminated cells to later on large conglomerates of several RFP positive cells displaying an elongated structure. Quite remarkably, this morphological change was exclusively observed in glioma tissue. In the peritumoral area and contralateral hemisphere, RFP positive cells remained small-

sized, heterogenous in morphology and scattered, both 14 and 21 DPO. Said morphological findings indicate a development of the traced cells which is different in glioma tissue compared to the peritumoral area and contralateral hemisphere.

#### **4.2 Proliferative expansion of the cells of the pericyte-lineage**

For assessment of individual cell proliferation, the thymidine analogues CldU and IdU were injected 2 days and 5 hours before perfusion, respectively (cf. chapter 3.2.2.3 CldU/IdU treatment). As such, CldU single positive cells traversed S-phase 2 days prior to sacrifice, while IdU single positive cells represent the currently proliferating cells (taking-up IdU within 5 hours before sacrifice). CldU/IdU co-labeled cells were in the cell cycle both 2 days and 5 hours before termination of the experiment; they can thus be interpreted as continuously proliferating cells. Quantifications were obtained from immunofluorescence-stained brain sections.

##### **4.2.1 CldU/IdU labeling**

Generally, significantly more CldU single positive, IdU single positive, and CldU/IdU double positive cells were found in the tumor than in the peritumoral or contralateral area (cf. Fig. 11 A, B, C,  $p < 0,0001$  for both markers), respectively. Especially in the latter, the thymidine analogues could not be detected in almost any cell. In the peritumoral region, however, a significant increase of both CldU (cf. Fig. 11 A,  $p < 0,0023$ ) and IdU (cf. Fig. 11 B,  $p < 0,0001$ ) single positive cells over time was found, indicating a general increase of proliferation both 2 days and 5 hours before sacrifice there. In the tumor area, a significant but relatively small decrease of CldU positive cells was found (cf. Fig. 11 A,  $p < 0,0136$ ). Nevertheless, the by far most extensive proliferation non-surprisingly takes place in the tumor (cf. Fig. 11 A, B, C).

Concerning CldU and IdU double stains, a meaningful increase of CldU and IdU double labeled cells was detected in the tumor (cf. Fig. 11 C,  $p < 0,0001$ ), whereas in the peritumoral and contralateral area no significant difference was observed between 14 and 21 DPO (cf. Fig. 11 C). Hence, in the tumor, the amount of continuously proliferating cells was not only the highest, but it also increases from 14 to 21 DPO.

With these quantifications at hand, respective labeling indices (cf. Tab. 11) were calculated as described in chapter 3.2.9 CldU/IdU labeling indices. 37,3% of all cells in the tumor (quantified on Alexa Hoechst-stained brain sections) incorporated CldU after 14 DPO, 28,9% after 21 DPO, respectively. The percentage of IdU labeled cells slightly decreases from 17,6% to 15,7% over time. The inoculated glioma cells thus proliferate decidedly at both time points.

Also, the increase of the CldU and IdU double labeling index from 14 to 21 days of tumor progression in the tumor as well as peritumoral area is standing out (cf. Tab. 11). The percentages of these double positive cells are indeed small, but increase from 4,4% to 6,0% over time illustrating an increment of continuously dividing cells. Since CldU and IdU labeled cells were extremely rarely found in the contralateral hemisphere as described in this chapter, (cf. Fig. 11 A, B, C), the corresponding labeling indices resulted to be very small. Due to their irrelevance to the objectives of this dissertation, they are not included in Tab. 11.

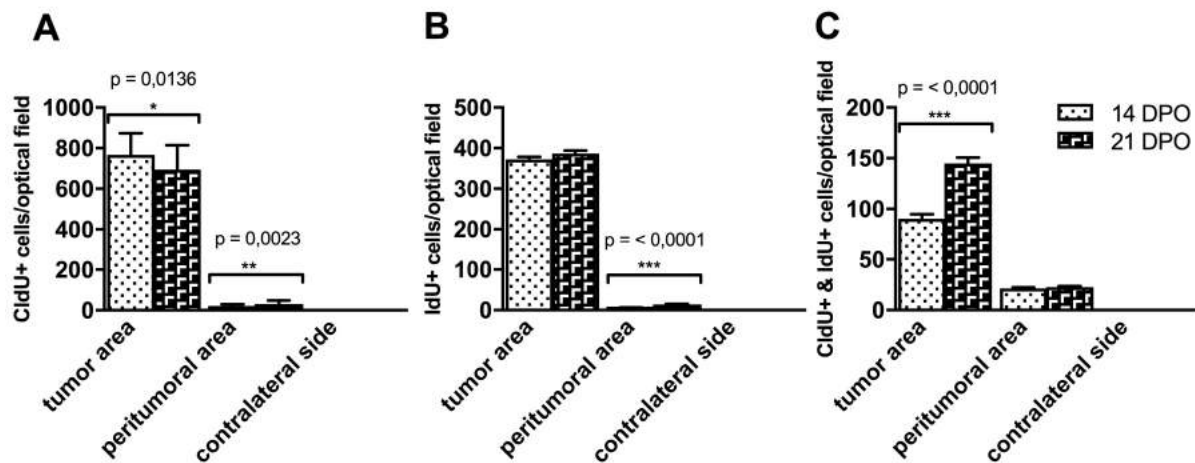


**Fig. 11 General CldU/IdU labeling.** Quantifications of thymidine analogue labeling in the tumor, peritumoral, and contralateral area were obtained from CldU-, IdU-, and Alexa Hoechst-co-stained brain sections 14 and 21 DPO (n = 4 mice per time point). **A** CldU single positive cells decrease significantly in the tumor area from 14 to 21 DPO (p < 0,0136). **B** IdU labeling remains consistently high in the tumor area. **C** The amount of CldU and IdU double positive cells very significantly increases from 14 to 21 DPO (p < 0,0001). Statistical significance between individual time-points is indicated in A, B, C.

#### 4.2.2 CldU/IdU labeling of endothelial cells and microglia/macrophages

Additional quantifications of RFP, CldU and IB4 as well as of RFP, IdU and IB4 co-stained sections were conducted in order to investigate the proliferative behavior of different cell types, namely of microglia and macrophages as well as of endothelial cells (cf. Fig. 12). The latter were identified by their individual morphology since IB4 labels both microglia, macrophages, and endothelial cells (large spherical-ellipsoid somata with branched processes as well as round nuclei of microglia and macrophages versus narrow, elongated cell bodies with flat nuclei of endothelial cells). Microglia and macrophages are both myeloid cells and cannot be differentiated neither by shape nor by antigen expression; in accordance with prior publications [176], they were thus integrated into one quantification.

Index type	Marker(s)	Labeling indices (%)			
		Tumor area		Peritumoral area	
		14 DPO	21 DPO	14 DPO	21 DPO
<b>General</b>	CldU	37,3	28,9	1,3	2,6
	IdU	17,6	15,7	1,9	1,2
	CldU & IdU	4,4	6,0	1,4	1,9
<b>Vascular</b>	CldU	18,2	18,5	9,2	15,2
	IdU	9,4	12,1	7,5	9,9
<b>Microglia/ macrophages</b>	CldU	7,1	7,5	0,6	0,5
	IdU	14,4	16,1	0,4	1,8

**Tab. 11 CldU/IdU labeling indices.** Quantifications were conducted on CldU-, IdU-, and Alexa Hoechst-stained brain sections (general labeling indices), on CldU- and IB4- as well as on IdU- and IB4-stained brain sections (vascular and microglia/macrophages labeling indices, n = 4 mice per time point). The amount of CldU/IdU positive cells (cf. Fig. 10) was normalized to the total amount of cells marked by an Alexa Hoechst stain. For calculating the vascular or microglia/macrophages labeling indices, the amount of CldU/IdU positive endothelial cells or microglia/macrophages was normalized to the total amount thereof, respectively (cf. chapter 3.2.9 CldU/IdU labeling indices).

Concerning the population of microglia and macrophages, again the highest amount of CldU and IdU labeled cells was found in the tumor ( $p < 0,0001$  for both markers) compared to the peritumoral and contralateral area (cf. Fig. 12 A, B). For CldU positive microglia and macrophages, no statistically significant change of labeled cell amounts over time was observed (cf. Fig. 12 A). Regarding IdU positive microglia and macrophages, a significant increase of labeled cells in the tumor from 14 to 21 DPO was detected ( $p < 0,0001$ ), showing an increment of proliferation at the time point of IdU injection over time (Fig. 12 B). In comparison to the total amount of IdU labeled cells (cf. Fig. 11 B), IdU positive microglia and macrophages additionally depict a significant proportion of all IdU positive cells, especially after 21 DPO. Also, the increase of IdU labeled microglia and macrophages in the tumor (cf. Fig. 12 B) is significant, whereas the total increase of IdU positive cells in the tumor from 14 to 21 DPO is not (cf. Fig. 11 B). Hence, microglia and macrophage proliferation contributes largely to tumor cell proliferation, especially in advanced tumor stages.

Regarding the population of endothelial cells, again the largest amount of both CldU and IdU labeled cells was found in the tumor area ( $p < 0,0001$  for both markers) compared to the peritumoral and contralateral region (cf. Fig. 12 B, C). Just as IdU positive microglia and macrophages, also IdU positive endothelial cells increase significantly in number from 14 to 21 DPO in the tumor ( $p < 0,0001$ , cf. Fig. 12 D). Furthermore, also an increment of CldU ( $p < 0,0001$ ) as well as IdU ( $p < 0,0026$ ) labeled endothelial cells in the peritumoral tissue was

quantified, indicating potential vessel growth in tumor surrounding areas (cf. Fig. 12 C, D). However, the total amount of CldU and IdU labeled endothelial cells is notably smaller than the number of accordingly labeled microglia and macrophages (cf. Fig. 12 A, B, C, D). They thus contribute relatively less to total tumor cell proliferation (cf. Fig. 11 A, B), albeit showing more in total and over time more increasing proliferation in the peritumoral area than microglia and macrophages. These findings confirm GL261 glioma cells as strong angiogenic stimulus.

In the tumor, more microglia and macrophages were either CldU or IdU positive than endothelial cells in absolute numbers (cf. Fig. 12 A, B, C, D). However, labeling indices of both CldU and IdU in the tumor area revealed a comparably high relative internalization of thymidine analogues by both endothelial cells and microglia/macrophages (cf. Tab 11). Comparable relative amounts of both cell populations thus proliferate quite profoundly in the glioma tissue both 14 and 21 DPO.

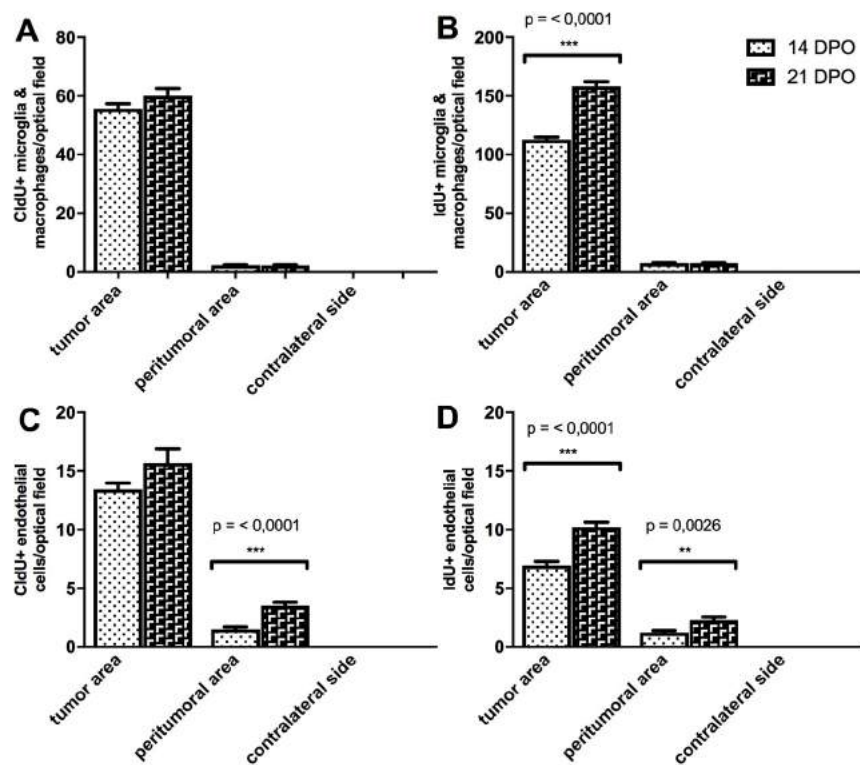


**Fig. 12 CldU/IdU-labeled cell populations.** Quantifications of CldU-/IdU-co-labeled microglia, macrophages, and endothelial cells were obtained from IB4- and CldU/IdU-co-stained brain sections ( $n = 4$  mice per time point). **A** CldU labeled microglia and macrophages. **B** IdU labeled microglia and macrophages with a significant increase of labeled cells in the tumor area from 14 to 21 DPO. **C** CldU labeled endothelial cells showing a significant increase in the peritumoral area over time. **D** IdU labeled endothelial cells increase significantly from 14 to 21 DPO in both the tumor and the peritumoral area. Statistical significance between individual time-points is indicated in A, B, C, D.

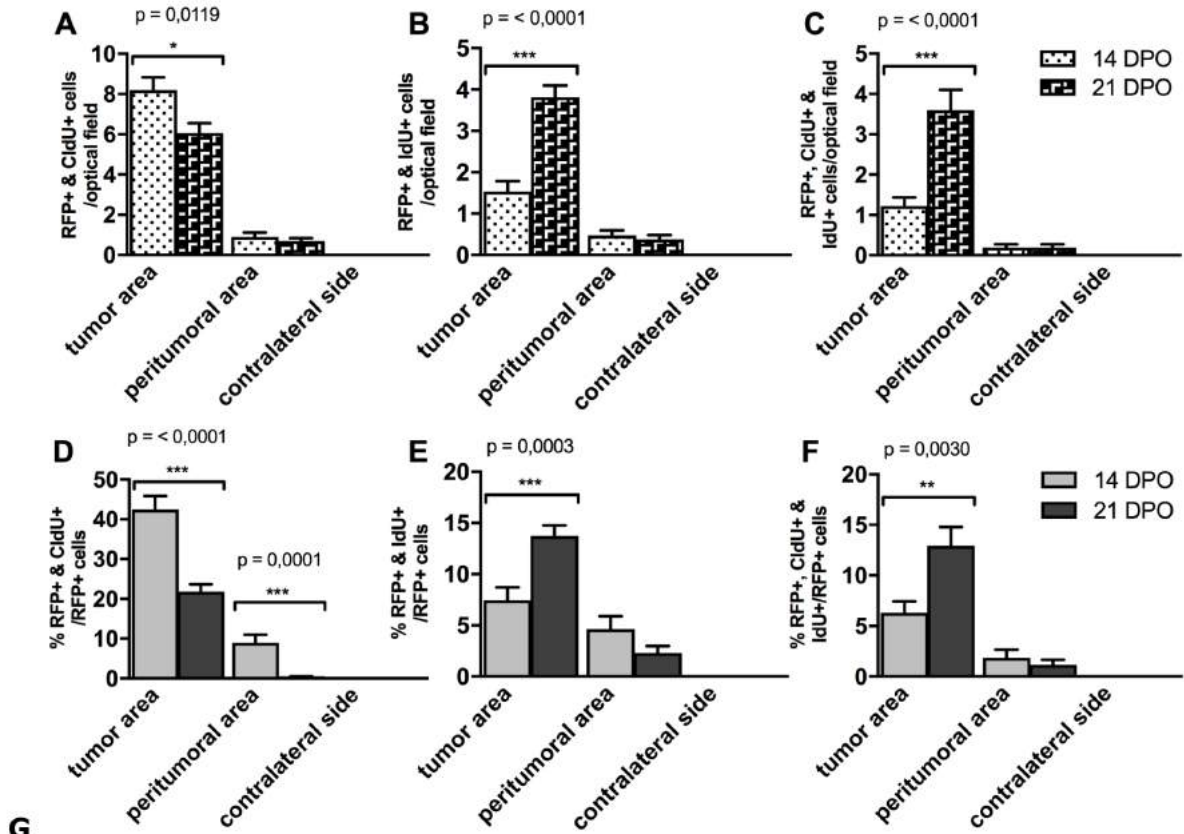
### 4.2.3 CldU/IdU labeling of the cells of the pericyte-lineage

Based on RFP and CldU or IdU co-stains, the proliferative behavior of RFP positive cells was investigated.

Just as in the total cell (cf. Fig. 11), endothelial cell (cf. Fig. 12 C, D), microglia and macrophage population (cf. Fig. 12 A, B), CldU and IdU labeled RFP positive cells were mainly detected in the tumor compared to other areas ( $p < 0,0001$  for both markers) indicating that the traced cells mainly proliferate here, both 14 and 21 DPO (cf. Fig. 13 A, B, C). The absolute increment of RFP, CldU and IdU triple positive cells from 14 to 21 DPO in the tumor area furthermore indicates that the traced cells are increasingly continuously proliferating in the neoplastic tissue the longer the time of tumor growth is (cf. Fig. 13 C). Compared to the general CldU- and IdU-double labeling indices (cf. Tab. 11), 12, 9% of all RFP positive cells stay in the cell cycle at 21 DPO (and 6,3% at 14 DPO), while only 6,0% of all tumor cells do so at that time point (and 4,4% 7 days earlier). The traced cells are thus characterized by continuous proliferation which is more prominent here than in other cells in the tumor.

In samples obtained from 21 DPO, a mean of  $3,813 \pm 0,2855$  ( $N=32$ ) RFP labeled cells were IdU positive (cf. Fig. 13 B). In relation to the mean of the RFP, CldU and IdU triple positive cells at the same time point ( $3,594 \pm 0,5097$ ,  $N=32$ , cf. Fig. 13 C), this shows that almost all traced cells proliferating at 21 DPO (94,3%) were in the cell cycle 2 days before. Also, a high but relatively smaller proportion of cells proliferating at 14 DPO (79,6%) was in the cell cycle 2 days earlier (cf. Fig. 13 B, C). This, again, demonstrates that the traced cells proliferate continuously, especially in more progressed tumor stages.

Quite remarkably, the total amount of RFP and CldU labeled cells decreases ( $p < 0,0119$ ) while the absolute number of RFP and IdU positive cells increases significantly from 14 to 21 DPO ( $p < 0,0001$ , cf. Fig. 13 A, B). Analogously, the relative amount of RFP and CldU double positive cells among all RFP positive cells decreased from 14 to 21 DPO, whereas the relative amount of RFP and IdU double positive cells showed an increment (cf. Fig. 13 D, E). This is explained by fast proliferating cells out-diluting the earlier administered thymidine analogue (CldU). They internalize CldU when it is administered (2 days before termination of the experiment), but due to additional cell cycles the marker is not detectable anymore at the time of the immunostaining. Then, at the day of sacrifice and IdU administration, fast proliferating cells incorporate IdU. In agreement with prior thymidine analogue uptake studies [170, 171], IdU single positive cells therefore represent the fast proliferating cell fraction. Strikingly, the increment of IdU and RFP double positive cells therefore indicates an increase of fast proliferating cells among the traced cell population.



**G**

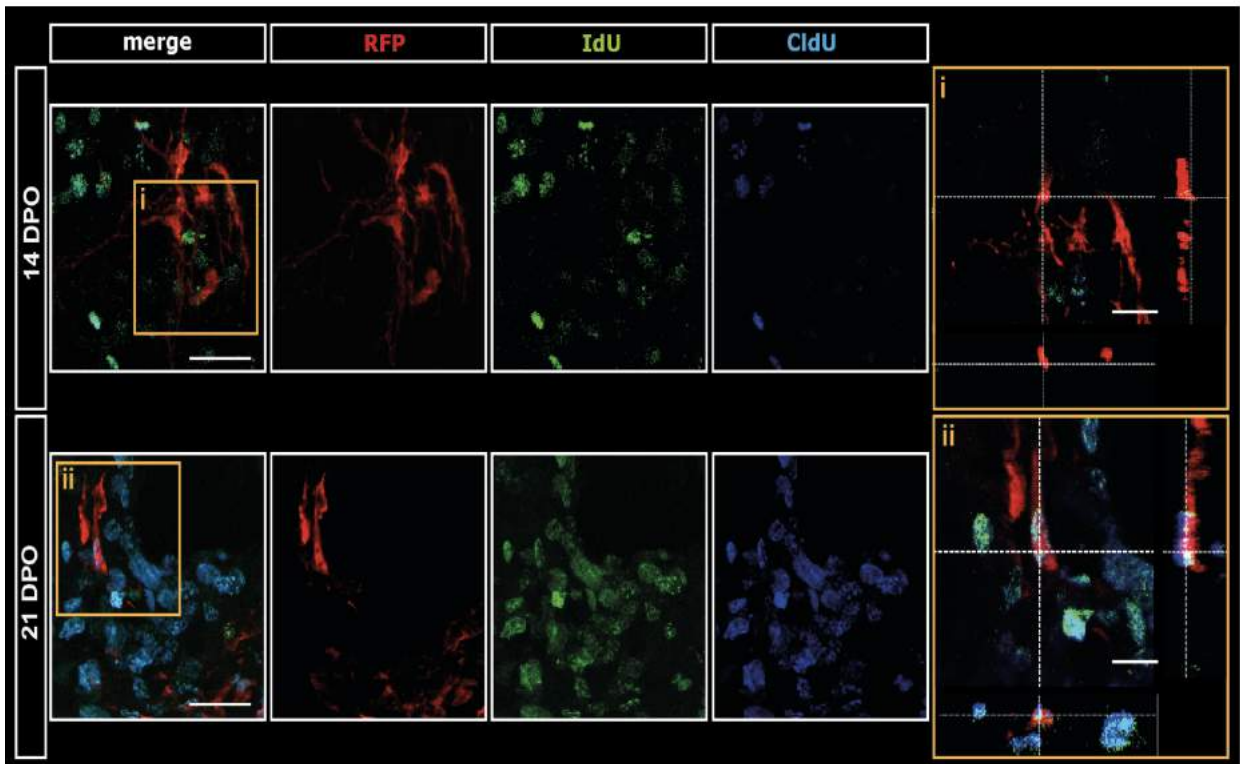


**Fig. 13 CldU/IdU labeling of RFP positive cells.** Quantifications of CldU-/IdU- and RFP double as well as of CldU, IdU, and RFP triple positive cells were obtained from CldU-, IdU- and RFP-stained brain sections 14 and 21 DPO ( $n = 4$  mice per time point). **A** Absolute amounts of CldU-labeled RFP positive cells in the tumor decrease from 14 to 21 DPO. **B** IdU-labeled traced cells in the glioma tissue, however, increase in number over time, which indicates an

increment of fast proliferating cells among the traced cell population. **C** Similarly, the amount of CldU and IdU co-labeled RFP positive cells increases significantly over time, suggesting that the traced cells are continuously proliferating in the glioma tissue, especially at more progressed tumor stages. **D, E** Amounts of CldU-/IdU- and RFP positive cells were normalized to the amount of all RFP positive cells in the respective area, demonstrating a relative decrease of CldU- and an increase of IdU-labeled RFP positive cells over time. **F** Analogously, CldU-, IdU- and RFP- triple positive cells were normalized to the amount of all RFP positive cells. This graph shows that 6,3% of the traced cells at 14 DPO and 12,9% at 21 DPO proliferate continuously, which is a very big fraction compared to general labeling indices (cf. Tab. 11). **G** Exemplary images of CldU- and IdU-co-stained brain sections showing a RFP positive cell at 14 DPO, which has not inherited a thymidine analogue. At 21 DPO, indeed, a striking amount of RFP positive cells is CldU- and IdU-co-labeled, as the images underneath exemplify. Yellow squares (i, ii) indicate the original locations of the magnification shown on the right. All images were obtained by confocal microscopy and the magnifications (i, ii) are displayed in the crosshair mode (cf. chapter 3.2.6.3 Confocal microscopy). i shows a clearly RFP single positive cell, while ii confirms that the cell located in the center of the crosshair is triple positive (red, green, and blue merge to white). Scale bars are 20  $\mu\text{m}$  in G, but 5  $\mu\text{m}$  in i, ii. Statistical significance between individual time-points is indicated in A-F.

It was further investigated to what extent the pool of traced cells is made up from vessel-associated or non-perivascular cells. This and their respective proliferative behavior was assessed by analyzing CldU, IdU, and IB4 triple stains. RFP positive cells in a juxtaendothelial (perivascular) position (and being CldU or IdU co-labeled) were quantified. A RFP positive cell was regarded as perivascular if it was measured to be maximally 1  $\mu\text{m}$  apart from a vessel (cf. chapter 3.2.8 Evaluation criteria).

RFP positive, perivascular cells were mainly found in the tumor (cf. Fig. 14 A, B, C). After 14 days of tumor growth,  $12.84 \pm 1.443$  (N=32) cells were located next to a vascular structure, after 21 days even  $24.25 \pm 1.333$  (N=32, cf. Fig. 14 A). As percentages, at earlier progression stages 66,6% of all RFP positive cells are located perivascular, whereas later 87,3% of all RFP labeled cells can be found next to a blood vessel (cf. Fig. 14 C).

These findings were confirmed by quantifications of the RFP positive, perivascular cells with vWF instead of IB4 as a blood vessel marker (Fig. 14 B). In both cases, almost equal amounts of RFP positive cells were identified to be in a perivascular position and a significant increase of perivascular located, traced cells in the tumor area from 14 to 21 days was detected ( $p < 0,0001$  for both markers, cf. Fig. 14 A, B). The main proportion, after 21 days almost 90%, of all traced cells are thus located in close apposition to endothelial cells raising the question which particular perivascular cell type they belong to.

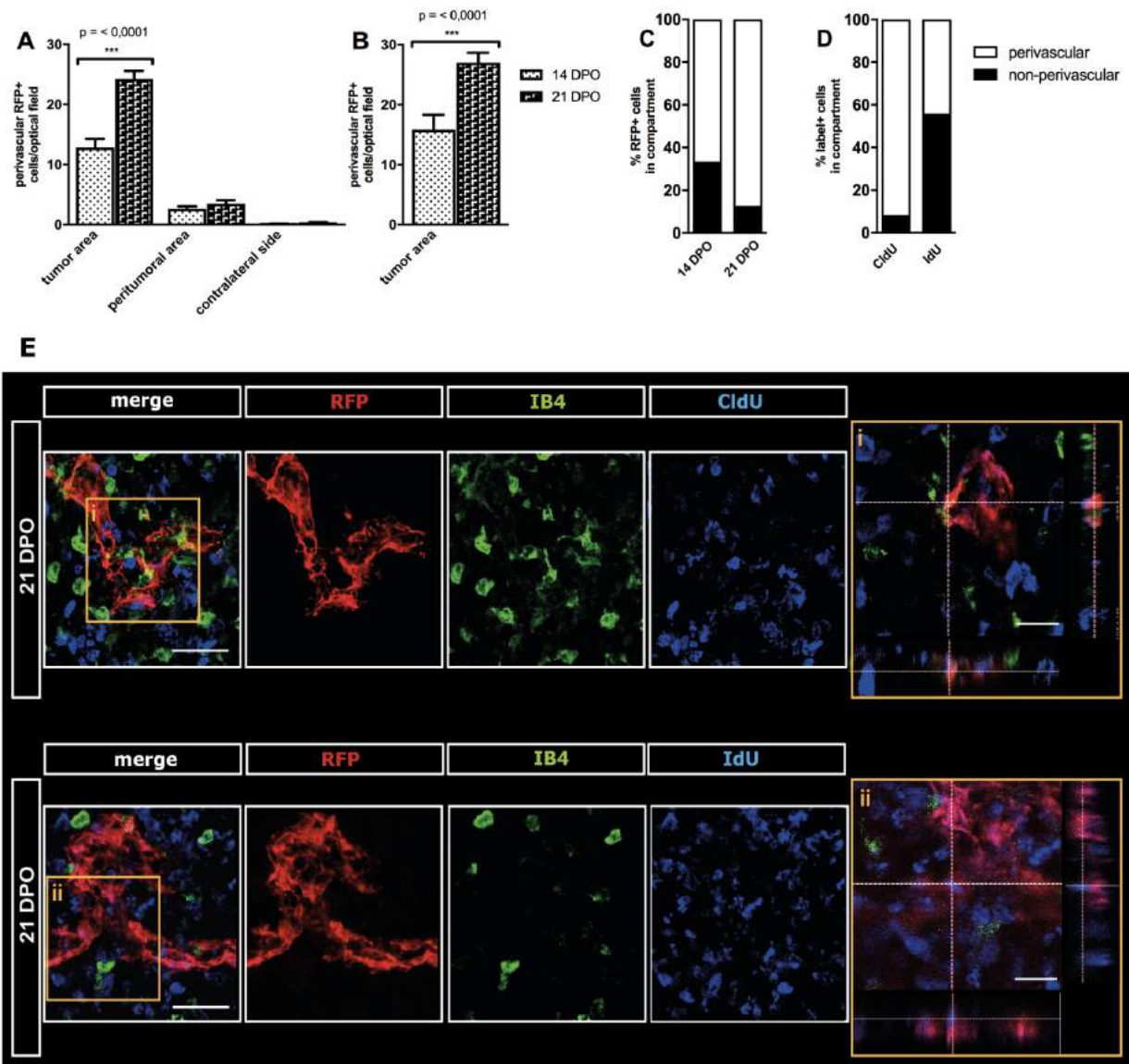


**Fig. 14 CldU/IdU labeling of perivascular RFP positive cells.** Quantifications of RFP positive cells were obtained from IB4- and CldU-/IdU-co-stained brain sections ( $n = 4$  mice per time point). **A** Amounts of RFP positive cells in a perivascular location were almost only found in the tumor and significantly increase from 14 to 21 DPO. **B** The latter was confirmed by sections stained with vWF instead of IB4 as marker for vasculature. **C** In relative numbers, 66,6% of all RFP positive cells are located perivascular at 14 DPO and at 21 DPO even 87,3% do so. **D** At 21 DPO, CldU-labeled, RFP positive cells were almost exclusively (91,6%) in a juxtaendothelial position, whereas IdU labeling was found to comparable amounts in both perivascular and non-perivascular RFP positive cells, indicating that albeit all traced cells proliferate, non-perivascular traced cells do so more rapidly. **E** Exemplary images illustrate these findings. Yellow squares (i, ii) indicate the original locations of the magnification shown on the right. All images were obtained by confocal microscopy and the magnifications (i, ii) are displayed in the crosshair mode (cf. chapter 3.2.6.3 Confocal microscopy). Images of CldU- and IB4-co-stained brain sections (tumor area) of mice sacrificed at 21 DPO (upper half of E) show multiple RFP positive cells assembled into conglomerates and located next to IB4 positive vascular structures. i furthermore shows co-localization of a RFP positive cell with a CldU-stained nucleus. CldU positivity was largely restricted to perivascular traced cells. The lower half of E moreover shows, again, a conglomerate RFP positive cells, which however is not located next to an IB4-stained vessel, but co-localizes with IdU (ii). IdU expression was found

in both perivascular and non-perivascular traced cells. The non-vascular structures marked by the IB4 stain are microglia and macrophages. Due to fundamentally different shape of said myeloid cells compared to a vascular morphology, they could easily be differentiated in quantifications. Scale bars are 20  $\mu\text{m}$  in E, but 5  $\mu\text{m}$  in i, ii. Statistical significance between individual time-points is indicated in A, B.

Concerning the incorporation of thymidine analogues of RFP positive, perivascular cells, quantifications display a proportional decrease in accordance with the general decrease of CldU labeled, RFP positive cells (Fig. 13 A). This as well applies to the increase of IdU labeled, RFP positive, perivascular cells in agreement with the general increase of IdU labeled, RFP positive cells (Fig. 13 B). Astonishingly, just as all traced cells, traced perivascular cells are therefore increasingly fast proliferating over time.

Relative amounts of thymidine analogue labeled, RFP positive cells were additionally assessed in terms of their location in the perivascular or non-perivascular compartment at 21 DPO. IdU labeling was found to almost equal relative amounts in both perivascular (44,1%) and non-perivascular (55,9%) RFP positive cells. Label-retaining of CldU was, however, almost only observed in perivascular RFP positive cells (91.6%, cf. Fig. 14 D). This data indicates that proliferation takes place in both perivascular and non-perivascular traced cells, but remarkably, compared to the perivascular traced cells, non-perivascular traced cells cycle more rapidly.

### **4.3 Characterization of the cells of the pericyte-lineage**

The traced cell population was further explored with regards to their perivascular location and marker constellation, specifically in terms of expression of pericyte and myeloid markers as well as of Apelin/APJ.

#### **4.3.1 Perivascular location**

As Quantifications have shown (cf. Fig. 14 A, B, C), the traced cells are largely found in a juxtaendothelial position the further the tumor has progressed and this development is restricted to the traced cells located in the tumor area.

However, exact cell locations are intricate to assess with usual 2D image projections. If structures overlap, it is sometimes difficult to differentiate whether they co-localize or lie behind or in front of each other. 3D reconstructions of confocal laser scanning microscopy z-stacks of RFP- and IB4-/vWF-stained brain sections were obtained in order to further confirm the results shown in Fig. 14 and to capture the spatial relation of the traced cells to vessels more decisively.

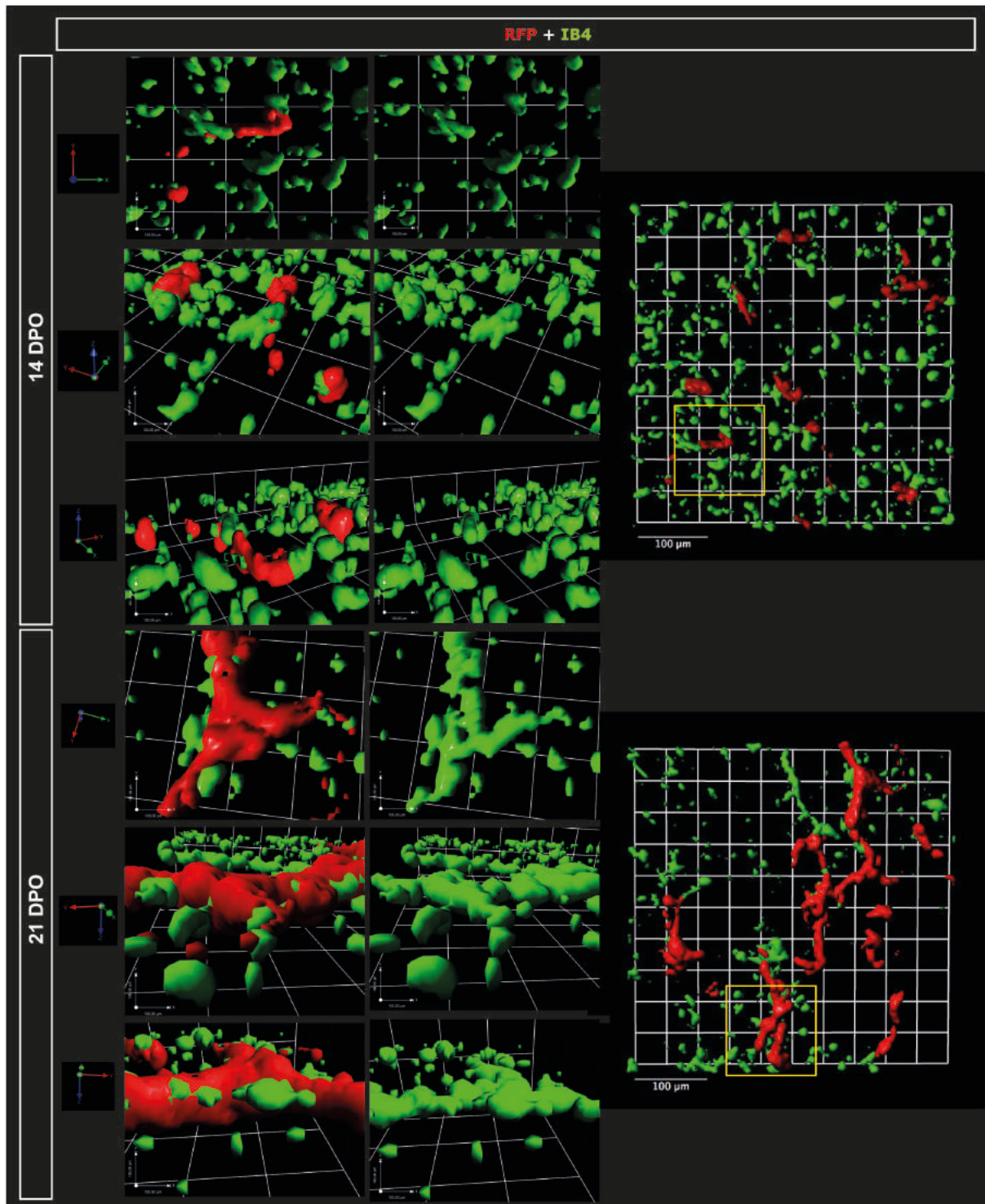


**Fig. 15 3D reconstructions of RFP- and IB4-co-stained brain sections.** Z-stacks of RFP- and IB4-co-stained brain sections obtained by confocal laser scanning microscopy were reconstructed to 3D images (cf. chapter 2.3.7 3D reconstruction). Exclusively 3D reconstructions of the tumor area are shown as RFP positive cells in general and especially RFP positive cells displaying a perivascular location were most predominantly found here. Overviews on the right were taken as xy-frames, i.e. looking from above on the stained sections. The yellow squares indicate the areas of magnification shown on the left as merged picture of both channels and in the green channel. Arrows on the left indicate the orientation of the respective magnifications. Magnifications clearly show that RFP positive cells are twining around IB4-stained vascular structures at 21 DPO, but not at 14 DPO. Scale bars are 100 μm in all images.

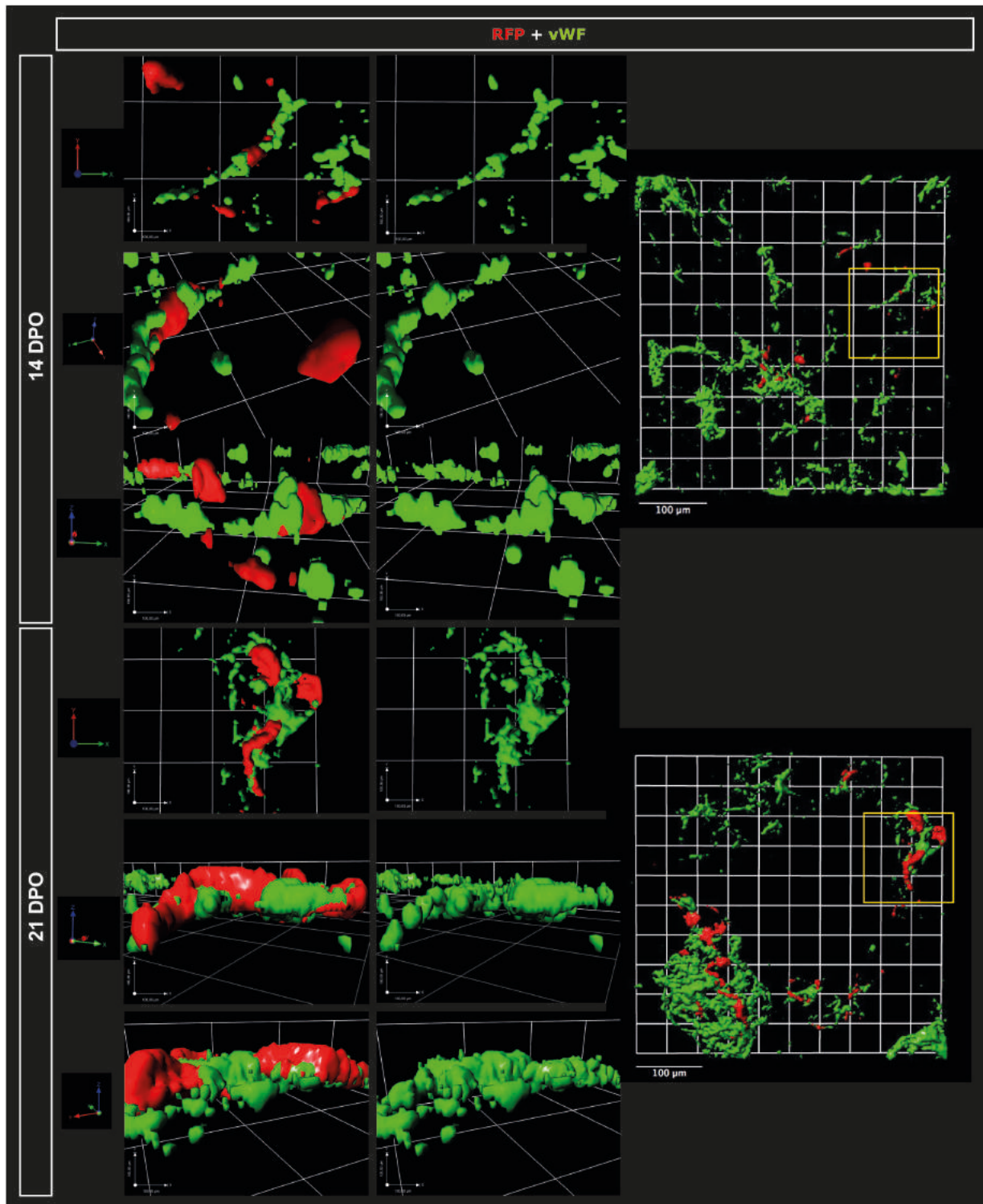


**Fig. 16 3D reconstructions of RFP- and vWF-co-stained brain sections.** Z-stacks of RFP- and vWF-co-stained brain sections obtained by confocal laser scanning microscopy were reconstructed to 3D images (cf. chapter 2.3.7 3D reconstruction). Again, only 3D reconstructions of the tumor area are shown. Overviews on the right are displayed as xy-frames. Areas of magnifications shown on the left-hand side are indicated by yellow squares in the overview images. Arrows on the left indicate the orientation of the respective magnifications. Magnification demonstrate that RFP positive cells are located in a perivascular position at 21 DPO, but largely not at 14 DPO. Large conglomerates of vWF-stained structures at 21 DPO shown on the lower right are typical for tumor vasculature (cf. chapter 1.1.3 Tumor angiogenesis and Apelin/APJ signaling). Scale bars are 100  $\mu\text{m}$  in all images.

As shown in Fig. 15 and 16, after 14 days of tumor growth, the traced cells are small in size and heterogenous in morphology, being disseminated all over the tumor tissue. Their cell bodies are spherical with only very short processes, if any. However, already at this time point, some are located next to vascular structures, albeit most of them are isolated, distributed and in no particular proximity to vessels. This image changes fundamentally after 21 days of tumor progression. Here, the traced cells have increased largely in size forming conglomerates of an elongated, vascular morphology. They now display a juxtaendothelial position irrespective of whether IB4 or vWF was utilized as vascular marker. Almost no RFP positive cell can be exempted from this observation. While indeed not all IB4 or vWF stained vessels are covered by the traced cells, nearly all of the latter cover vascular structures. 3D reconstructions thus confirm the results shown in Fig. 13; the traced cells can now clearly be interpreted to develop into perivascular cells. Notably, all of these aspects apply to pericytes in a tumor context (cf. chapter 1.2.6 Pericytes in gliomas).

Regarding specifically the 3D reconstructed overview of vWF-stained sections at 21 DPO (cf. Fig. 16, lower right), the displayed vessel conglomerates are tumor-typical vascular malformations induced by an unbalanced equilibrium of pro- and anti-proliferative factors in which the former prevails (cf. chapter 1.1.3 Tumor angiogenesis and Apelin/APJ signaling).

#### **4.3.2 Pericyte marker constellation**

Due to morphology, proliferation, and location of the traced cells indicating a potential genesis of pericytes from the latter, sections were immunohistochemically stained for classical pericyte markers, namely the intermediate filament Desmin, the receptor of Platelet-derived growth factor-B (PDGFR $\beta$ ), and Neural/glia antigen-2 (NG2, cf. chapter 1.2.3 Pericyte markers) to assess whether and, if so, to what extent RFP positive cells co-label with them. Co-localization analyses were thoroughly performed by confocal laser scanning microscopy.

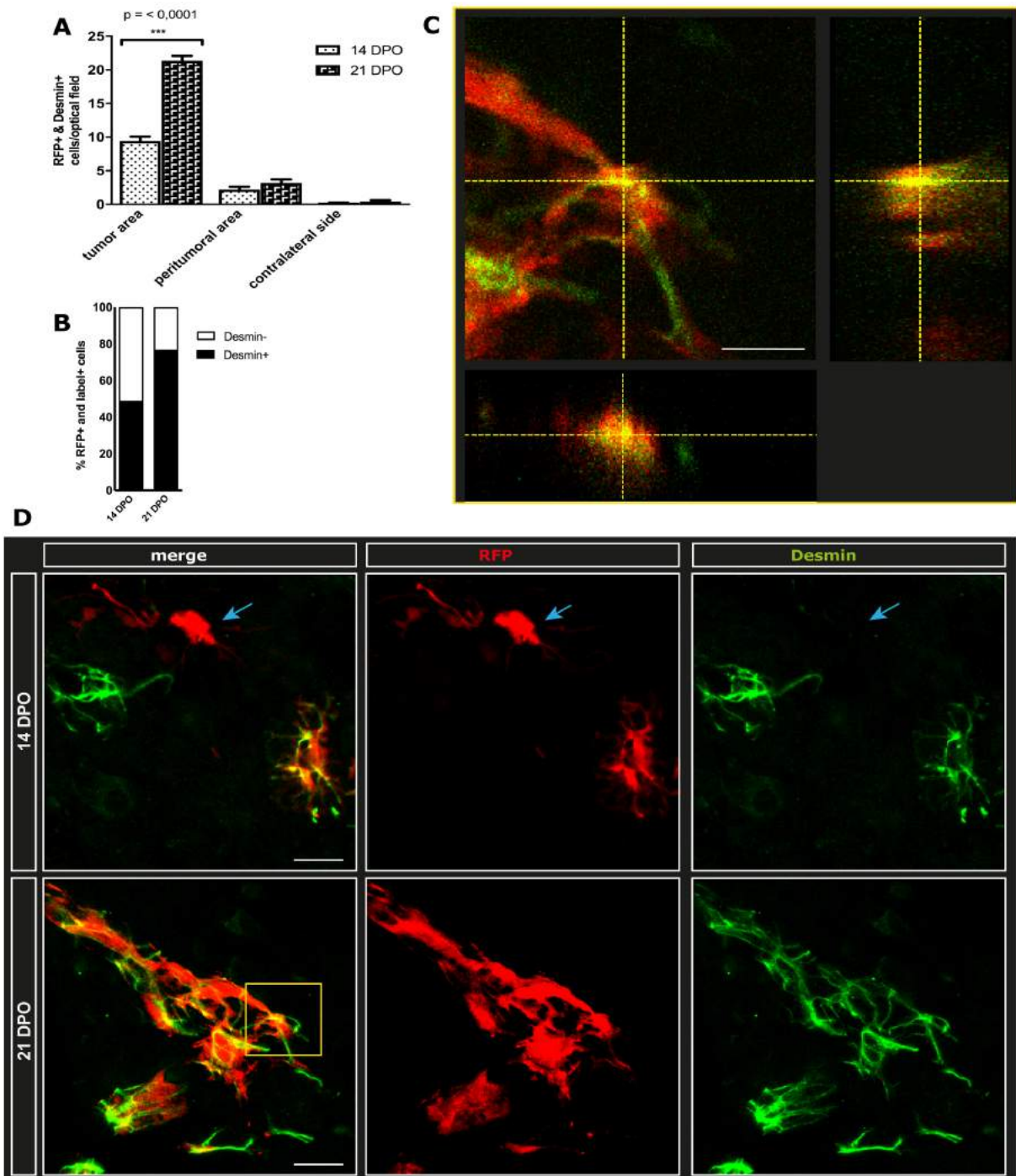


**Fig. 17 Desmin labeling of RFP positive cells.** Quantifications of RFP positive cells were obtained from Desmin co-stained brain sections ( $n = 4$  mice per time point). **A** In the tumor area, RFP positive cells increasingly co-label with the pericyte marker Desmin from 14 to 21 DPO. **B** While at 14 DPO 49,0% of all RFP positive cells also express Desmin, at 21 DPO 76,8% co-label with the pericyte marker in the tumor, indicating that a vast majority of the traced cells develop into pericytes (RFP and Desmin positive) from cells of non-pericyte identity (RFP positive, Desmin negative) if located in glioma tissue as angiogenic stimulus. **C** Co-labeling analyses were performed by confocal laser scanning microscopy. The image was taken in the crosshair mode, corroborating that RFP truly co-labels with Desmin in one single cell. **C** is a magnification of **D** as indicated by the yellow square. In **D** exemplary images from which quantifications (cf. **A**) were obtained are displayed. The blue arrow points at a cell of non-pericyte identity at 14 DPO (RFP positive, Desmin negative). Scale bars are  $10 \mu\text{m}$  in **C**, **D**. Statistical significance between individual time-points is indicated in **A**.

Regarding Desmin stained brain sections, quantifications reveal that after 14 DPO nearly half of all RFP expressing cells co-labeled with the pericyte marker (49,0%), whereas after 21 DPO even about three fourths of them co-localized (76,8%; cf. Fig. 17 A, B, D). Generally, the majority of RFP and Desmin co-labeled cells is clearly located in the tumor, regardless of tumor progression time (cf. Fig. 17 A). Also, only in the tumor a significant increase was observed compared to the two other areas (cf. Fig. 17 A) indicating that predominantly in the neoplasm the traced cells develop into pericytes for this genesis is presumably dependent on tumor progression as angiogenic stimulus. Compared to the total amount of RFP positive cells in the tumor in absolute numbers ( $19,27 \pm 1,548$  (N=48) after 14;  $27,77 \pm 0,6205$  (N=48) after 21 days, cf. Fig. 9),  $9,444 \pm 0,6377$  (N=18) RFP positive cells also express Desmin after 14, already  $21,33 \pm 0,7420$  (N=12) after 21 days.

With respect to the quantifications conducted for perivascular RFP positive cells (cf. Fig. 14 A with IB4 as a vessel marker and Fig. 14 B with vWF as a vessel marker), results furthermore clarify that after 14 DPO not all RFP and Desmin co-positive cells ( $19,27 \pm 1,548$  (N=48), cf. Fig. 17 A) also display a perivascular location, since more RFP and Desmin co-positive cells were counted than perivascular RFP positive cells ( $12,84 \pm 1,443$  (N=32) with IB4 as a vessel marker, cf. Fig. 14 A;  $15,86 \pm 2,463$  (N=7) with vWF as a vessel marker, cf. Fig. 14 B). After 21 days, however, most of the RFP and Desmin double positive cells ( $27,77 \pm 0,6205$  (N=48), cf. Fig. 17 A) are located perivascular as the amount of RFP and Desmin double positive cells is only slightly less than the amount of perivascular RFP positive cells ( $24,25 \pm 1,333$  (N=32) with IB4 as a vessel marker, cf. Fig. 14 A;  $27,00 \pm 1,668$  (N=13) with vWF as a vessel marker, cf. Fig. 14 B). The traced cells thus presumably start to express the pericyte marker Desmin before they display a perivascular location and later on migrate to blood vessels. Moreover, the increase of RFP and Desmin double positive cells from 14 to 21 days ( $8,5 \pm 0,9275$ , cf. Fig. 17 A) is less than the average increase of perivascular RFP positive cells ( $11,41 \pm 0,11$  with IB4 as a vessel marker, cf. Fig. 14 A;  $11,14 \pm 0,795$  with vWF as a vessel marker, cf. Fig. 14 B) indicating that Desmin is expressed earlier than a perivascular location is achieved.

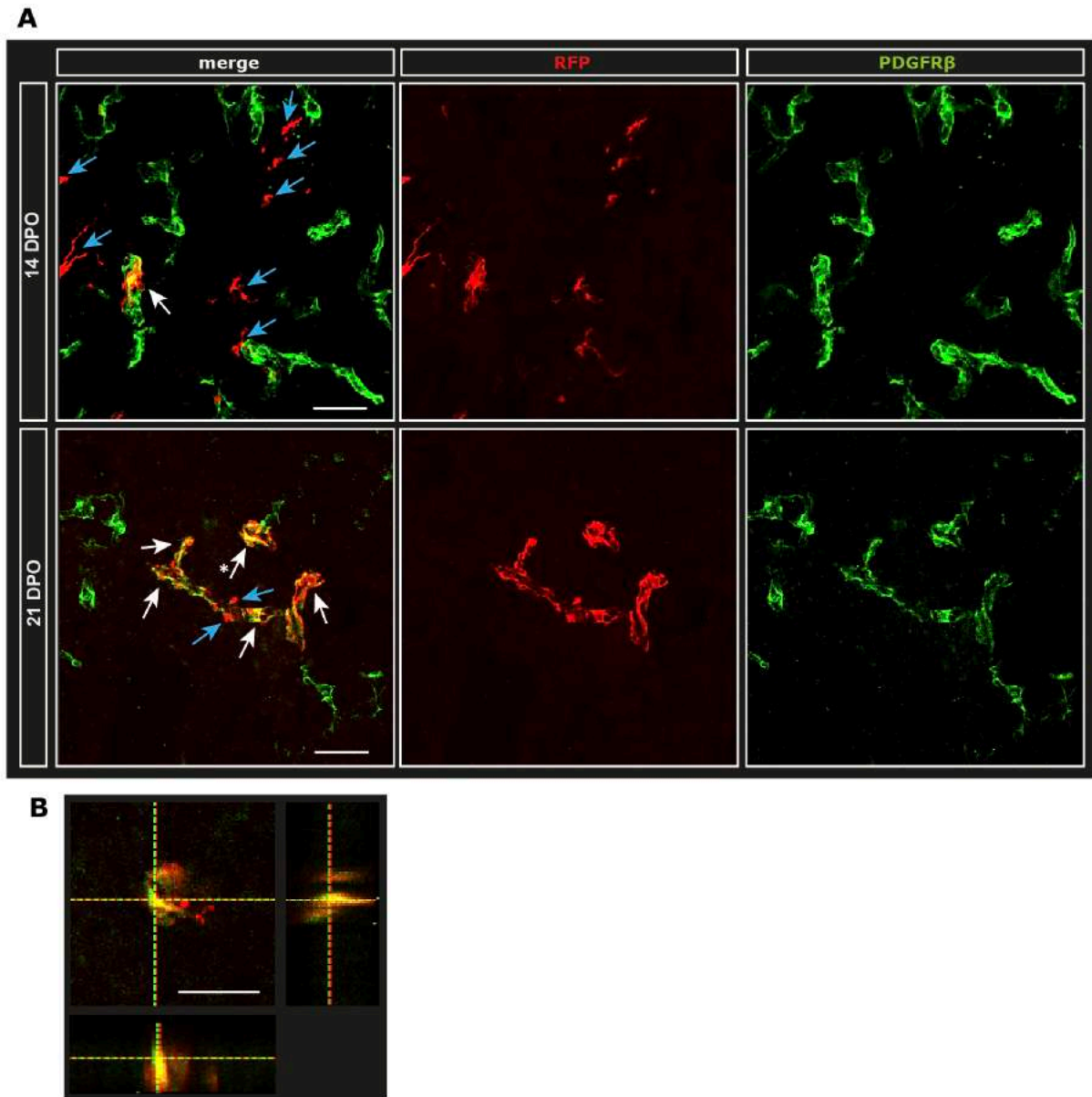


**Fig. 18 PDGFR $\beta$  labeling of RFP positive cells.** Brain sections were stained for PDGFR $\beta$  to assess co-staining of RFP positive cells with said pericyte marker ( $n = 4$  mice per time point). **A** RFP positive cells evermore co-label with PDGFR $\beta$  from 14 to 21 DPO in the tumor, corroborating that the traced cells develop into pericytes (RFP and PDGFR $\beta$  positive) from cells of non-pericyte identity (RFP positive, PDGFR $\beta$  negative). RFP single positive cells (i.e. cells of non-pericyte identity) are indicated by blue, RFP and pericyte marker co-labeled cells (i.e. newly generated pericytes) are indicated by white arrows in **A**. **B** paradigmatically illustrates that RFP and PDGFR $\beta$  blatantly co-label at 21 DPO; the magnification was obtained from **A** as indicated by the starred white arrow. Scale bars are 50  $\mu\text{m}$  in **A**, but 10  $\mu\text{m}$  in **B**.

Regarding PDGFR $\beta$  and RFP co-stained sections, also an increment of co-labeling of the traced cells with the pericyte marker was found from 14 to 21 DPO (cf. Fig. 18 A), similar to the pattern observed on Desmin stained tissue. Again, RFP and PDGFR $\beta$  co-labeled cells were largely found in the tumor and exclusively RFP positive cells in the neoplasm displayed said increase of co-localization with PDGFR $\beta$  over time. This further bolsters the notion that

the traced cells develop into pericytes and that this development depends on exposition to a strong angiogenic stimulus, such as tumor angiogenesis.

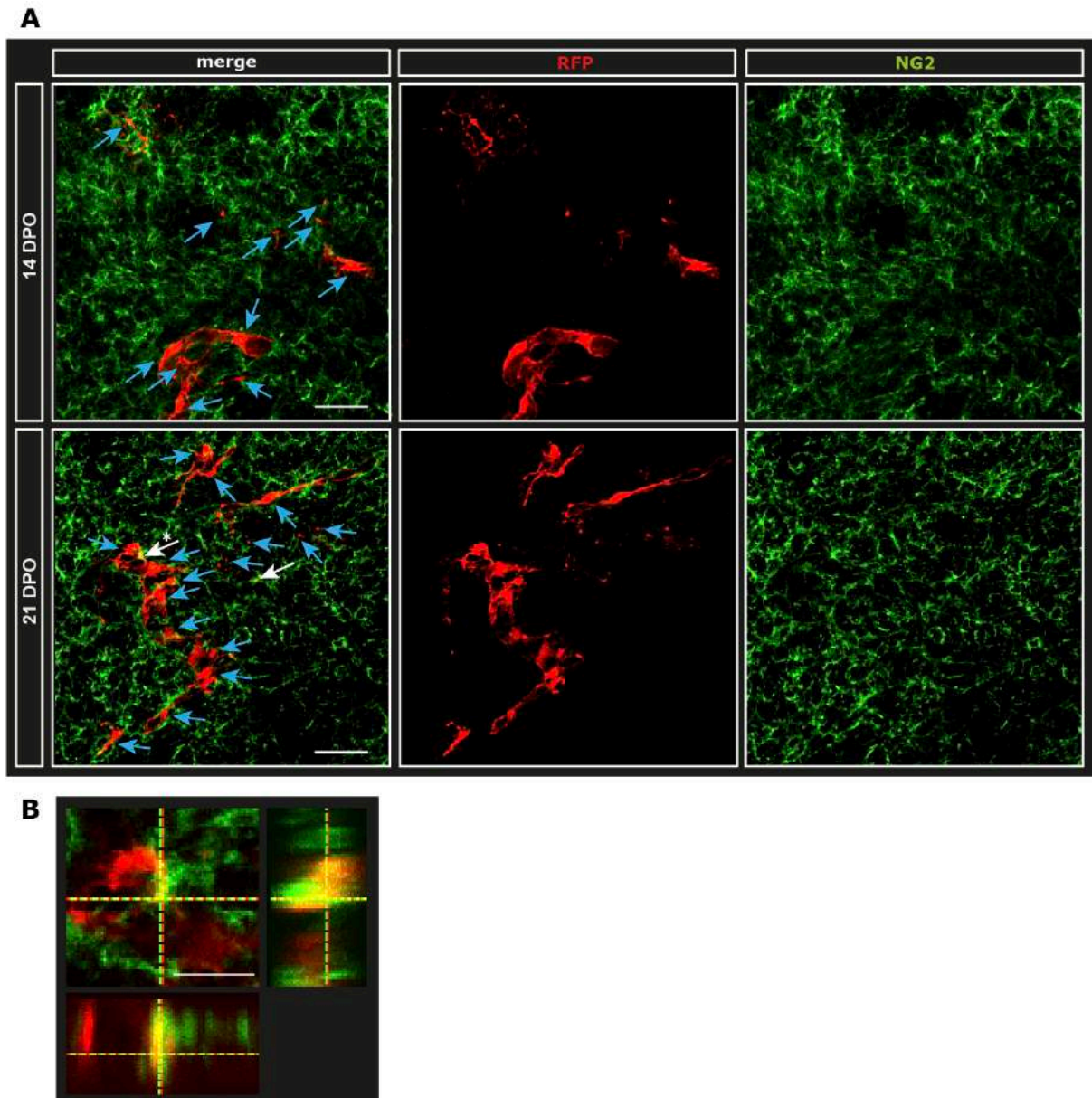


**Fig. 19 NG2 labeling of RFP positive cells.** Brain sections were stained for NG2 to analyze co-staining of RFP positive cells with said pericyte marker ( $n = 4$  mice per time point). **B** RFP positive cells increasingly co-localize with the pericyte marker NG2 from 14 to 21 DPO if located in glioma tissue. Blue arrows indicate RFP single positive cells (i.e. cells of non-pericyte identity); white arrows signal RFP and pericyte marker co-labeled cells (i.e. newly generated pericytes) in A. Besides pericytes, NG2 also labels GL261 glioma cells. **C** exemplarily demonstrates that RFP and NG2 co-label at 21 DPO; the magnification was obtained from B as indicated by the starred white arrow. Scale bars are  $50 \mu\text{m}$  in A, but  $10 \mu\text{m}$  in B.

NG2 also is a well-known pericyte marker, but, by contrast, not only specifically labels pericytes but also GL261 glioma cells. By conducting a NG2 single stain on U87 xenograft glioma tissue, NG2 was confirmed to be a clear pericyte marker in gliomas; since these tumor

cells are NG2 negative, NG2 labeled pericytes were clearly visible in this setting (data not shown). Concerning RFP positive cells, a small amount co-labeled with NG2 after 14 DPO, whereas after 21 DPO many traced cells co-localize with the pericyte marker (cf. Fig. 19 A). This increment was restricted to the traced cells in the tumor tissue, analogously to the observations made on Desmin and PDGFR $\beta$  stains, respectively. Ultimately, results show that all three classical pericyte markers, Desmin, PDGFR $\beta$ , and NG2, co-label with the traced cells to a large extent after 21 DPO, corroborating that a vast proportion of the traced cells have developed into pericytes at that time point.

To further verify that the traced cells increasingly both express pericyte markers and display a perivascular location, brain sections were immunohistochemically stained for RFP, a pericyte (Desmin) and a vessel marker (IB4) combined. Co-localization analyses were thoroughly performed by confocal laser scanning microscopy. Evaluations show that after 21 DPO RFP and Desmin double positive cells are mainly located next to an IB4 positive structure (cf. Fig. 20). These findings altogether corroborate that a vast proportion of the traced cells have developed into pericytes in glioma tissue at 21 DPO.

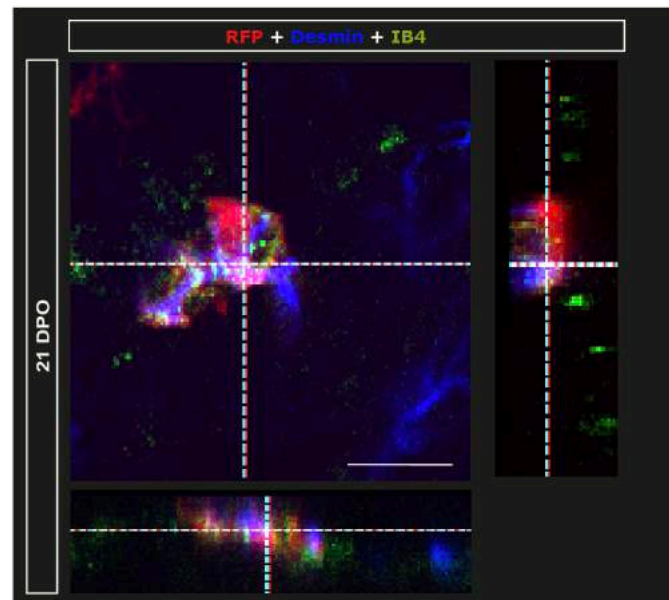


**Fig. 20 Pericyte marker co-labeling of perivascular RFP positive cells.** Brain sections were immunohistochemically stained for both a pericyte (Desmin) and a vessel marker (IB4). The image shows RFP and pericyte marker co-labeled cells in a juxtaendothelial position at 21 DPO in glioma tissue, bolstering the evidence that the traced cells evolve to pericytes if located in the tumor. Scale bars are 10  $\mu$ m.

At 14 DPO, however, many RFP positive cells are not located in a perivascular position on both IB4 and vWF co-stains, respectively, (cf. Fig. 13 E; Fig 14; Fig. 15) and do not express pericyte markers (Desmin/PDGFR $\beta$ /NG2, cf. Fig. 16 B, D; Fig. 17 A, B). At these early stages, the traced cells therefore do not display pericyte characteristics, albeit they develop into pericytes later. The findings of this study thus propose a previously unrecognized lineage of tumor-associated pericytes.

### 4.3.3 Lack of Iba1 expression

As shown in the previous chapters, from 14 to 21 DPO, the traced cells increasingly express mature pericyte markers and are located next to blood vessels. The latter feature, however, is also a characteristic of myeloid cells, such as microglia and macrophages, especially in an oncological context. RFP positive cells were therefore analyzed for Iba1- and IB4-co-localization, both well-known markers for myeloid cells, in order to assess whether they develop into cells of the myeloid lineage.

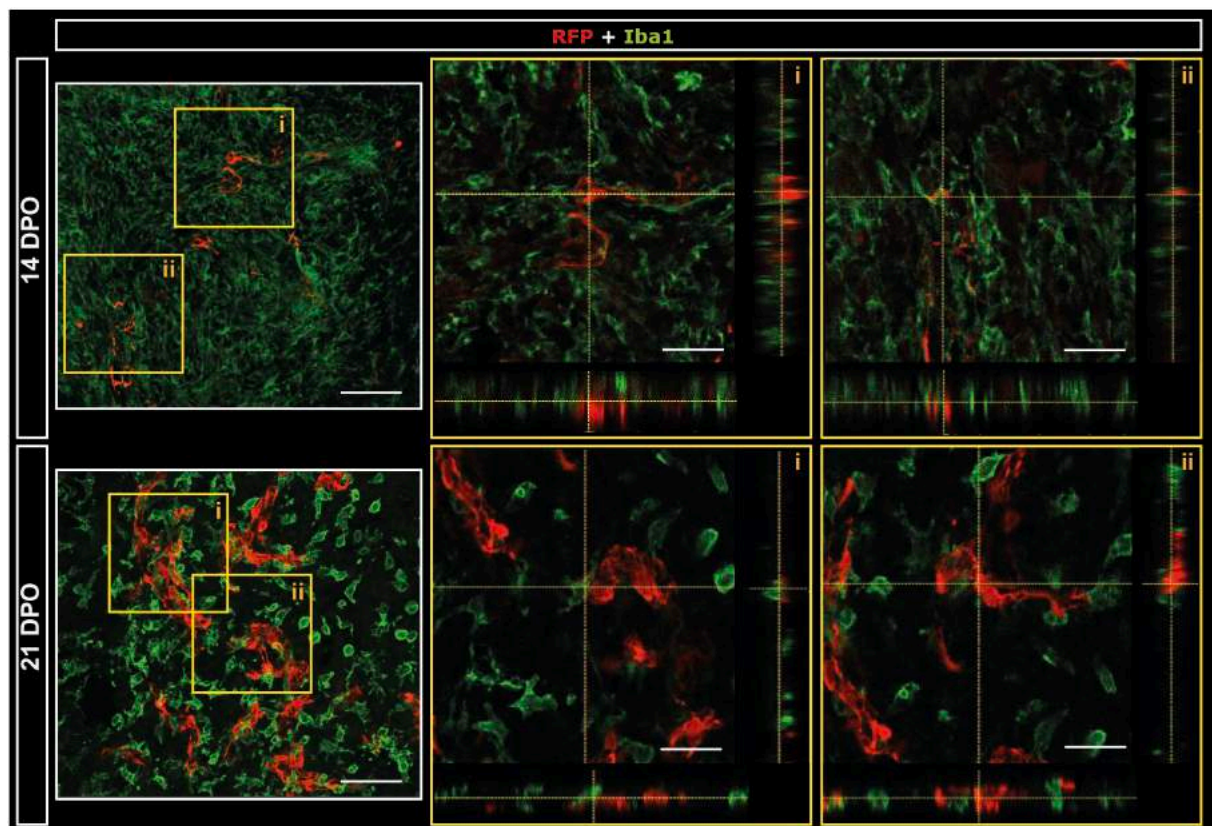


**Fig. 21 RFP positive cells do not co-label with Iba1.** Brain sections were immunohistochemically stained for the myeloid marker Iba1 to assess possible co-labeling with RFP positive cells. As the images at hand show, RFP positive cells do not co-localize with Iba1, indicating that the traced cells do not develop into myeloid cells, such as microglia or macrophages. Yellow squares (i, ii) indicate the original locations of the magnification shown in the middle and on the right-hand side. All images were obtained by confocal microscopy and the magnifications (i, ii) are displayed in the crosshair mode (cf. chapter 3.2.6.3 Confocal microscopy). Scale bars are 50  $\mu$ m in maximal projections, but 10  $\mu$ m in magnifications.

As Fig. 19 illustrates, RFP positive cells do not co-label with Iba1, neither after 14 nor after 21 DPO. The traced cells are often located directly next to an Iba1 positive microglia or macrophage, but do not co-localize with the marker. The same applies to IB4, which stains both microglia, macrophages and vessels (cf. Fig. 14 E, Fig. 15). Just as stated above, the latter were differentiated by morphology (large spherical-ellipsoid somata with branched processes of microglia and macrophages versus narrow, elongated cell bodies with flat nuclei of endothelial cells). This altogether indicates that the traced cells do not develop into Iba1 expressing myeloid cells.

#### **4.3.4 Pericyte subtypes**

Pericytes can be classified in different subtypes, most commonly based on specific marker constellations, which are then taken as indicators for divergent functional profiles. Concerning pericytes in an oncological context, Birbrair and colleagues have introduced a classification which differentiates so-called type-1- from type-2-pericytes (cf. chapter 1.2.4 Pericyte subtypes): Type-1-pericytes are NG2 positive and Nestin negative; type-2-pericytes are NG2 and Nestin co-positive. While both subtypes are morphologically identical, they differ in their functions: Only type-2-pericytes participate in tumor angiogenesis, are angiogenic *in vivo* as well as *in vitro*, and participate in vessel recovery after ischemia; type-1-pericytes do not display any of said functions [135].

A modified version of this classification was chosen to further characterize the traced cells in the present study. Since NG2 stains turned out to be difficult to analyze due to NG2 expression of GL261 glioma cells (cf. Fig. 19 A, B), this marker was not included in the classification at hand. Instead, Desmin, which has already proved to co-label with a comparable amount of RFP positive cells like NG2 and is a well-established pericyte marker (cf. chapter 1.2.3 Pericyte markers) was selected. Nestin was taken as second marker, just as in the original classification proposed by Birbrair and colleagues [135]. However, just as NG2, Nestin is also expressed by GL261 glioma cells, but Nestin stained brain sections of U87 glioma xenografts (Nestin negative) could validate the marker as a clear label for pericytes in a glioma context (data not shown). Desmin and Nestin co-stains could thus be performed to differentiate pericyte subtypes in the traced pericyte population.

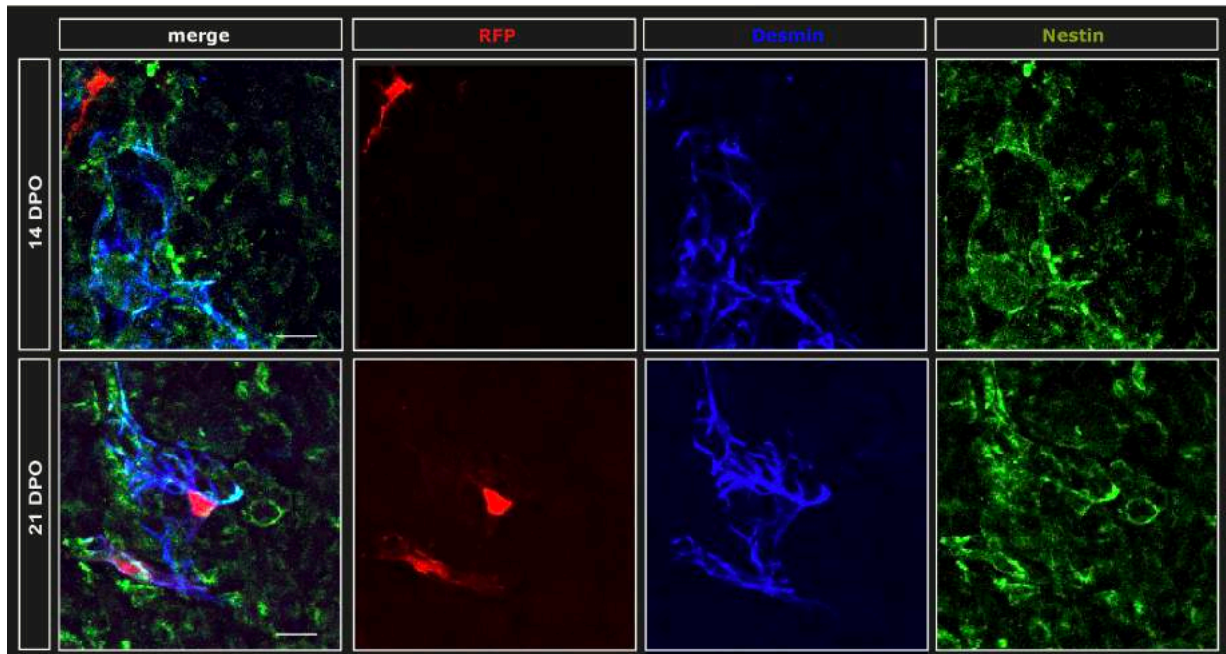


**Fig. 22 RFP positive cells do not develop into different pericyte subtypes.** Brain sections were immunohistochemically stained for both the pericyte marker Desmin and Nestin to potentially differentiate pericyte subtypes in the traced pericyte cell population. Based on a classification introduced by Birbrair et al., pericytes were discerned as either Desmin positive and Nestin negative or as both Desmin and Nestin positive. As already described in Fig. 16 A-D, the traced cells increasingly co-localize with Desmin from 14 to 21 DPO. However, at neither 14 nor 21 DPO RFP positive cells co-label with both Desmin and Nestin. Concerning the classification at hand, the traced pericyte cell population does therefore not develop into different pericyte subtypes. Scale bars are 50  $\mu\text{m}$  in all images.

With regards to all pericytes labeled by Desmin in the tumor, both Desmin and Nestin co-positive cells and Desmin single positive cells were found in comparable amounts (cf. Fig. 22). The same applies to the peritumoral as well as the contralateral area. Thus, no conclusion towards more or less participation of one subtype in tumor angiogenesis can be drawn.

Concerning the traced pericyte population, none of the RFP and Desmin double positive cells co-labeled with Nestin at 14 DPO (Fig. 22). Analogously, RFP single positive cells did not co-localize with Nestin at that time point. At 21 DPO, again neither RFP and Desmin co-positive cells nor RFP single positive cells co-label with Nestin, ultimately indicating that the traced cells do not develop into divergent pericyte subtypes.

#### 4.3.5 Apelin/APJ expression

The traced cell population as well as pericytes in general were additionally analyzed for co-localization with Apelin and its receptor APJ, both of which are known to mediate glioma angiogenesis [84] (cf. chapter 1.1.3 Tumor angiogenesis and Apelin/APJ signaling). Brain sections were stained for either Apelin or APJ, respectively, in order to assess whether the

traced cells which have already obtained a pericyte phenotype express said markers. Co-labeling analyses were performed by confocal microscopy.

The Apelin antibody utilized in this study is directed against human Apelin but also labels its murine isoform and could thus be applied to stains of mouse brain tissue in the present experiment [84]. The used APJ antibody is directed against the rat APJ receptor; however, it also reacts with murine APJ and can consequently also be exerted for APJ detection in mice [84]. Both antibodies have already been shown to sufficiently stain for their respective target on mouse tissue [177] and Apelin control stains on Apelin knock-out mice were negative (data not shown), confirming the validity of the stains conducted in this study.

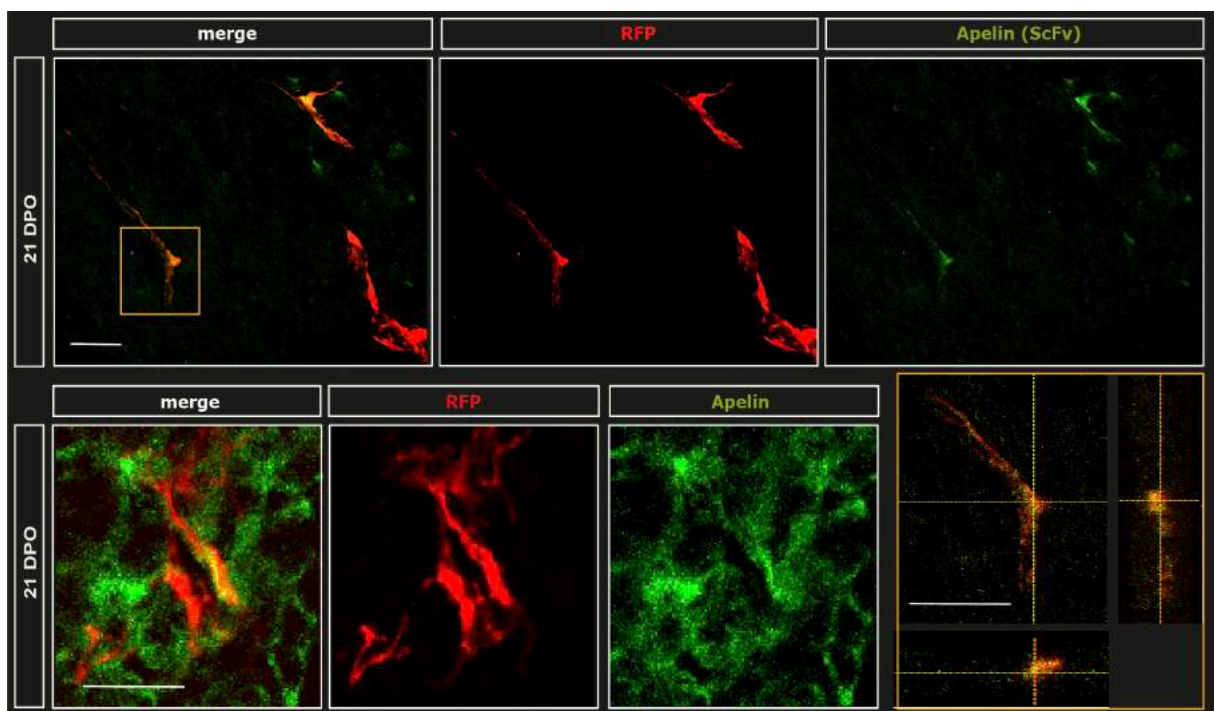


**Fig. 23 Apelin labeling of RFP positive cells.** Brain sections were immunohistochemically stained for Apelin in order to investigate whether RFP positive cells co-label with the marker. At 21 DPO, a subset of RFP positive cells co-localize with Apelin. Images in the upper row illustrate several RFP positive cells, two of which co-label with Apelin. One RFP and Apelin double positive cell was additionally magnified and displayed in the crosshair mode (image in the right-hand corner), as indicated by the yellow square. Co-labeling of RFP positive cells with Apelin is restricted to the tumor area; in the peritumoral area and contralateral hemisphere, the traced cells do not co-label with Apelin. Brain sections were stained with an anti-Apelin ScFv (images in the upper row) and an anti-Apelin antibody (images in the row underneath), respectively, both of which revealed the same result. Scale bars are 10  $\mu$ m in all images.

Generally, Apelin was found both in GL261 glioma cells (cf. Fig. 23), in cells of the peritumoral tissue and in the contralateral area. In the latter two regions, it was expressed in the cytoplasm of glial cells, most predominantly in astrocytes, judging from morphology. More Apelin positive glial cells were found in close proximity to the tumor; especially peritumoral

astrocytes expressed the marker (data not shown). Astrocytes are known to surround glioma tissue being hypertrophic, activated and involved in peritumoral edema generation as well as in inflammation processes [68]. Just as astrocytes in general, it has previously been established that they express Apelin [80]. These results hence confirm the validity of the conducted stain in this study.

As shown in Fig. 23, co-labeling of RFP positive pericytes with Apelin was found in a subset of cells after 21 days of tumor progression. This finding was clearly validated by RFP and Apelin double stains with single-chain fragment variables (ScFv, cf. Fig. 23): An anti-Apelin ScFv (C12) distinctly co-labeled with a proportion of the traced cells at 21 DPO. The majority of the RFP positive cells, however, remained Apelin negative.

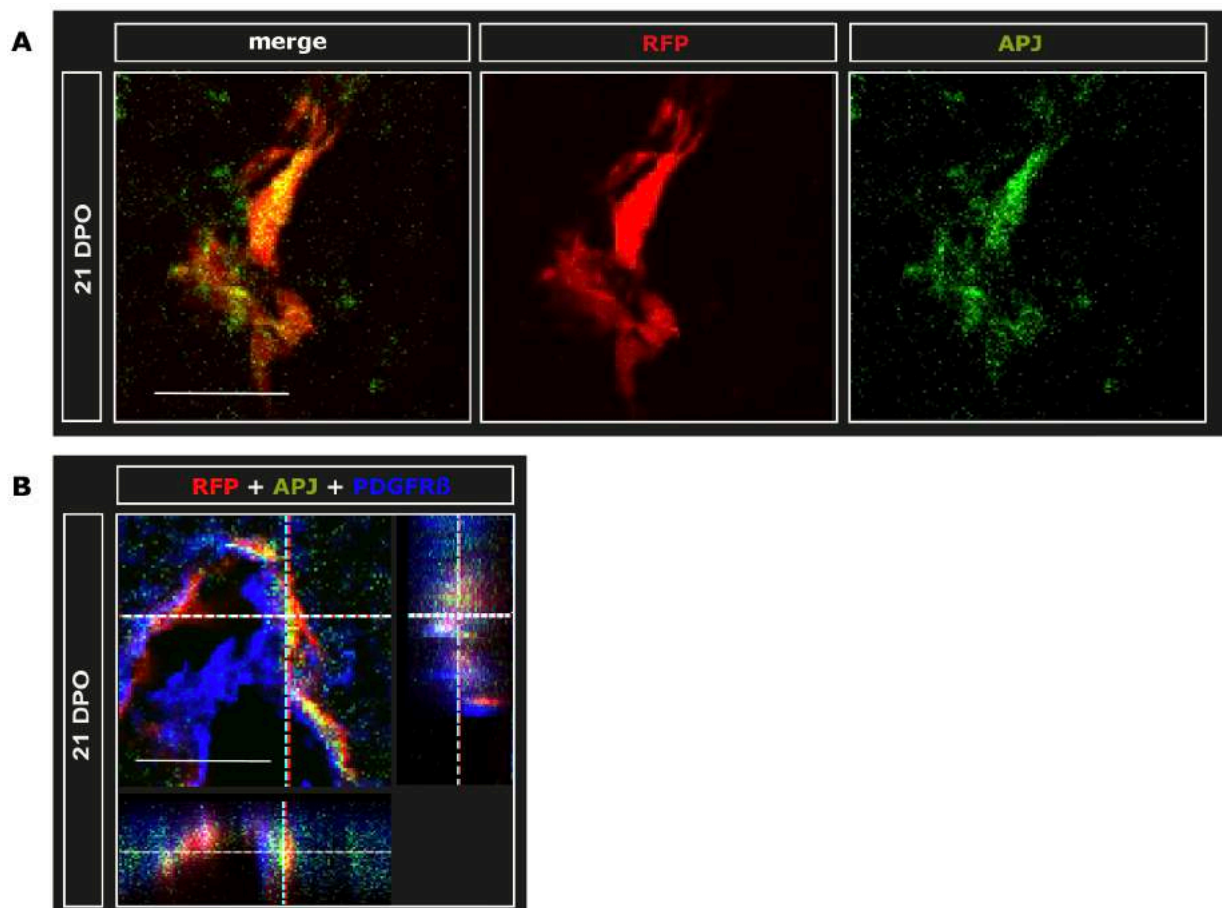


**Fig. 24 APJ labeling of RFP positive cells.** For assessing co-labeling of RFP positive cells with APJ, brain sections were immunohistochemically stained for APJ as well as APJ and PDGFR $\beta$ , respectively. **A** A proportion of RFP positive cells co-localize with APJ at 21 DPO. This co-localization is restricted to RFP positive cells located in the tumor area. **B** Especially the traced cells which co-label with PDGFR $\beta$  and therefore have obtained a pericyte identity co-label with APJ. Scale bars are 10  $\mu$ m in all images.

Just as Apelin, APJ is expressed by GL261 tumor cells. In the tumor, it was furthermore found in vascular structures. Regarding the peritumoral and contralateral area, APJ was

detected most predominantly in glial cells, not cytoplasmatically as Apelin, but nuclearly, and an increasing number of APJ positive cells was found in closer proximity to the tumor. In contrast to the tumor area, peritumoral vascular structures were APJ negative (data not shown), analogous to Apelin, indicating that APJ may influence specifically tumor vasculature.

Furthermore, a subset of RFP positive cells co-label with APJ after 21 DPO (cf. Fig. 24 A). APJ also co-localizes with PDGFR $\beta$  labeled pericytes in the tumor tissue, irrespective of RFP co-staining. Again, this does not apply to all PDGFR $\beta$  labeled pericytes, but to some, eventually a certain subpopulation. In the peritumoral and contralateral area, PDGFR $\beta$  and APJ do not co-localize. APJ consequently might play a role in a certain subpopulation of tumor-associated pericytes.

Regarding the RFP positive cells, which co-express PDGFR $\beta$ , i.e. the traced cells which have already obtained a pericyte phenotype, APJ was found in some after 21 DPO (cf. Fig. 24 B). Hence, just as the total, PDGFR $\beta$  positive pericyte population, also the traced pericyte population partly expresses APJ increasing with their maturity.

Overall, both Apelin and APJ is expressed by the traced cells. This expression, however, is restricted to the traced cells located in the tumor and is limited to a certain proportion of the traced cells, namely the ones which have developed into tumor-associated pericytes.

## 5. Discussion

### 5.1 The pericyte-lineage

Up until now, the ontogeny of pericytes is only poorly understood. A variety of studies suggest that pericytes in the CNS are neural crest derived, but findings regarding the lineage of pericytes in both physiological and pathological conditions are strikingly heterogenous [100]. Particularly the cellular origin of tumor-associated pericytes remains largely elusive. It is often assumed that they derive from tumor surrounding, mature pericytes which infiltrate the neoplastic tissue, but scientific evidence therefore has not been provided as of yet (cf. chapter 1.2.5 Pericyte ontogeny and chapter 1.2.6 Pericytes in gliomas) [100].

In the study at hand, the ontogeny of pericytes was re-investigated in NesCreER<sup>T2</sup> x Ai9tdTomato double transgenic mice, which were orthotopically inoculated with GL261 murine glioma cells. This mouse model allowed tracing the lineage of Nestin expressing cells (Nestin positive at the time of Tamoxifen administration, cf. chapter 3.2.2 Treatment protocol) during high-grade glioma angiogenesis in vivo with RFP as reporter.

The traced cells were most abundantly found in glioma tissue and increased in amount between the two investigated time points, 14 and 21 days after tumor inoculation. While at earlier time points of tumor progression (14 DPO) the traced cells are small, heterogenous in morphology, and disseminated in the neoplastic tissue, they develop to large conglomerates of several traced cells displaying an elongated structure in further progressed glioma stages (21 DPO). Moreover, the traced cells are increasingly found in a perivascular location the further the tumor progresses, but do not co-localize with classical vessel markers (IB4, vWF). 3D reconstructions of confocal laser scanning microscopy z-stacks corroborated that the traced cells do not co-label with endothelial cell markers such as IB4 and vWF, but wind around vessels, suggesting that they develop into perivascular cells. Indeed, the traced cells incrementally obtain typical pericyte markers (Desmin, PDGFR $\beta$ , NG2) during the time course of gliomagenesis. Since juxtaposition with endothelial cells and expression of different pericyte markers are the defining criteria for pericyte identification [96, 100, 115], it was concluded that the traced cells develop into pericytes over the observed time course. As at early stages of tumor progression (14 DPO) the traced cells do not display a pericyte-like morphology, are largely not located in close apposition to endothelia, and mainly do not express typical pericyte markers, the lineage-tracing experiment of this doctoral thesis has revealed that pericytes develop from cells of non-pericyte identity, which in turn originate from Nestin expressing cells (Nestin positive at the time of Tamoxifen administration). Also, this shift in morphology, localization, and pericyte marker expression of the traced cells during glioma progression was

most abundant in the tumor, compared to the peritumoral area and the contralateral hemisphere, indicating that the development of pericytes from cells of non-pericyte identity is dependent upon a strong angiogenic stimulus.

The ontogeny of pericytes has been investigated in previous lineage-tracing studies using pericyte marker (e.g. PDGFR $\beta$  or NG2) reporter lines. For instance, Song and colleagues have proclaimed that tumor derived PDGFR $\beta$  positive perivascular progenitor cells have the capacity to develop into pericytes in pancreatic carcinoma [124]. Although studies of that kind have provided relevant insights into pericyte progeny, their scope remains restricted to the experimental assessment of cell-populations committed to a pericyte-phenotype. The Nestin reporter mouse model utilized in this study, by contrast, is pericyte marker-independent and thereby allows tracing a broader range of the pericyte lineage, leading to the novel finding that tumor-associated pericytes derive from the cells of non-pericyte identity characterized in this thesis.

Evidence indicates that pericytes are strikingly plastic cells [178] and stages of trans-differentiation of pericytes into myeloid cells and vice versa have been repeatedly reported in the literature [179, 180]. In response to a range of pathological conditions pericytes were suggested to be a novel source of microglia/macrophages in the CNS [180]. Besides, Elmore and colleagues have suggested that microglia may derive from a brain-resident Nestin positive progenitor which was demonstrated to be Iba1-negative but developed into Iba1-positive microglia [181]. However, in the study at hand, it was shown that the traced cells do not express the microglia/macrophage-specific calcium binding protein Iba1 at the investigated time points 14 and 21 DPO throughout their development.

Another protein that is regularly used as identification marker for microglia and macrophages is CD11b, which is also known as Integrin alpha M (ITGAM) [182, 183]. Importantly, it has so far not been found to be expressed by pericytes [96, 100]. However, further experiments conducted in the Neurosurgical Research Laboratory, where the project of this dissertation was performed, have demonstrated that many of the traced cells, which were characterized in this study, express CD11b, mainly at later stages of tumor growth (data not part of this thesis). These findings may be explained by successive differentiation of the traced cells of non-pericyte identity first to tumor-associated pericytes (at 14 and 21 DPO) followed by trans-differentiation to CD11b positive cells afterwards. Another alternative explanation of these new findings would be that a sub-population of the traced cells of non-pericyte identity (at 14 DPO) develops directly into CD11b positive cells (without acquiring a pericyte phenotype in between), whilst concomitantly another sub-population develops into the CD11b

negative pericytes characterized in this thesis. Trans-differentiation of pericytes into myeloid cells and vice versa has been repeatedly demonstrated in the literature [179, 180]. Nonetheless, vast majority of the traced cells clearly fulfill all available criteria for pericyte identification at 21 DPO and therewith should be defined as pericytes at that time point [96, 100, 115]. The cell development investigated in the doctoral thesis at hand can, hence, still be interpreted as newly identified lineage of tumor-associated pericytes.

Continuous and rapid proliferation is a well-established feature of less differentiated cells [184]. As cells differentiate, their proliferation rate usually decreases [185]. Preclinically, proliferative behavior is commonly assessed by thymidine analogue uptake experiments [53]. In the study at hand, two thymidine analogues, CldU and IdU, were therefor injected into Nestin reporter mice at different time points, respectively (CldU 2 days, IdU 5 hours before sacrifice, cf. chapter 3.2.2 Treatment protocol). In addition to a general assessment of cell proliferation, this CldU/IdU labeling paradigm allows the specific detection of continuously proliferating (CldU and IdU double-labeled) cells, and fast proliferating (IdU-labeled) cells, since if cells proliferate rapidly, they dilute-out the earlier administered thymidine analogue. This interpretation of the CldU/IdU-labeling protocol was made in concordance with prior thymidine analogue uptake studies [170, 171]. As this study has shown, the traced cells (to a remarkable extent) stay in the cell cycle (i.e. incorporate thymidine analogues), even if compared to proliferatively active glioma cells surrounding them, and to an astounding proportion also proliferate continuously. Furthermore, traced cells which have not yet acquired a pericyte phenotype (as determined by the absence of close apposition to endothelia in this experiment) are more likely to proliferate rapidly compared to traced cells which have already obtained a pericyte phenotype (judging from the presence of juxtaendothelial position), suggesting that the development of the traced cells of non-pericyte identity into pericytes depicts a process of cell differentiation. However, the cells of non-pericyte identity (at 14 DPO) cannot be delineated as pericyte progenitor [-like] cells, for, as mentioned earlier, further experiments that are not part of this dissertation have shown that the traced cells express CD11b at later time points of tumor growth, which is incompatible with a pericyte phenotype, and progenitor cells are commonly defined as committed to one cell phenotype [185]. Nevertheless, the data demonstrated in this thesis establishes and characterizes a previously unrecognized lineage of pericytes, since not all traced cells express CD11b at later stages of tumor expansion but hold onto their pericyte expression profile (data not part of this thesis).

## 5.2 The pericyte-lineage in glioma angiogenesis

Glioblastoma multiforme is the most common and most aggressive primary brain tumor in adults with a median overall survival of only 13-15 months despite therapy [19]. In addition to rapid and diffuse invasiveness, GBM is, amongst other features, characterized by exorbitant neo-vascularization [12, 24]. In the study at hand, NesCreER<sup>T2</sup> x Ai9tdTomato mice were orthotopically inoculated with GL261 glioma cells. GL261 is a syngeneic murine glioma cell line, which is frequently used as a model for high-grade gliomas like GBM in preclinical as well as translational research, and represents one of the few available immunocompetent glioma mouse models [186, 187]. It reliably generates highly angiogenic tumors in cohorts of mice with consistent histopathological attributes [167], making it a realistic high-grade glioma model for the study of tumor-associated pericytes in this thesis. The tumor cell proliferation rate has additionally been investigated as part of the evaluation of the CldU/IdU thymidine analogue labeling paradigm conducted in this dissertation and confirmed a high cell turnover typically seen in high-grade gliomas (cf. chapter 4.2.1 CldU/IdU labeling).

The study at hand has shown that new pericytes develop from cells of non-pericyte identity, which in turn originate from Nestin expressing cells (Nestin positive at the time of Tamoxifen administration), within intracranial high-grade gliomas, suggesting that pericytes play an important role in tumor angiogenesis. Indeed, it is well established that pericytes, amongst other features, maintain the integrity of the BBB [96], display contractile functions to govern vasodilatation and -constriction [148], thereby regulate the clearance of toxic metabolites [100], and most importantly control angiogenesis [111], also in neoplastic tissue [96]. As introduced earlier, they are a pivotal part of the tumor microenvironment and facilitate tumor growth by promoting endothelial cell survival [188] and fostering immunosuppression [189, 190] (cf. chapter 1.2.6 Pericytes in gliomas).

The origin of tumor associated pericytes has remained an unresolved question up until now [100]. In the literature, it is usually assumed that they originate from tumor surrounding, mitotically inactive pericytes [100]. Previous studies have suggested that they may derive from immature mesenchymal cells within the neoplasm [155]. Other authors propose that pericytes in tumors derive from the bone-marrow [156, 157], as in high-grade gliomas the BBB is disrupted making such a migration theoretically plausible [24]. In addition, Bexell and colleagues have demonstrated that bone-marrow derived MSCs share characteristics of pericytes in high-grade gliomas, including expression of pericyte markers ( $\alpha$ SMA, PDGFR $\beta$ , NG2), tumor tropism, and integration into the vessel wall [191]. In the present study it was illustrated that cells of non-pericyte identity differentiate into mature pericytes particularly in

the tumor, but not in the peritumoral area or contralateral hemisphere (cf. Fig. 23). Quite remarkably, those newly formed pericytes appear to derive from a cell population of non-pericyte identity that may be endogenous to the brain as the traced cells were exclusively found here and not in other organs (data not part of this thesis). This finding does not stand in conflict with previous studies as pericytes from a single tissue were demonstrated to originate from multiple sources [192].

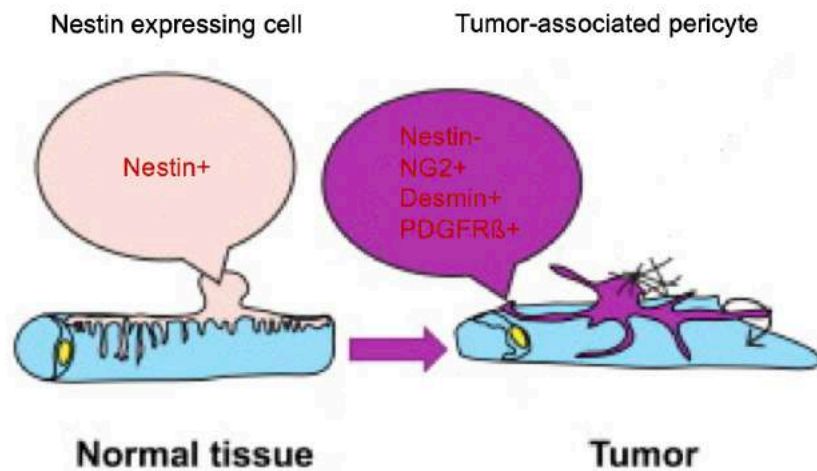


**Fig. 25 The ontogeny of tumor-associated pericytes from Nestin expressing cells.** Findings of the study at hand show that pericytes (Nestin negative, pericyte marker [NG2, Desmin, PDGFR $\beta$ ] positive) in high-grade gliomas develop from Nestin expressing cells (Nestin positive at the time of Tamoxifen administration). Adapted from [100].

According to prior findings, recruitment of pericytes to tumor parenchyma is mainly mediated by the PDGF $\beta$ /PDGFR $\beta$  pathway, which was also shown to govern recruitment of pericytes under physiological conditions [96, 100, 150]. Notwithstanding, in this study, the traced cells express PDGFR $\beta$  in later stages of tumor progression (21 DPO) when they have already obtained a pericyte phenotype (as determined by pericyte marker expression and juxtaendothelial location), but not at earlier time points of tumor growth (14 DPO) when they have not yet acquired pericyte features. Recruitment of the cells of non-pericyte identity characterized in the dissertation at hand is therefore most likely independent from the PDGF $\beta$ /PDGFR $\beta$  pathway. Other proposed mechanisms for tumor-associated pericyte recruitment suggest an additional role of HB-EGF in a model of pancreatic carcinoma [151] and of EGFR positive pericytes in the development of resistance against antiangiogenic therapy in a model of lung cancer [152]. Whether the traced cells of non-pericyte identity investigated

in this study are recruited during gliomagenesis by the latter or other pathways remains a subject of future investigations.

Morphological and molecular studies to characterize pericyte identity have recently pointed out a heterogeneity in pericyte population of the CNS [193]. For instance, while some pericytes are lining alongside arteries, others exhibit a mesh star-shape on post-capillary venules, with intermediate cells displaying mixed morphologies [194]. In accordance with these morphological varieties, latest attempts to provide a pericyte transcriptome strongly suggested the existence of several pericyte subtypes [111, 193, 195-199]. In the literature, pericyte subtypes are commonly identified by different marker profiles, which are then taken as indicators for divergent functions [100]. With regard to tumor-associated pericytes, Birbrair and colleagues have introduced a classification which differentiates so-called type-1- from type-2-pericytes (cf. chapter 1.2.4 Pericyte subtypes): Type-1-pericytes are NG2 positive and Nestin negative; type-2-pericytes are NG2 and Nestin co-positive. While both subtypes are morphologically identical, they differ in their functions: Type-2-pericytes, but not type-1-pericytes, participate in tumor angiogenesis, are angiogenic *in vivo* as well as *in vitro*, and participate in vessel recovery after ischemia [135]. Due to NG2 expression of the GL261 glioma cell line, which was utilized as high-grade glioma model in the study at hand, and commensurate expression of NG2 and Desmin of the traced cells, subtype identification of the traced cells was conducted by co-labeling analysis of the traced cells with Desmin and Nestin. Quite remarkably, the traced cells become increasingly Desmin positive the further the tumor progresses, as described earlier, but do not co-label with Nestin throughout their development, indicating that they do not develop into different pericyte subtypes during glioma angiogenesis.

Pericytes are known to display pivotal functions including tumor angiogenesis, vessel formation, and remodeling of the vasculature, all of which they fulfill in interaction with endothelial cells [200]. A range of signaling pathways has been reported to mediate pericyte-endothelial cell communication including Notch [201], angiopoietins [202], Sphingosin-1-phosphate [203], transforming growth factor  $\beta$  (TGF $\beta$ ) [204] and PDGF $\beta$  [205, 206]. As it was shown in this study, the receptor of the latter (PDGFR $\beta$ ) is expressed by a majority of the traced cells in further progressed tumor stages (21 DPO), but not at earlier time points of tumor expansion (14 DPO). This finding suggests that the traced pericyte population might interact with endothelial cells via the PDGF $\beta$ /PDGFR $\beta$  pathway as soon as they have acquired a pericyte phenotype. In addition to that, the present study indicates that the traced cells which have obtained a pericyte phenotype may interact with endothelial cells via the Apelin/APJ pathway.

Apelin, the endogenous ligand of the G-Protein coupled receptor APJ, is widely expressed both in the brain and in the periphery, including the cardiovascular system, gastrointestinal tract, adipose tissue, lung, kidney, liver, uterus, ovary and skeletal muscle [86]. It is known to be an indispensable factor in embryonic vasculogenesis and, most importantly, tumor angiogenesis in malignant gliomas [84]. More specifically, Apelin and APJ were found to be expressed by endothelial cells in glioblastoma multiforme, particularly in areas of vessel sprouting and branching (endothelial tip-cells) as well as in radially oriented tumor cells surrounding band-like necrotic foci, indicating a putative hypoxia dependent function [84]. In endothelial cells Apelin intensifies proliferation, migration and capillary-like tube formation [90]. Excitingly, the study at hand has provided first evidence that both Apelin and APJ are expressed by a proportion of pericytes in general and of the tumor-associated pericytes characterized in this thesis, suggesting that both proteins may have so far unresolved functions in the biology of certain pericyte subpopulations. Given the fact that Apelin has shown to mediate angiogenesis in malignant gliomas [84], these findings might indicate that it carries out this function, amongst others, via pericytes.

### **5.3 Cells of the pericyte-lineage as future therapeutic targets?**

For Glioblastoma multiforme is a highly angiogenic tumor, research on anti-angiogenic therapies has surged in the last decades. Especially Bevacizumab, a humanized monoclonal antibody inhibiting VEGF [78, 92], has been proclaimed as a promising new drug in GBM therapy. However, this treatment has not shown an effect on overall survival of GBM patients [35, 93] and drug resistance by evasion of VEGF inhibition has been reported to occur in various preclinical settings [94, 95]. In addition to that, anti-angiogenic therapies of that kind have the potential to trigger a more aggressive and metastatic phenotype of GBM [207, 208]. Targeting endothelial cell interactions exclusively has thus so far not been a successful therapeutic strategy to inhibit tumor angiogenesis in GBM.

Recent findings suggest that pericytes, amongst other factors, protect the endothelium from VEGF-A inhibition [100] and Benjamin and colleagues have demonstrated that after VEGF-A ablation only tumor vasculature that lacked pericyte coverage was diminished [159]. Simultaneous targeting of both, endothelial cells and pericytes, has thus been proposed as a more promising therapeutic regime than conventional single-targeted strategies [160, 161]. Indeed, VEGF inhibitors applied in synergy with tyrosine kinase inhibitors directed against the pericyte marker PDGFR $\beta$  have shown more efficient blockage of tumor angiogenesis than VEGF inhibitors alone in a range of experimental models [160].

Furthermore, it was recently demonstrated that inhibiting VEGF-A/VEGFR-2 signaling in GBM accelerates the invasion of APJ expressing tumor cells and that Apelin/APJ signaling mediates GBM angiogenesis [177]. Blunting APJ by Apelin-F13A, a mutant form of the physiological Apelin-13 peptide, in turn, yields to reduced cell invasion as well as tumor angiogenesis in GBM models and has synergistic effects with VEGFR-2 blockade [177]. In models of primary lung and mammary tumors, Apelin inhibition was shown to reduce tumor blood vessel formation, vessel leakiness, hypoxia and immune cell infiltration [209]. In the light of the evidence for Apelin and APJ expression by pericytes in general and of the cells of non-pericyte identity characterized in this thesis, these effects of both Apelin and APJ inhibition may be mediated by cells of the pericyte lineage.

Notably, pericytes also display various functions under physiological conditions [200], making pericyte-targeted therapies likely to trigger ample side-effects which might restrict therapeutic applications. Targeting cells of a malignancy-specific pericyte lineage or sub-population would thus represent a more convenient strategy for antiangiogenic therapies than focusing on a generic pericyte phenotype. This study has provided evidence for a previously unknown lineage of pericytes, generating new pericytes during high-grade glioma angiogenesis and, as such, providing auspicious targets for future antiangiogenic therapies. For a potential clinical translation, however, further research on this lineage, its further development and origin is imperative.

## 6. Summary

The doctoral thesis at hand establishes a GL261 high-grade glioma model in double transgenic NesCreER<sup>T2</sup> x Ai9tdTomato mice as a novel tool to investigate the lineage of pericytes throughout glioma progression in vivo with RFP as reporter. Through a series of cell type identification analyses, using immunofluorescence labeling of brain sections and confocal microscopy, a highly proliferative cell type of non-pericyte identity was found, generating pericytes if exposed to high-grade gliomagenesis as angiogenic stimulus. The investigation of this newly identified pericyte-lineage revealed the following findings:

- (1) Throughout the two investigated time points of tumor progression, 14 and 21 DPO, the amount of the traced cells (i.e. the RFP positive cells) located in the tumor increases significantly and exclusively here, the traced cells develop from small cells of heterogenous morphology and scattered in location to cell conglomerates extending around and alongside endothelia.
- (2) As determined by a CldU/IdU thymidine analogue labeling paradigm, the traced cells proliferate extensively and the proportion of the traced cells which is not located in close apposition to vasculature traverses the cell cycle particularly fast, suggesting that especially the proportion of the traced cells which has not yet obtained a pericyte phenotype proliferates rapidly.
- (3) In the tumor parenchyma, the traced cells are incrementally located in a juxtaendothelial position and increasingly co-label with typical pericyte markers (Desmin, PDGFR $\beta$ , NG2) the further the neoplasm progresses, indicating that the traced cells develop into new tumor-associated pericytes if exposed to a highly angiogenic environment.
- (4) The traced cells do not co-label with the myeloid marker Iba1 and the stem cell marker Nestin as soon as they have obtained a pericyte phenotype (at 21 DPO), indicating that they do not [trans-] differentiate into Iba1 positive microglia/macrophages at that point of time. Furthermore, the traced cells express both Apelin and APJ when they have acquired a pericyte phenotype.

## 7. Zusammenfassung

In der vorliegenden medizinischen Doktorarbeit wird das GL261 High-Grade Gliom Model in NesCreER<sup>T2</sup> x Ai9tdTomato Mäusen als neues Instrument zur Untersuchung der Zelllinie von Tumor-assoziierten Perizyten in vivo mit RFP als Reporter etabliert. Anhand von Immunfluoreszenz-markierten Gehirnschnitten und Konfokalmikroskopie wurden hochgradig proliferative Zellen identifiziert, die keinen Perizyten-Phänotyp aufweisen, aus denen sich jedoch Perizyten unter dem pro-angiogenen Stimulus orthotop inokulierter Gliomzellen entwickelten. Im Rahmen der Untersuchung dieser neuen Zelllinie Tumor-assoziiertes Perizyten wurde Folgendes gezeigt:

- (1) Während der zwei untersuchten Zeitpunkte der Tumorprogression, 14 und 21 DPO, nahm die Anzahl der verfolgten Zellen (d.h. der RFP positiven Zellen) im Tumorgewebe signifikant zu. Zudem zeigte sich ausschließlich im Tumorgewebe, dass die sich verfolgten Zellen von kleinen, morphologisch heterogenen Zellen mit disseminierter Lokalisation zu Zellkonglomeraten entwickelten, welche sich um und entlang von Endothelzellen erstreckten.
- (2) Mithilfe eines CldU/IdU Labeling Protokolls wurde demonstriert, dass die verfolgten Zellen stark proliferieren und dass der Anteil verfolgter Zellen, die nicht juxtaendothelial positioniert sind, besonders stark proliferiert. Hieraus kann geschlossen werden, dass vornehmlich der Anteil verfolgter Zellen, welche noch keinen Perizyten Phänotyp angenommen haben, schnell proliferiert.
- (3) Im Tumorparenchym befinden sich die verfolgten Zellen zunehmend in juxtaendothelialer Position und exprimieren vermehrt etablierte Perizyten Marker (Desmin, PDGFR $\beta$ , NG2), je weiter die Tumorprogression fortschreitet, was auf eine zunehmende Differenzierung der verfolgten Zellen in Tumor-assoziierte Perizyten hinweist, sofern sie einem starken pro-angiogenem Stimulus ausgesetzt sind.
- (4) Die verfolgten Zellen weisen keine Expression des myeloiden Markers Iba1 und des Stammzellmarkers Nestin auf sobald sie einen Perizyten Phänotyp angenommen haben (21 DPO). Dies legt nahe, dass keine (Trans-) Differenzierung der verfolgten Zellen zu Iba1 positiven Mikroglia/Makrophagen erfolgt. Zudem exprimieren die verfolgten Zellen sowohl Apelin als auch APJ sobald sie einen Perizyten Phänotyp angenommen haben.

## 8. References

1. Alifieris, C. and D.T. Trafalis, *Glioblastoma multiforme: Pathogenesis and treatment*. Pharmacol Ther, 2015. **152**: p. 63-82.
2. Preusser, M., et al., *Current concepts and management of glioblastoma*. Ann Neurol, 2011. **70**(1): p. 9-21.
3. Louis, D.N., et al., *The 2007 WHO classification of tumours of the central nervous system*. Acta Neuropathol, 2007. **114**(2): p. 97-109.
4. Louis, D.N., et al., *The 2016 World Health Organization Classification of Tumors of the Central Nervous System: a summary*. Acta Neuropathol, 2016. **131**(6): p. 803-20.
5. Sahm, F., et al., *Addressing diffuse glioma as a systemic brain disease with single-cell analysis*. Arch Neurol, 2012. **69**(4): p. 523-6.
6. Goodenberger, M.L. and R.B. Jenkins, *Genetics of adult glioma*. Cancer Genet, 2012. **205**(12): p. 613-21.
7. Coons, S.W., et al., *Improving diagnostic accuracy and interobserver concordance in the classification and grading of primary gliomas*. Cancer, 1997. **79**(7): p. 1381-93.
8. Tabouret, E., et al., *Prognostic impact of the 2016 WHO classification of diffuse gliomas in the French POLA cohort*. Acta Neuropathol, 2016. **132**(4): p. 625-34.
9. Ostrom, Q.T., et al., *CBTRUS statistical report: primary brain and central nervous system tumors diagnosed in the United States in 2007-2011*. Neuro Oncol, 2014. **16 Suppl 4**: p. iv1-63.
10. Omuro, A. and L.M. DeAngelis, *Glioblastoma and other malignant gliomas: a clinical review*. Jama, 2013. **310**(17): p. 1842-50.
11. Harrison, R.A. and J.F. de Groot, *Treatment of Glioblastoma in the Elderly*. Drugs Aging, 2018.
12. Liu, Y., et al., *Long-term temozolomide might be an optimal choice for patient with multifocal glioblastoma, especially with deep-seated structure involvement: a case report and literature review*. World J Surg Oncol, 2015. **13**: p. 142.
13. Miller, C.R. and A. Perry, *Glioblastoma*. Arch Pathol Lab Med, 2007. **131**(3): p. 397-406.
14. Ohgaki, H. and P. Kleihues, *The definition of primary and secondary glioblastoma*. Clin Cancer Res, 2013. **19**(4): p. 764-72.
15. Ohgaki, H. and P. Kleihues, *Genetic pathways to primary and secondary glioblastoma*. Am J Pathol, 2007. **170**(5): p. 1445-53.
16. Maher, E.A., et al., *Malignant glioma: genetics and biology of a grave matter*. Genes Dev, 2001. **15**(11): p. 1311-33.
17. Yan, H., et al., *IDH1 and IDH2 mutations in gliomas*. N Engl J Med, 2009. **360**(8): p. 765-73.
18. Juratli, T.A., et al., *The prognostic value of IDH mutations and MGMT promoter status in secondary high-grade gliomas*. J Neurooncol, 2012. **110**(3): p. 325-33.
19. Alexander, B.M. and T.F. Cloughesy, *Adult Glioblastoma*. J Clin Oncol, 2017. **35**(21): p. 2402-2409.
20. Ryken, T.C., et al., *The role of imaging in the management of progressive glioblastoma : a systematic review and evidence-based clinical practice guideline*. J Neurooncol, 2014. **118**(3): p. 435-60.
21. Alexiou, G.A., et al., *Glioblastoma multiforme imaging: the role of nuclear medicine*. Curr Radiopharm, 2012. **5**(4): p. 308-13.

22. Boonzaier, N.R., et al., *Assessing and monitoring intratumor heterogeneity in glioblastoma: how far has multimodal imaging come?* CNS Oncol, 2015. **4**(6): p. 399-410.
23. Wick, W. and M. Platten, *Understanding and Treating Glioblastoma*. Neurol Clin, 2018. **36**(3): p. 485-499.
24. Aldape, K., et al., *Glioblastoma: pathology, molecular mechanisms and markers*. Acta Neuropathol, 2015. **129**(6): p. 829-48.
25. Weller, M., et al., *European Association for Neuro-Oncology (EANO) guideline on the diagnosis and treatment of adult astrocytic and oligodendroglial gliomas*. Lancet Oncol, 2017. **18**(6): p. e315-e329.
26. Platten, M., et al., *Concepts in glioma immunotherapy*. Cancer Immunol Immunother, 2016. **65**(10): p. 1269-75.
27. Stummer, W., et al., *5-Aminolevulinic acid-derived tumor fluorescence: the diagnostic accuracy of visible fluorescence qualities as corroborated by spectrometry and histology and postoperative imaging*. Neurosurgery, 2014. **74**(3): p. 310-9; discussion 319-20.
28. Stummer, W. and E. Suero Molina, *Fluorescence Imaging/Agents in Tumor Resection*. Neurosurg Clin N Am, 2017. **28**(4): p. 569-583.
29. Roa, W., et al., *Abbreviated course of radiation therapy in older patients with glioblastoma multiforme: a prospective randomized clinical trial*. J Clin Oncol, 2004. **22**(9): p. 1583-8.
30. Malmstrom, A., et al., *Temozolomide versus standard 6-week radiotherapy versus hypofractionated radiotherapy in patients older than 60 years with glioblastoma: the Nordic randomised, phase 3 trial*. Lancet Oncol, 2012. **13**(9): p. 916-26.
31. Perry, J.R., N. Laperriere, and W.P. Mason, *Radiation plus Temozolomide in Patients with Glioblastoma*. N Engl J Med, 2017. **376**(22): p. 2197.
32. Stupp, R., et al., *Radiotherapy plus concomitant and adjuvant temozolomide for glioblastoma*. N Engl J Med, 2005. **352**(10): p. 987-96.
33. Chinot, O.L., et al., *Bevacizumab plus radiotherapy-temozolomide for newly diagnosed glioblastoma*. N Engl J Med, 2014. **370**(8): p. 709-22.
34. Gilbert, M.R., et al., *A randomized trial of bevacizumab for newly diagnosed glioblastoma*. N Engl J Med, 2014. **370**(8): p. 699-708.
35. Wick, W., et al., *Lomustine and Bevacizumab in Progressive Glioblastoma*. N Engl J Med, 2017. **377**(20): p. 1954-1963.
36. Wick, W., et al., *EORTC 26101 phase III trial exploring the combination of bevacizumab and lomustine in patients with first progression of a glioblastoma*. Journal of Clinical Oncology, 2016. **34**(15\_suppl): p. 2001-2001.
37. Weller, M., et al., *How we treat glioblastoma*. ESMO Open, 2019. **4**(Suppl 2): p. e000520.
38. Sasmita, A.O., Y.P. Wong, and A.P.K. Ling, *Biomarkers and therapeutic advances in glioblastoma multiforme*. Asia Pac J Clin Oncol, 2018. **14**(1): p. 40-51.
39. Cloughesy, T.F., et al., *Phase 1 trial of vocimagene amiretrorepvec and 5-fluorocytosine for recurrent high-grade glioma*. Sci Transl Med, 2016. **8**(341): p. 341ra75.
40. Strebe, J.K., J.A. Lubin, and J.S. Kuo, *"Tag Team" Glioblastoma Therapy: Results From a Phase 1 Trial of Toca 511 and 5-Fluorocytosine for Recurrent High-Grade Glioma*. Neurosurgery, 2016. **79**(6): p. N18-n20.
41. Sampson, J.H., et al., *Immunologic escape after prolonged progression-free survival with epidermal growth factor receptor variant III peptide vaccination in patients with newly diagnosed glioblastoma*. J Clin Oncol, 2010. **28**(31): p. 4722-9.

42. Bloch, O., et al., *Heat-shock protein peptide complex-96 vaccination for recurrent glioblastoma: a phase II, single-arm trial*. *Neuro Oncol*, 2014. **16**(2): p. 274-9.
43. Brown, C.E., et al., *Regression of Glioblastoma after Chimeric Antigen Receptor T-Cell Therapy*. *N Engl J Med*, 2016. **375**(26): p. 2561-9.
44. Omuro, A., et al., *Nivolumab with or without ipilimumab in patients with recurrent glioblastoma: results from exploratory phase I cohorts of CheckMate 143*. *Neuro Oncol*, 2018. **20**(5): p. 674-686.
45. Carter, T., et al., *Ipilimumab and Bevacizumab in Glioblastoma*. *Clin Oncol (R Coll Radiol)*, 2016. **28**(10): p. 622-6.
46. Kessler, T., et al., *Molecular differences in IDH wildtype glioblastoma according to MGMT promoter methylation*. *Neuro Oncol*, 2018. **20**(3): p. 367-379.
47. Wick, W., et al., *MGMT testing--the challenges for biomarker-based glioma treatment*. *Nat Rev Neurol*, 2014. **10**(7): p. 372-85.
48. Crocetti, E., et al., *Epidemiology of glial and non-glial brain tumours in Europe*. *Eur J Cancer*, 2012. **48**(10): p. 1532-42.
49. Ostrom, Q.T., et al., *CBTRUS Statistical Report: Primary brain and other central nervous system tumors diagnosed in the United States in 2010-2014*. *Neuro Oncol*, 2017. **19**(suppl\_5): p. v1-v88.
50. Li, L.T., et al., *Ki67 is a promising molecular target in the diagnosis of cancer (review)*. *Mol Med Rep*, 2015. **11**(3): p. 1566-72.
51. Brown, D.C. and K.C. Gatter, *Ki67 protein: the immaculate deception?* *Histopathology*, 2002. **40**(1): p. 2-11.
52. Nowakowski, R.S., S.B. Lewin, and M.W. Miller, *Bromodeoxyuridine immunohistochemical determination of the lengths of the cell cycle and the DNA-synthetic phase for an anatomically defined population*. *J Neurocytol*, 1989. **18**(3): p. 311-8.
53. Tuttle, A.H., et al., *Immunofluorescent detection of two thymidine analogues (CldU and IdU) in primary tissue*. *J Vis Exp*, 2010(46).
54. Chehrehasa, F., et al., *EdU, a new thymidine analogue for labelling proliferating cells in the nervous system*. *J Neurosci Methods*, 2009. **177**(1): p. 122-30.
55. Wacker, M.R., et al., *The prognostic implications of histologic classification and bromodeoxyuridine labeling index of mixed gliomas*. *J Neurooncol*, 1994. **19**(2): p. 113-22.
56. Sharma, S., et al., *A correlative study of gliomas using in vivo bromodeoxyuridine labeling index and computer-aided malignancy grading*. *Pathol Oncol Res*, 1999. **5**(2): p. 134-41.
57. Payton, M., et al., *Antagonism of Ang-Tie2 and Dll4-Notch signaling has opposing effects on tumor endothelial cell proliferation, evidenced by a new flow cytometry method*. *Lab Invest*, 2014. **94**(11): p. 1296-308.
58. Pittman, R.N., *Oxygen transport in the microcirculation and its regulation*. *Microcirculation*, 2013. **20**(2): p. 117-37.
59. Folkman, J. and M. Klagsbrun, *Angiogenic factors*. *Science*, 1987. **235**(4787): p. 442-7.
60. Risau, W., *Mechanisms of angiogenesis*. *Nature*, 1997. **386**(6626): p. 671-4.
61. Hardee, M.E. and D. Zagzag, *Mechanisms of glioma-associated neovascularization*. *Am J Pathol*, 2012. **181**(4): p. 1126-41.
62. Folkman, J., et al., *Induction of angiogenesis during the transition from hyperplasia to neoplasia*. *Nature*, 1989. **339**(6219): p. 58-61.
63. Folkman, J., et al., *Isolation of a tumor factor responsible for angiogenesis*. *J Exp Med*, 1971. **133**(2): p. 275-88.

64. Naumov, G.N., et al., *Tumor-vascular interactions and tumor dormancy*. *Apmis*, 2008. **116**(7-8): p. 569-85.
65. Hanahan, D. and R.A. Weinberg, *Hallmarks of cancer: the next generation*. *Cell*, 2011. **144**(5): p. 646-74.
66. Hanahan, D. and R.A. Weinberg, *The hallmarks of cancer*. *Cell*, 2000. **100**(1): p. 57-70.
67. Carmeliet, P. and R.K. Jain, *Angiogenesis in cancer and other diseases*. *Nature*, 2000. **407**(6801): p. 249-57.
68. Fukumura, D. and R.K. Jain, *Tumor microvasculature and microenvironment: targets for anti-angiogenesis and normalization*. *Microvasc Res*, 2007. **74**(2-3): p. 72-84.
69. Claesson-Welsh, L., *Blood vessels as targets in tumor therapy*. *Ups J Med Sci*, 2012. **117**(2): p. 178-86.
70. Baluk, P., H. Hashizume, and D.M. McDonald, *Cellular abnormalities of blood vessels as targets in cancer*. *Curr Opin Genet Dev*, 2005. **15**(1): p. 102-11.
71. Shweiki, D., et al., *Vascular endothelial growth factor induced by hypoxia may mediate hypoxia-initiated angiogenesis*. *Nature*, 1992. **359**(6398): p. 843-5.
72. Goel, S., et al., *Normalization of the vasculature for treatment of cancer and other diseases*. *Physiol Rev*, 2011. **91**(3): p. 1071-121.
73. Gargett, C.E. and P.A. Rogers, *Human endometrial angiogenesis*. *Reproduction*, 2001. **121**(2): p. 181-6.
74. Dvorak, H.F., *Tumors: wounds that do not heal. Similarities between tumor stroma generation and wound healing*. *N Engl J Med*, 1986. **315**(26): p. 1650-9.
75. Vasudev, N.S. and A.R. Reynolds, *Anti-angiogenic therapy for cancer: current progress, unresolved questions and future directions*. *Angiogenesis*, 2014. **17**(3): p. 471-94.
76. Baeriswyl, V. and G. Christofori, *The angiogenic switch in carcinogenesis*. *Semin Cancer Biol*, 2009. **19**(5): p. 329-37.
77. Kerbel, R.S., *Antiangiogenic therapy: a universal chemosensitization strategy for cancer?* *Science*, 2006. **312**(5777): p. 1171-5.
78. Weathers, S.P. and J. de Groot, *VEGF Manipulation in Glioblastoma*. *Oncology (Williston Park)*, 2015. **29**(10): p. 720-7.
79. Liu, A.Y. and G. Ouyang, *Tumor angiogenesis: a new source of pericytes*. *Curr Biol*, 2013. **23**(13): p. R565-8.
80. Yang, Y., et al., *Apelin/APJ system and cancer*. *Clin Chim Acta*, 2016. **457**: p. 112-6.
81. Wu, L., L. Chen, and L. Li, *Apelin/APJ system: A novel promising therapy target for pathological angiogenesis*. *Clin Chim Acta*, 2017. **466**: p. 78-84.
82. Tatemoto, K., et al., *Isolation and characterization of a novel endogenous peptide ligand for the human APJ receptor*. *Biochem Biophys Res Commun*, 1998. **251**(2): p. 471-6.
83. Hosoya, M., et al., *Molecular and functional characteristics of APJ. Tissue distribution of mRNA and interaction with the endogenous ligand apelin*. *J Biol Chem*, 2000. **275**(28): p. 21061-7.
84. Kalin, R.E., et al., *Paracrine and autocrine mechanisms of apelin signaling govern embryonic and tumor angiogenesis*. *Dev Biol*, 2007. **305**(2): p. 599-614.
85. Devic, E., et al., *Amino acid sequence and embryonic expression of msr/apj, the mouse homolog of Xenopus X-msr and human APJ*. *Mech Dev*, 1999. **84**(1-2): p. 199-203.
86. O'Carroll, A.M., et al., *The apelin receptor APJ: journey from an orphan to a multifaceted regulator of homeostasis*. *J Endocrinol*, 2013. **219**(1): p. R13-35.

87. Folino, A., et al., *Effects of apelin on the cardiovascular system*. Heart Fail Rev, 2015. **20**(4): p. 505-18.
88. Chapman, N.A., D.J. Dupre, and J.K. Rainey, *The apelin receptor: physiology, pathology, cell signalling, and ligand modulation of a peptide-activated class A GPCR*. Biochem Cell Biol, 2014. **92**(6): p. 431-40.
89. Kang, Y., et al., *Apelin-APJ signaling is a critical regulator of endothelial MEF2 activation in cardiovascular development*. Circ Res, 2013. **113**(1): p. 22-31.
90. Kasai, A., et al., *Apelin is a novel angiogenic factor in retinal endothelial cells*. Biochem Biophys Res Commun, 2004. **325**(2): p. 395-400.
91. Folkman, J., *Angiogenesis research: from laboratory to clinic*. Forum (Genova), 1999. **9**(3 Suppl 3): p. 59-62.
92. Wang, N., R.K. Jain, and T.T. Batchelor, *New Directions in Anti-Angiogenic Therapy for Glioblastoma*. Neurotherapeutics, 2017. **14**(2): p. 321-332.
93. Taal, W., et al., *Single-agent bevacizumab or lomustine versus a combination of bevacizumab plus lomustine in patients with recurrent glioblastoma (BELOB trial): a randomised controlled phase 2 trial*. Lancet Oncol, 2014. **15**(9): p. 943-53.
94. Casanovas, O., et al., *Drug resistance by evasion of antiangiogenic targeting of VEGF signaling in late-stage pancreatic islet tumors*. Cancer Cell, 2005. **8**(4): p. 299-309.
95. Mizukami, Y., et al., *Induction of interleukin-8 preserves the angiogenic response in HIF-1alpha-deficient colon cancer cells*. Nat Med, 2005. **11**(9): p. 992-7.
96. van Dijk, C.G., et al., *The complex mural cell: pericyte function in health and disease*. Int J Cardiol, 2015. **190**: p. 75-89.
97. Bentov, I. and M.J. Reed, *The effect of aging on the cutaneous microvasculature*. Microvasc Res, 2015. **100**: p. 25-31.
98. Rouget, C., *Mémoire sur le développement, la structure et les propriétés physiologique des capillaires sanguins et lymphatiques*. 1873.
99. Zimmermann, K.W., *Der feinere bau der blutcapillaren*. Zeitschrift für Anatomie und Entwicklungsgeschichte, 1923. **68**(1): p. 29-109.
100. Armulik, A., G. Genove, and C. Betsholtz, *Pericytes: developmental, physiological, and pathological perspectives, problems, and promises*. Dev Cell, 2011. **21**(2): p. 193-215.
101. Sims, D.E., *The pericyte--a review*. Tissue Cell, 1986. **18**(2): p. 153-74.
102. Diaz-Flores, L., et al., *Pericytes. Morphofunction, interactions and pathology in a quiescent and activated mesenchymal cell niche*. Histol Histopathol, 2009. **24**(7): p. 909-69.
103. Hida, K., et al., *Tumor angiogenesis--characteristics of tumor endothelial cells*. Int J Clin Oncol, 2016. **21**(2): p. 206-212.
104. Shepro, D. and N.M. Morel, *Pericyte physiology*. Faseb j, 1993. **7**(11): p. 1031-8.
105. Mathiisen, T.M., et al., *The perivascular astroglial sheath provides a complete covering of the brain microvessels: an electron microscopic 3D reconstruction*. Glia, 2010. **58**(9): p. 1094-103.
106. Petrova, T.V., et al., *Defective valves and abnormal mural cell recruitment underlie lymphatic vascular failure in lymphedema distichiasis*. Nat Med, 2004. **10**(9): p. 974-81.
107. Daneman, R. and A. Prat, *The blood-brain barrier*. Cold Spring Harb Perspect Biol, 2015. **7**(1): p. a020412.
108. Zlokovic, B.V., *The blood-brain barrier in health and chronic neurodegenerative disorders*. Neuron, 2008. **57**(2): p. 178-201.

109. Daneman, R., *The blood–brain barrier in health and disease*. Annals of neurology, 2012. **72**(5): p. 648-672.
110. Muoio, V., P.B. Persson, and M.M. Sendeski, *The neurovascular unit - concept review*. Acta Physiol (Oxf), 2014. **210**(4): p. 790-8.
111. Daneman, R., et al., *Pericytes are required for blood-brain barrier integrity during embryogenesis*. Nature, 2010. **468**(7323): p. 562-6.
112. Bell, R.D., et al., *Pericytes control key neurovascular functions and neuronal phenotype in the adult brain and during brain aging*. Neuron, 2010. **68**(3): p. 409-27.
113. Sa-Pereira, I., D. Brites, and M.A. Brito, *Neurovascular unit: a focus on pericytes*. Mol Neurobiol, 2012. **45**(2): p. 327-47.
114. Stratman, A.N. and G.E. Davis, *Endothelial cell-pericyte interactions stimulate basement membrane matrix assembly: influence on vascular tube remodeling, maturation, and stabilization*. Microsc Microanal, 2012. **18**(1): p. 68-80.
115. Allt, G. and J.G. Lawrenson, *Pericytes: cell biology and pathology*. Cells Tissues Organs, 2001. **169**(1): p. 1-11.
116. Nehls, V. and D. Drenckhahn, *The versatility of microvascular pericytes: from mesenchyme to smooth muscle? Histochemistry*, 1993. **99**(1): p. 1-12.
117. Nehls, V., K. Denzer, and D. Drenckhahn, *Pericyte involvement in capillary sprouting during angiogenesis in situ*. Cell Tissue Res, 1992. **270**(3): p. 469-74.
118. Puro, D.G., *Physiology and pathobiology of the pericyte-containing retinal microvasculature: new developments*. Microcirculation, 2007. **14**(1): p. 1-10.
119. Rucker, H.K., H.J. Wynder, and W.E. Thomas, *Cellular mechanisms of CNS pericytes*. Brain Res Bull, 2000. **51**(5): p. 363-9.
120. Attwell, D., et al., *Glial and neuronal control of brain blood flow*. Nature, 2010. **468**(7321): p. 232-43.
121. Carmeliet, P. and R.K. Jain, *Molecular mechanisms and clinical applications of angiogenesis*. Nature, 2011. **473**(7347): p. 298-307.
122. Hall, A.P., *Review of the pericyte during angiogenesis and its role in cancer and diabetic retinopathy*. Toxicol Pathol, 2006. **34**(6): p. 763-75.
123. Gerhardt, H. and C. Betsholtz, *Endothelial-pericyte interactions in angiogenesis*. Cell Tissue Res, 2003. **314**(1): p. 15-23.
124. Song, S., et al., *PDGFRbeta+ perivascular progenitor cells in tumours regulate pericyte differentiation and vascular survival*. Nat Cell Biol, 2005. **7**(9): p. 870-9.
125. Hellstrom, M., et al., *Lack of pericytes leads to endothelial hyperplasia and abnormal vascular morphogenesis*. J Cell Biol, 2001. **153**(3): p. 543-53.
126. Huang, F.J., et al., *Pericyte deficiencies lead to aberrant tumor vascularization in the brain of the NG2 null mouse*. Dev Biol, 2010. **344**(2): p. 1035-46.
127. Smith, S.W., S. Chand, and C.O. Savage, *Biology of the renal pericyte*. Nephrol Dial Transplant, 2012. **27**(6): p. 2149-55.
128. Ozerdem, U., et al., *NG2 proteoglycan is expressed exclusively by mural cells during vascular morphogenesis*. Dev Dyn, 2001. **222**(2): p. 218-27.
129. Winkler, E.A., R.D. Bell, and B.V. Zlokovic, *Pericyte-specific expression of PDGF beta receptor in mouse models with normal and deficient PDGF beta receptor signaling*. Mol Neurodegener, 2010. **5**: p. 32.
130. Crisan, M., et al., *A perivascular origin for mesenchymal stem cells in multiple human organs*. Cell Stem Cell, 2008. **3**(3): p. 301-13.
131. Crisan, M., et al., *Perivascular cells for regenerative medicine*. J Cell Mol Med, 2012. **16**(12): p. 2851-60.

132. Alliot, F., et al., *Pericytes and periendothelial cells of brain parenchyma vessels co-express aminopeptidase N, aminopeptidase A, and nestin*. J Neurosci Res, 1999. **58**(3): p. 367-78.
133. Xueyong, L., et al., *Differentiation of the pericyte in wound healing: The precursor, the process, and the role of the vascular endothelial cell*. Wound Repair Regen, 2008. **16**(3): p. 346-55.
134. Bandopadhyay, R., et al., *Contractile proteins in pericytes at the blood-brain and blood-retinal barriers*. J Neurocytol, 2001. **30**(1): p. 35-44.
135. Birbrair, A., et al., *Type-2 pericytes participate in normal and tumoral angiogenesis*. Am J Physiol Cell Physiol, 2014. **307**(1): p. C25-38.
136. Corselli, M., et al., *Perivascular ancestors of adult multipotent stem cells*. Arterioscler Thromb Vasc Biol, 2010. **30**(6): p. 1104-9.
137. Crisan, M., et al., *Multilineage stem cells in the adult: a perivascular legacy?* Organogenesis, 2011. **7**(2): p. 101-4.
138. Birbrair, A., et al., *Type-1 pericytes participate in fibrous tissue deposition in aged skeletal muscle*. Am J Physiol Cell Physiol, 2013. **305**(11): p. C1098-113.
139. Birbrair, A., et al., *Role of pericytes in skeletal muscle regeneration and fat accumulation*. Stem Cells Dev, 2013. **22**(16): p. 2298-314.
140. Birbrair, A., et al., *Skeletal muscle pericyte subtypes differ in their differentiation potential*. Stem Cell Res, 2013. **10**(1): p. 67-84.
141. Korn, J., B. Christ, and H. Kurz, *Neuroectodermal origin of brain pericytes and vascular smooth muscle cells*. J Comp Neurol, 2002. **442**(1): p. 78-88.
142. Etchevers, H.C., et al., *The cephalic neural crest provides pericytes and smooth muscle cells to all blood vessels of the face and forebrain*. Development, 2001. **128**(7): p. 1059-68.
143. Bergwerff, M., et al., *Neural crest cell contribution to the developing circulatory system: implications for vascular morphology?* Circ Res, 1998. **82**(2): p. 221-31.
144. Foster, K., et al., *Contribution of neural crest-derived cells in the embryonic and adult thymus*. J Immunol, 2008. **180**(5): p. 3183-9.
145. Muller, S.M., et al., *Neural crest origin of perivascular mesenchyme in the adult thymus*. J Immunol, 2008. **180**(8): p. 5344-51.
146. Cai, C.L., et al., *A myocardial lineage derives from Tbx18 epicardial cells*. Nature, 2008. **454**(7200): p. 104-8.
147. Lindahl, P., et al., *Pericyte loss and microaneurysm formation in PDGF-B-deficient mice*. Science, 1997. **277**(5323): p. 242-5.
148. Hall, C.N., et al., *Capillary pericytes regulate cerebral blood flow in health and disease*. Nature, 2014. **508**(7494): p. 55-60.
149. Sagare, A.P., et al., *Pericyte loss influences Alzheimer-like neurodegeneration in mice*. Nat Commun, 2013. **4**: p. 2932.
150. Abramsson, A., et al., *Defective N-sulfation of heparan sulfate proteoglycans limits PDGF-BB binding and pericyte recruitment in vascular development*. Genes Dev, 2007. **21**(3): p. 316-31.
151. Nolan-Stevaux, O., et al., *Differential contribution to neuroendocrine tumorigenesis of parallel egfr signaling in cancer cells and pericytes*. Genes Cancer, 2010. **1**(2): p. 125-41.
152. Cascone, T., et al., *Upregulated stromal EGFR and vascular remodeling in mouse xenograft models of angiogenesis inhibitor-resistant human lung adenocarcinoma*. J Clin Invest, 2011. **121**(4): p. 1313-28.
153. Nisancioglu, M.H., et al., *Generation and characterization of rgs5 mutant mice*. Mol Cell Biol, 2008. **28**(7): p. 2324-31.

154. Raza, A., M.J. Franklin, and A.Z. Dudek, *Pericytes and vessel maturation during tumor angiogenesis and metastasis*. Am J Hematol, 2010. **85**(8): p. 593-8.
155. Abramsson, A., et al., *Analysis of mural cell recruitment to tumor vessels*. Circulation, 2002. **105**(1): p. 112-7.
156. Du, R., et al., *HIF1alpha induces the recruitment of bone marrow-derived vascular modulatory cells to regulate tumor angiogenesis and invasion*. Cancer Cell, 2008. **13**(3): p. 206-20.
157. Rajantie, I., et al., *Adult bone marrow-derived cells recruited during angiogenesis comprise precursors for periendothelial vascular mural cells*. Blood, 2004. **104**(7): p. 2084-6.
158. Pietras, K. and A. Ostman, *Hallmarks of cancer: interactions with the tumor stroma*. Exp Cell Res, 2010. **316**(8): p. 1324-31.
159. Benjamin, L.E., et al., *Selective ablation of immature blood vessels in established human tumors follows vascular endothelial growth factor withdrawal*. J Clin Invest, 1999. **103**(2): p. 159-65.
160. Bergers, G., et al., *Benefits of targeting both pericytes and endothelial cells in the tumor vasculature with kinase inhibitors*. J Clin Invest, 2003. **111**(9): p. 1287-95.
161. Erber, R., et al., *Combined inhibition of VEGF and PDGF signaling enforces tumor vessel regression by interfering with pericyte-mediated endothelial cell survival mechanisms*. Faseb j, 2004. **18**(2): p. 338-40.
162. Imayoshi, I., et al., *Temporal regulation of Cre recombinase activity in neural stem cells*. Genesis, 2006. **44**(5): p. 233-8.
163. Van Duyne, G.D., *Cre Recombinase*. Microbiol Spectr, 2015. **3**(1): p. Mdna3-0014-2014.
164. Kratochwil, C.F. and F.M. Rijli, *The Cre/Lox system to assess the development of the mouse brain*. Methods Mol Biol, 2014. **1082**: p. 295-313.
165. Jahn, H.M., A. Scheller, and F. Kirchhoff, *Genetic control of astrocyte function in neural circuits*. Front Cell Neurosci, 2015. **9**: p. 310.
166. Giachino, C. and V. Taylor, *Lineage analysis of quiescent regenerative stem cells in the adult brain by genetic labelling reveals spatially restricted neurogenic niches in the olfactory bulb*. Eur J Neurosci, 2009. **30**(1): p. 9-24.
167. Stock, K., et al., *Neural precursor cells induce cell death of high-grade astrocytomas through stimulation of TRPV1*. Nat Med, 2012. **18**(8): p. 1232-8.
168. Erasso, D.M., et al., *Effects of isoflurane or propofol on postnatal hippocampal neurogenesis in young and aged rats*. Brain Res, 2013. **1530**: p. 1-12.
169. Brandt, M.D., E. Ellwardt, and A. Storch, *Short- and long-term treatment with modafinil differentially affects adult hippocampal neurogenesis*. Neuroscience, 2014. **278**: p. 267-75.
170. Teta, M., et al., *Growth and regeneration of adult beta cells does not involve specialized progenitors*. Dev Cell, 2007. **12**(5): p. 817-26.
171. Llorens-Martin, M. and J.L. Trejo, *Multiple birthdating analyses in adult neurogenesis: a line-up of the usual suspects*. Front Neurosci, 2011. **5**: p. 76.
172. Ramos-Vara, J.A., *Technical aspects of immunohistochemistry*. Vet Pathol, 2005. **42**(4): p. 405-26.
173. Hosseini, H., et al., *Inhibiting angiogenesis with human single-chain variable fragment antibody targeting VEGF*. Microvasc Res, 2015. **97**: p. 13-8.
174. Lun, Y.Z., et al., *Cloning, expression and identification by immunohistochemistry of humanized single-chain variable fragment antibody against hepatitis C virus core protein*. Pol J Microbiol, 2011. **60**(1): p. 13-7.

175. Rymo, S.F., et al., *A two-way communication between microglial cells and angiogenic sprouts regulates angiogenesis in aortic ring cultures*. PLoS One, 2011. **6**(1): p. e15846.
176. Yang, Y., et al., *Attenuation of acute stroke injury in rat brain by minocycline promotes blood-brain barrier remodeling and alternative microglia/macrophage activation during recovery*. J Neuroinflammation, 2015. **12**: p. 26.
177. Mastrella, G., et al., *Targeting APLN/APLNR Improves Antiangiogenic Efficiency and Blunts Proinvasive Side Effects of VEGFA/VEGFR2 Blockade in Glioblastoma*. Cancer Res, 2019. **79**(9): p. 2298-2313.
178. Herrmann, M., et al., *Pericyte plasticity - comparative investigation of the angiogenic and multilineage potential of pericytes from different human tissues*. Eur Cell Mater, 2016. **31**: p. 236-49.
179. Yamamoto, S., et al., *A subset of cerebrovascular pericytes originates from mature macrophages in the very early phase of vascular development in CNS*. Sci Rep, 2017. **7**(1): p. 3855.
180. Sakuma, R., et al., *Brain pericytes serve as microglia-generating multipotent vascular stem cells following ischemic stroke*. J Neuroinflammation, 2016. **13**(1): p. 57.
181. Hughes, E.G. and D.E. Bergles, *Hidden progenitors replace microglia in the adult brain*. Neuron, 2014. **82**(2): p. 253-5.
182. Martin, E., et al., *Analysis of Microglia and Monocyte-derived Macrophages from the Central Nervous System by Flow Cytometry*. J Vis Exp, 2017(124).
183. Kluge, M.G., et al., *Impaired microglia process dynamics post-stroke are specific to sites of secondary neurodegeneration*. Glia, 2017. **65**(12): p. 1885-1899.
184. Zou, W., et al., *CHAPTER 7 - Isolation, culture and propagation of dendritic cells*, in *Dendritic Cells (Second Edition)*, M.T. Lotze and A.W. Thomson, Editors. 2001, Academic Press: London. p. 77-96.
185. Cooper, G.M., R.E. Hausman, and R.E. Hausman, *The cell: a molecular approach*. Vol. 10. 2000: ASM press Washington, DC.
186. Szatmari, T., et al., *Detailed characterization of the mouse glioma 261 tumor model for experimental glioblastoma therapy*. Cancer Sci, 2006. **97**(6): p. 546-53.
187. Wu, A., et al., *Persistence of CD133+ cells in human and mouse glioma cell lines: detailed characterization of GL261 glioma cells with cancer stem cell-like properties*. Stem Cells Dev, 2008. **17**(1): p. 173-84.
188. Franco, M., et al., *Pericytes promote endothelial cell survival through induction of autocrine VEGF-A signaling and Bcl-w expression*. Blood, 2011. **118**(10): p. 2906-17.
189. Bose, A., et al., *Tumor-derived vascular pericytes anergize Th cells*. J Immunol, 2013. **191**(2): p. 971-81.
190. Ochs, K., et al., *Immature mesenchymal stem cell-like pericytes as mediators of immunosuppression in human malignant glioma*. J Neuroimmunol, 2013. **265**(1-2): p. 106-16.
191. Bexell, D., et al., *Bone marrow multipotent mesenchymal stroma cells act as pericyte-like migratory vehicles in experimental gliomas*. Mol Ther, 2009. **17**(1): p. 183-90.
192. Yamazaki, T., et al., *Tissue Myeloid Progenitors Differentiate into Pericytes through TGF-beta Signaling in Developing Skin Vasculature*. Cell Rep, 2017. **18**(12): p. 2991-3004.
193. Mazare, N., et al., *Connexin 30 is expressed in a subtype of mouse brain pericytes*. Brain Struct Funct, 2018. **223**(2): p. 1017-1024.

194. Hartmann, D.A., et al., *Pericyte structure and distribution in the cerebral cortex revealed by high-resolution imaging of transgenic mice*. Neurophotonics, 2015. **2**(4): p. 041402.
195. Armulik, A., et al., *Pericytes regulate the blood-brain barrier*. Nature, 2010. **468**(7323): p. 557-61.
196. Bondjers, C., et al., *Microarray analysis of blood microvessels from PDGF-B and PDGF-Rbeta mutant mice identifies novel markers for brain pericytes*. Faseb j, 2006. **20**(10): p. 1703-5.
197. Zeisel, A., et al., *Brain structure. Cell types in the mouse cortex and hippocampus revealed by single-cell RNA-seq*. Science, 2015. **347**(6226): p. 1138-42.
198. Zhang, Y., et al., *An RNA-sequencing transcriptome and splicing database of glia, neurons, and vascular cells of the cerebral cortex*. J Neurosci, 2014. **34**(36): p. 11929-47.
199. He, L., et al., *Analysis of the brain mural cell transcriptome*. Sci Rep, 2016. **6**: p. 35108.
200. Ferland-McCollough, D., et al., *Pericytes, an overlooked player in vascular pathobiology*. Pharmacol Ther, 2017. **171**: p. 30-42.
201. Pedrosa, A.R., et al., *Endothelial Jagged1 promotes solid tumor growth through both pro-angiogenic and angiocrine functions*. Oncotarget, 2015. **6**(27): p. 24404-23.
202. Armulik, A., A. Abramsson, and C. Betsholtz, *Endothelial/pericyte interactions*. Circ Res, 2005. **97**(6): p. 512-23.
203. Liu, Y., et al., *Edg-1, the G protein-coupled receptor for sphingosine-1-phosphate, is essential for vascular maturation*. J Clin Invest, 2000. **106**(8): p. 951-61.
204. Dohgu, S., et al., *Brain pericytes contribute to the induction and up-regulation of blood-brain barrier functions through transforming growth factor-beta production*. Brain Res, 2005. **1038**(2): p. 208-15.
205. Bjarnegard, M., et al., *Endothelium-specific ablation of PDGFB leads to pericyte loss and glomerular, cardiac and placental abnormalities*. Development, 2004. **131**(8): p. 1847-57.
206. Enge, M., et al., *Endothelium-specific platelet-derived growth factor-B ablation mimics diabetic retinopathy*. Embo j, 2002. **21**(16): p. 4307-16.
207. Paez-Ribes, M., et al., *Antiangiogenic therapy elicits malignant progression of tumors to increased local invasion and distant metastasis*. Cancer Cell, 2009. **15**(3): p. 220-31.
208. Potente, M., H. Gerhardt, and P. Carmeliet, *Basic and therapeutic aspects of angiogenesis*. Cell, 2011. **146**(6): p. 873-87.
209. Uribesalgo, I., et al., *Apelin inhibition prevents resistance and metastasis associated with anti-angiogenic therapy*. EMBO Mol Med, 2019: p. e9266.

## 9. Eidesstattliche Versicherung



### Eidesstattliche Versicherung

**Eisenhut, Katharina**

Name, Vorname

Ich erkläre hiermit an Eides statt,

dass ich die vorliegende Dissertation mit dem Titel

**"Lineage-tracing reveals the genesis of pericytes from Nestin expressing cells during glioma angiogenesis"**

selbständig verfasst, mich außer der angegebenen keiner weiteren Hilfsmittel bedient und alle Erkenntnisse, die aus dem Schrifttum ganz oder annähernd übernommen sind, als solche kenntlich gemacht und nach ihrer Herkunft unter Bezeichnung der Fundstelle einzeln nachgewiesen habe.

Ich erkläre des Weiteren, dass die hier vorgelegte Dissertation nicht in gleicher oder in ähnlicher Form bei einer anderen Stelle zur Erlangung eines akademischen Grades eingereicht wurde.

München, den 03.04.2021

Ort, Datum

Katharina Eisenhut

Unterschrift Doktorandin bzw. Doktorand

## 10. Acknowledgements

First of all, I want to express my sincere gratitude to Prof. Rainer Glaß for the possibility to carry out this project in his research group as well as his continuous guidance and support during my doctoral studies.

Likewise, I am grateful to Dr. Roland Kälin for his methodological advice, his encouragement and the many helpful discussions regarding my research project.

Further, I would like to give thanks to all current and former members of the neurosurgical research group, who were involved in my project, particularly Yuping Li and Yingxi Wu for their assistance with the in vivo experiments and the prolific collaboration. For her consistent technical aid, I moreover thank Stefanie Lange.

Also, I am thankful for being admitted to and supported by the *FöFoLe* Program (“Programm zur Förderung von Forschung und Lehre”) of the Medical Faculty of Ludwig Maximilians University Munich.

Finally, I herewith cordially thank my parents for their ceaseless assurance, not only but especially regarding the doctoral thesis at hand.

## 12. Publication

During my doctoral studies, I contributed to the following publication:

Mastrella, G., Hou, M., Li, M., Stöcklein, V.M., Zdouc, N., Volmar, M.N.M., Miletic, H., Reinhard, S., Herold-Mende, C.C., Kleber, S., **Eisenhut, K.**, Gargiulo, G., Synowitz, M., Vescovi, A., Harter, P., Penninger, J.M., Wagner, E., Mittelbronn, M., Bjerkwig, R., Hambardzumyan, D., Schüller, U., Tonn, J.C., Radke, J., Glass, R., Kälin, R.E., *Targeting APLN/APLNR Improves Antiangiogenic Efficiency and Blunts Proinvasive Side Effects of VEGFA/VEGFR2 Blockade in Glioblastoma*. *Cancer Res*, 2019. **79**(9): p. 2298-2313.